

# **Accuracy of patient-specific dosimetry using hybrid planar-SPECT/CT imaging: A Monte Carlo study**

by

Michaela Morphis

**Submitted in fulfilment of the requirements in respect of the Doctoral Degree  
PhD (Medical Physics) in the Department of Medical Physics in the Faculty of  
Health Sciences at the University of the Free State.**

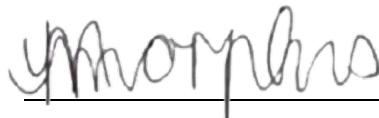
28 July 2021

Promoter: Dr. JA. van Staden  
Co-promoters: Dr. H. du Raan  
Dr. FCP. Du Plessis

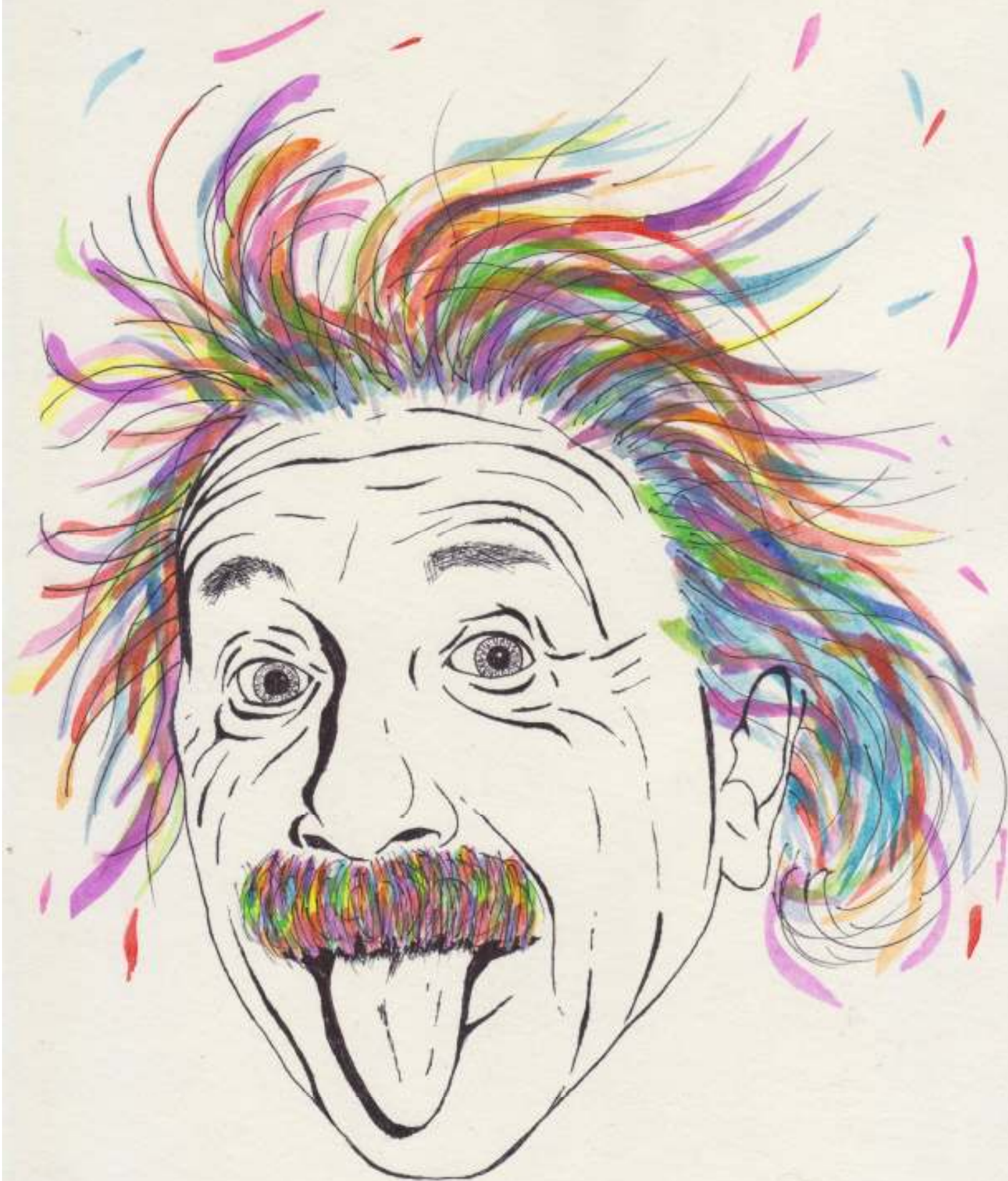
I, Michaella Morphis, declare that the thesis that I herewith submit for the Doctoral Degree PhD (Medical Physics) at the University of the Free State, is my independent work, and that I have not previously submitted it for a qualification at another institution of higher education.

Bloemfontein

28 July 2021

A handwritten signature in black ink, appearing to read 'ymorphis', is written over a horizontal line.

Michaella Morphis



Strive not to be a success, but rather to be of value.  
Albert Einstein

S. REDGARD 2021

## **Acknowledgements**

I wish to show my appreciation to my promoters, Dr Johan van Staden, Dr Hanlie du Raan and Dr Frederik du Plessis, for their guidance and assistance in every step of this journey. Their patience, understanding, and enthusiasm have made a strong impression on me, and I will forever cherish the memories created.

I humbly thank Prof. Michael Ljungberg from Lund University for his invaluable support over the past few years. His immense knowledge, kindness and willingness to help has made this study possible. Working with him and Prof. Katarina Sjögren Gleisner has been an extraordinary experience, for which I am honoured and eternally grateful.

A special thank you to Mrs Keamogetswe Ramonaheng for her continuous support. Getting through this required more than just academic support, so I thank her for her friendship over the years. We did it!

I wish to acknowledge the generous support provided by the High-Performance Computing division at the University of the Free State and the Department of Nuclear Medicine at Universitas Academic Hospital. I extend a thank you to Prof. Charles Herbst for his continued programming assistance.

Finally, I must express my deep appreciation to my parents, sister and brother-in-law for their enduring support and encouragement throughout my studies. And of course my niece and nephew for their unconditional love and much needed distractions of smiles and laughter. I am forever indebted to you all.

# Table of Contents

Abstract.....	vi
Abbreviations.....	viii

Chapter 1:	Introduction
Chapter 2:	Paper I
Chapter 3:	Paper II
Chapter 4:	Paper III
Chapter 5:	Paper IV
Chapter 6:	Summary and future work

## Appendices

Appendix A:	Paper I – front page of published article
Appendix B:	Paper II – front page of published article
Appendix C:	Paper III – front page of published article
Appendix D:	Additional information and results
Appendix E:	Ethics approval letter
Appendix F:	Turnitin report

## **Abstract**

*Introduction:* Theragnostics is a precision medical discipline aiming to individualise patient targeted treatment. It aims at treating cancer by the systemic administration of a therapeutic radiopharmaceutical, which targets specific cells based on the labelling molecule. With the renewed interest in radiopharmaceutical therapy, the importance of accurate image quantification using iodine-123 (I-123) and iodine-131 (I-131), for dosimetry purposes, has been re-emphasised. Monte Carlo (MC) modelling techniques have been used extensively in Nuclear Medicine (NM), playing an essential role in modelling gamma cameras for the assessment of activity quantification accuracy, which is vital for accurate dosimetry.

This thesis aimed to assess the accuracy of patient-specific I-131 dosimetry using hybrid whole-body (WB) planar-SPECT/CT imaging. The study was based on MC simulations of voxel-based digital phantoms, using the SIMIND MC code emulating the Siemens Symbia™ T16 gamma camera. To achieve the aim, the thesis was divided into four objectives, (i) validating the accuracy of an energy resolution (ER) model, (ii) verifying the SIMIND setup for simulation of static, WB planar and SPECT images for I-123 with a low energy high resolution (LEHR) and a medium energy (ME) collimator and for I-131 with a high energy (HE) collimator, (iii) evaluating SPECT quantification accuracy for the three radionuclide-collimator combinations and (iv) assessing the accuracy of I-131 absorbed dose calculations for tumours and organs at risk, based on hybrid WB planar-SPECT/CT imaging.

*Methodology:* The proposed ER model was fit to measured ER values (between 27.0 and 637.0 keV) as a function of photon energy. Measured and simulated energy spectra (in-air, in-scatter and a voxel-based digital patient phantom) were compared. The SIMIND setup was validated by comparing measured and simulated static and WB planar (extrinsic energy spectra, system sensitivity and system spatial resolution in-air and in-scatter), as well as SPECT (simple geometry sensitivity) results. Quantification accuracy was assessed in voxel-based digital simple and patient phantoms, using optimised OS-EM iterative reconstruction updates, calibration factor and recovery curves. Finally, using the true and quantitative activity data from I-123 and I-131 voxel-based digital patient phantoms, full MC radiation transport was performed, to determine the accuracy of the absorbed dose for I-131-mIBG radiopharmaceutical therapy.

*Results:* The fitted ER model better simulated the energy response of the gamma camera, especially for high energy photopeaks, (I-123: 528.9 keV and I-131: 636.9 keV). The measured and simulated system energy spectra (differences  $\leq 4.6$  keV), system sensitivity (differences  $\leq 6.9\%$ ), system spatial resolution (differences  $\leq 6.4\%$ ) and SPECT validation results (difference  $\leq 3.6\%$ ) compared well. Quantification errors less than 6.0% were obtained when appropriate corrections were applied. I-123 LEHR and I-123 ME quantification accuracies compared well (when corrections for septal scatter and penetration are applied), which can be useful in departments that perform I-123 studies and may not have access to ME collimators. Average I-131 absorbed doses of  $2.0 \pm 0.4$  mGy/MBq (liver),  $20.1 \pm 4.0$  mGy/MBq (3.0 cm tumour) and  $22.6 \pm 4.2$  mGy/MBq (5.0 cm tumour) were obtained in simulated patient studies. When using a novel method of replacing the reconstructed activity distribution with a uniform activity distribution, eliminating the Gibbs artefact, the dosimetry accuracy was within 10.5%.

*Conclusion:* Using the proposed fitted ER model, SIMIND could be used to accurately simulate static and WB planar and SPECT projection images of the Siemens Symbia™ T16 SPECT/CT for both I-123 and I-131 with their respective collimators. Accurate quantification resulted in absorbed dose accuracies within 10.5%. The hybrid WB planar-SPECT/CT dosimetry method proved effective for personalised treatment planning of I-131 radiopharmaceutical therapy, with either I-123 or I-131 diagnostic imaging.

*Nuclear Medicine, theragnostics, quantification, dosimetry, Monte Carlo, SPECT/CT, whole-body planar, I-123, I-131, SIMIND, LundADose*

## Abbreviations

2D	Two-dimensional
3D	Three-dimensional
A/P	Anterior and posterior
CDR	Collimator-detector response
CF	Calibration factor
CT	Computed tomography
EPHD	Energy pulse-height distribution
EPHDs	Energy pulse-height distributions
ESSE	Effective scatter source estimate
FWHM	Full width half maximum
FWTM	Full width tenth maximum
GM	Geometric mean
HE	High energy
I-123	Iodine-123
I-131	Iodine-131
LEHR	Low energy high resolution
LSF	Line spread function
LSFs	Line spread functions
Lu-177	Lutetium-177
MC	Monte Carlo
ME	Medium energy
mIBG	Meta-iodobenzylguanidine
MIRD	Medical internal radiation dosimetry
ML-EM	Maximum likelihood-expectation maximisation
NaI	Sodium iodide
NEMA	National electrical manufacturers association
NET	Neuroendocrine tumour
NETs	Neuroendocrine tumours
NM	Nuclear Medicine
NMISA	National metrology institute of South Africa
OS-EM	Ordered subsets-expectation maximization



p.i.	Post injection
PVE	Partial volume effect
PVEs	Partial volume effects
QAD	Quantified SPECT activity distribution
QAD <sub>u</sub>	Quantified SPECT activity uniformly distributed
RC	Recovery coefficient
RCs	Recovery coefficients
ROI	Region of interest
ROIs	Regions of interest
SCD	Source-to-collimator distance
SCDs	Source-to-collimator distances
SD	Standard deviation
SDs	Standard deviations
SIMIND	Simulation of imaging nuclear detectors
SPECT	Single-photon emission computed tomography
TAC	Time activity curve
TACs	Time activity curves
Tc-99m	Technetium-99m
TDC	Time dose-rate curve
TEW	Triple energy window
UAH	Universitas Academic Hospital
UFOV	Useful field of view
VOI	Volume of interest
VOIs	Volumes of interest
WB	Whole-body

# **Chapter 1: Introduction**

# Table of Contents

1.1.	Overview .....	1.2
1.1.1.	Theranostics .....	1.2
1.1.2.	Nuclear Medicine imaging .....	1.3
1.1.3.	Radiopharmaceutical therapy planning .....	1.6
1.1.3.1.	Activity quantification.....	1.6
1.1.3.2.	Dosimetry .....	1.13
1.1.4.	Monte Carlo techniques .....	1.15
1.2.	Thesis rationale.....	1.17
1.3.	Aim and objectives .....	1.17
1.4.	Summary of papers.....	1.18
1.5.	References .....	1.20

## **1.1. Overview**

### **1.1.1. Theragnostics**

Nuclear medicine (NM) makes use of targeted radiopharmaceuticals to image specific physiological or pathological processes. Once the radiopharmaceutical is administered to the patient and imaged over time, the resultant image displays a spatial distribution of the radiopharmaceutical within the patient, detailing the uptake and retention of activity in the patient's organs. NM imaging is a valuable tool for detecting cancer, as most often, cancer affects the functioning of cells, resulting in some form of functional and/or physiological change, which is then visualised on the NM diagnostic image.

For several decades, radionuclides have been used to treat cancer. In 1901, radium-226 was used to treat a tuberculous skin lesion, and in 1936, phosphorous-32 was used for pain relief for patients with metastatic bone lesions, in-vitro to treat leukaemia and for treating polycythaemia vera. The use of phosphorus-32 for the treatment of polycythaemia vera has declined, due to the lack of the radiopharmaceutical's availability. With the discovery of iodine-131 (I-131) in 1938, a new era in medicine emerged. I-131 has been used for diagnostic purposes as far back as 1939, and in 1946 it was used to treat the first patient for thyroid cancer (1), leading to the current era of theragnostics. Theragnostics is a NM technique that takes advantage of radiopharmaceuticals' targeting properties for diagnostic and therapeutic purposes. It aims at treating cancer by the systemic administration of a therapeutic radiopharmaceutical, which targets specific cells based on the labelling molecule (pharmaceutical), allowing for a personalised therapy approach.

Theragnostics is a milestone in cancer treatment, which has bridged the divide between Oncotherapy and NM. The principle of theragnostics lies in the combination of targeted cancer imaging (diagnostics) and therapy (2). To allow for visualisation of potential targets, both the diagnostic imaging and therapy procedure typically use the same radiopharmaceutical, however, in some cases, the radionuclide may differ. Several theragnostic radionuclide pairs (strontium-83/strontium-89, yttrium-86/yttrium90 and copper-64/copper-67) are used, making it possible to estimate potential toxicities and predict the benefits of such therapy (3,4).

Since theragnostics is a precision medical discipline aiming to individualised patient targeted treatment, the importance of accurate image quantification using I-131 and iodine-123 (I-123) has been re-emphasised (3,5,6).

I-131, with a physical half-life of 8.04 days, emits both gamma photons (284.3 keV, 364.5 keV, 636.9 keV and 722.9 keV) and beta particles (maximum and mean energy: 606.0 keV and 192.0 keV) (7). In contrast, I-123 emits gamma photons (159.0 keV, 528.9 keV) as well as characteristic x-rays (27.3 keV) and has a physical half-life of 13.2 hours, making I-123 ideal for diagnostic imaging. Furthermore, I-123 has been promoted for diagnostic imaging for treatment with I-131, to avoid stunting of tumour growth. Since the biodistribution of I-123 and I-131 in the body are similar, I-123 can be used as a surrogate for I-131 in the I-131 treatment planning process. Furthermore, I-123 carries a reduced radiation burden compared to I-131 due to its shorter half-life and lack of beta particles; therefore, higher quantities of I-123 can be administered for diagnostic purposes.

Due to the natural accumulation of iodine in the thyroid, I-123 and I-131 are routinely used in diagnostic and therapeutic thyroid studies (8). However, it has gained popularity in treating non-Hodgkin lymphomas and neuroendocrine tumours (NETs) when attached to a pharmaceutical. I-131 labelled to tositumomab, a monoclonal antibody protein, is typically used to image and treat non-Hodgkins lymphoma (9). Both I-131 and I-123 can be labelled to a noradrenaline analogue, meta-iodobenzylguanidine (mIBG), and used to detect and treat NETs. I-131-mIBG and I-123-mIBG naturally accumulate in NETs as well as the lungs, liver, kidneys, spleen, bladder, bone marrow and salivary glands (10,11).

### **1.1.2. Nuclear Medicine imaging**

The most important application of radiation in NM is radionuclide imaging. As mentioned, once the radiopharmaceutical is administered to the patient, it can be imaged with a gamma camera, and the resultant image will display a spatial distribution of the radiopharmaceutical within the patient, detailing the uptake and retention of activity in the patient's organs.

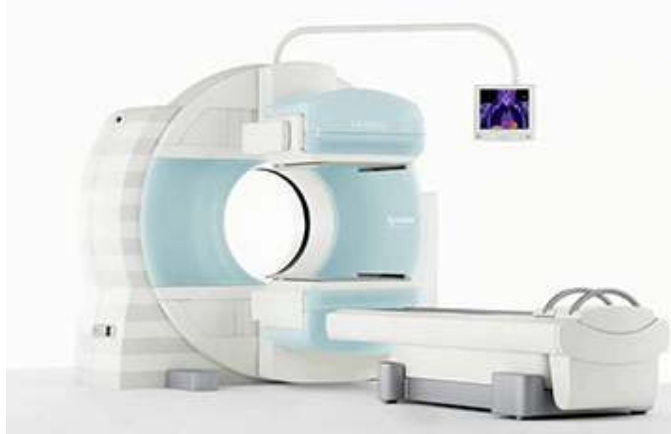


**Figure 1.1.** Siemens Symbia dual-head gamma camera (12).

The general components and basic principles of the gamma camera are shown in Figure 1.2. Photons emitted from the patient and have passed through the collimators are detected by the scintillation detector. Here, the energy of the photon is converted to light, which is then detected and amplified by the photomultiplier tubes, generating an electronic signal. The energy and positional information are used to form a digital image. Corrections for energy, linearity and uniformity can be applied to the digital image.

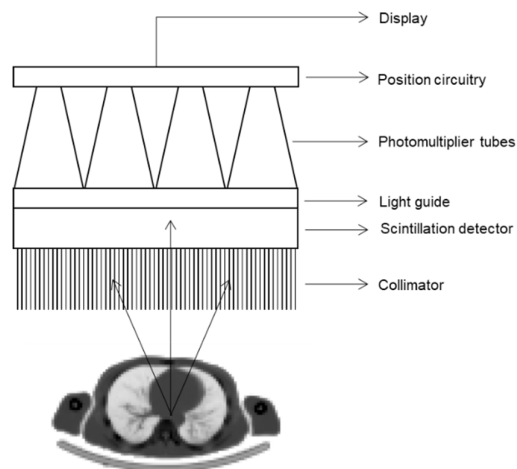


**Figure 1.2.** Basic principles and components of a gamma camera.

The collimator, constructed from lead sheets, only allows for photons travelling parallel to the collimator holes, to pass through. The choice of collimator depends on the radionuclide used, the size of the organ to be imaged, as well as if high-resolution or high-sensitivity is of

interest in the study being performed. The parallel-hole collimator is used in most routine NM studies. Thus, collimators are designed and constructed for a specific photon energy range. The choice of collimator is vital when evaluating quantification accuracy. Imaging I-131 with a high energy (HE) collimator is well established (13), as it minimises the effect of collimator septal scatter and penetration. However, either a low energy high resolution (LEHR) collimator or a medium energy (ME) collimator can be used for I-123 imaging. The effects of collimator septal scatter and penetration, from I-123 high-energy photons, are reduced with a ME collimator, resulting in images with improved contrast, and is thus ideal when quantitatively accurate images are required (14). The LEHR collimator can provide superior spatial resolution images, but only if appropriate collimator septal scatter and penetration corrections are applied (14,15). Simulated whole-body (WB) images (shoulder to thigh) obtained with different radionuclide-collimator combinations are shown in Figure 1.3.

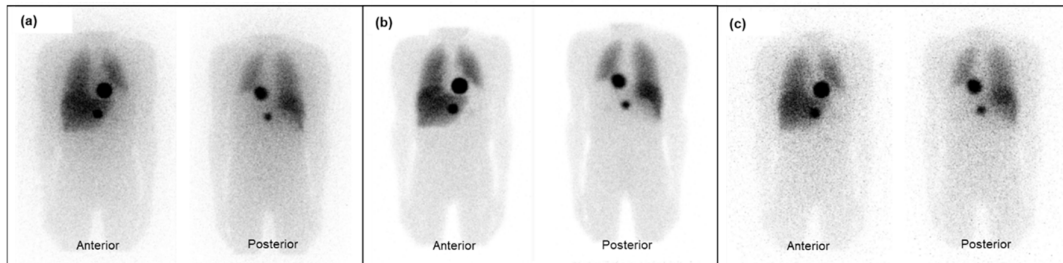


**Figure 1.3.** Simulated WB images of (a) I-123 LEHR, (b) I-123 ME and (c) I-131 HE.

When performing imaging for radiopharmaceutical therapy planning purposes, the gamma camera acquisition mode is important. Acquisition modes, amongst others, include WB planar and single-photon emission computed tomography (SPECT) imaging.

The process of WB planar imaging is relatively simple; it involves the acquisition of a series of two-dimensional (2D) WB anterior and posterior (A/P) planar images. Typically, imaging is performed at fixed time intervals, tracking the biodistribution of the radiopharmaceutical in the patient as it is washed out (biological washout).

Due to limitations of planar imaging, namely, its lack of depth resolution and superimposition of over- and underlying tissues, its use in absolute quantification can be challenging. The effect of the over- and underlying tissue is solved with SPECT imaging, making it the preferred acquisition mode when accurate dosimetry is required in therapeutic NM applications. During SPECT imaging, multiple image projections are acquired at fixed

angular increments around the patient. These images are then reconstructed to create a three-dimensional (3D) distribution of activity in the patient. If appropriate corrections for scatter, attenuation and collimator-detector response (CDR) are applied, each voxel represents the amount of activity located at that position in the patient (16). The corrections are discussed in Section 1.1.3.1 (ii).

### **1.1.3. Radiopharmaceutical therapy planning**

Radiopharmaceutical therapy planning is founded on two fundamental processes: activity quantification and absorbed dose calculations (dosimetry).

#### **1.1.3.1. Activity quantification**

Identifying the radiopharmaceutical distribution within the body and quantifying the amount of activity taken up by tumours and organs at risk from a NM image is termed activity quantification. The accuracy with which activity can be quantified influences the accuracy with which dose calculations can be performed.

##### **i. Planar quantification**

One of the earliest and currently the most common method of activity quantification is the planar conjugate-view technique (two opposing projections as shown in Figure 1.3). Typically, WB planar images are acquired at three or four timepoints during the first week after administration (4). Factors such as attenuation, scatter, over-and under-lying tissues and background effects need to be corrected to yield accurate results.

##### Attenuation Correction

When using the conjugate view technique, the difference in the count distribution in the two opposite projections is a function of photon attenuation, thus, making the depth of the source in the patient vital for accurate attenuation correction. When the geometric-mean (GM) of the two opposing projections is determined, the source depth is averaged. Thus, the attenuation correction factor becomes a function of patient thickness only, easily determined from a transmission image. It is important to note that the conjugate view technique is only exact for a point or plane source (17). An alternative method for determining patient-specific attenuation maps, using computed tomography (CT) information, has been developed (18). This method makes use of a CT scout image, converted to a transmission image (Figure 1.4). The higher photon flux of the CT scout image allows for an improved signal-to-noise ratio compared to a radionuclide



transmission image, making it possible to acquire a scout image post-radiopharmaceutical administration. In addition, acquiring a scout image in succession to the NM WB image allows for better spatial registration of the two images. Not only is the scan time for a scout image short in comparison to a radionuclide transmission image, but it also provides good spatial resolution, allowing for accurate delineation of most organs. Typically, CT scout images are used qualitatively to define the axial scan range for a CT scan. To use the images quantitatively for attenuation correction, they need to be rescaled to transmission values. A patient-weight based method can be used to determine the scaling factor (4). This method of attenuation correction with planar imaging has proven successful (18). However, in scenarios where a CT scout is unavailable, 3D CT data can be used to generate a scout image.

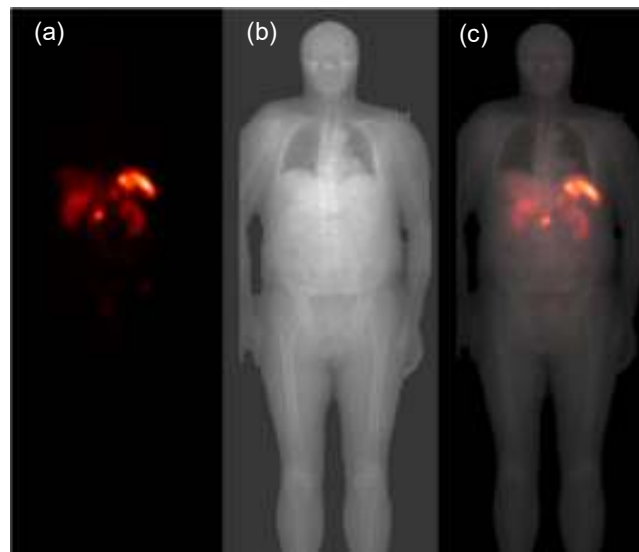


**Figure 1.4.** An example of a CT scout used for WB planar attenuation correction for Lu-177-Dotatate therapy. (a) Anterior image of the WB activity distribution, (b) patient CT scout, and (c) fused images of the activity distribution and the CT scout image (4).

### Scatter Correction

Several approaches to scatter correction in planar imaging have been taken. Scatter correction methods include using an effective attenuation coefficient in the GM method or applying the triple energy window (TEW) method. Ogawa et al. proposed the TEW method of scatter correction in 1991 (19). It makes use of two scatter windows, one on either side of the photopeak. The information from these two windows is used to estimate the amount of scatter in the primary window and then subtracted from the

primary photopeak data for each pixel. An alternative scatter correction method uses a Wiener filter, utilising scatter kernels based on scatter point-spread functions (6). The scatter kernels are precalculated using Monte Carlo (MC) simulations of a point source in a water-filled elliptical phantom. The kernels are a function of source depth and are normalised to compensate for scatter quantitatively. This form of scatter correction also acts as a sharpening filter. The downside of this method is that the kernels are only calculated in water and not for other tissue-equivalent materials. Nevertheless, it has proven successful with planar imaging (4,6,16) and was thus the chosen method for this study.

#### Region of Interest and Calibration Factor

For accurate quantification, regions of interest (ROIs) must be defined correctly. Typically, the CT scout image is used to assist in organ delineation. WB planar images must be registered to the WB CT scout image to ensure accurate ROI definition. The purpose of image registration is to transform the sequence of images geometrically, ensuring the pixel values in each of the images represent the same position in the patient. A single set of ROIs can be used to delineate multiple WB planar images if registered correctly. Once a set of ROIs is defined, count statistics can be obtained.

The basis of absolute quantification is that image information be proportional to activity. A calibration factor (CF) is used to convert the number of counts in a region of interest (ROI) to units of activity. The most straightforward calibration procedure utilises a planar acquisition of a point source in air, from which an 'in-air sensitivity' value, with negligible scatter and attenuation, is assumed (20).

#### Partial Volume Effect Correction

The partial volume effect (PVE) is caused by the limited spatial resolution of the imaging device and the sampling frequency. Objects with sizes below approximately twice the full width half maximum (FWHM) of the spatial resolution are likely to be degraded (17). As a result, the activity is underestimated. This occurs when activity from the ROI is lost to its surroundings, decreasing the amount of activity within that ROI (spill-out). Overestimation of activity in a ROI occurs when activity outside the ROI adds to its activity, increasing the amount of activity within that ROI (spill-in). In both cases, it is assumed that the ROI perfectly delineates the structure to be quantified.

In summary, the PVE results in the gain or loss of counts from a specific region. If there are structures with activity uptake close to the ROI, the spill-out of activity from these structures can increase counts in adjacent ROIs (17). The degree of the PVE depends on several factors: system spatial resolution, patient motion (including respiratory motion) and the distribution of activity. Performance characteristics of the collimator and the detectors' intrinsic resolution may influence the systems' spatial resolution. The intrinsic resolution is affected by radionuclide energy and crystal thickness. With an increase in photopeak energy and a decrease in the crystal's thickness, the intrinsic resolution will improve. The collimator, however, plays the most significant role in determining the system spatial resolution (21). A simple approach to correct for the PVE would be to estimate the recovery coefficients (RCs) for different sized objects within a phantom and then generate a recovery coefficient (RC) curve. A RC is the ratio of the recovered activity concentration ( $[A]_{recovered}$ ), to the true activity concentration ( $[A]_{true}$ ), as seen in the equation below,

$$RC = \frac{[A]_{recovered}}{[A]_{true}} \quad (1.1)$$

where

$$[A]_{recovered} = \frac{\text{average radioactivity in volume}}{\text{volume}} \quad (1.2)$$

An RC curve of the RC versus object diameter ( $x$ ) can be plotted, and a function with the form

$$RC = a - be^{-cx} \quad (1.3)$$

can be fitted to the data, allowing for interpolation between object sizes. The RC can subsequently be applied in calculating the true amount of activity within the structures (23,24,25).

### Time Activity Curves

A time activity curve (TAC) is created by plotting the activity in a ROI to the corresponding timepoint. The objective of a TAC is to describe the pharmacokinetics of the radiopharmaceutical during the total time it resides in the source organ. Integrating the TAC gives a value that corresponds to the cumulated activity, from which the absorbed dose to the target organ can be calculated. The pharmacokinetics of the radiopharmaceutical depends on both the physical (decay) and biological (washout) half-life of the radiopharmaceutical. Not only does the pharmacokinetics differ from organ to

organ, but there is considerable inter-patient variability. Since these curves influence the calculated absorbed dose, they must be determined for each source organ in individual patients, allowing for personalised treatment planning (4,16).

## ii. SPECT/CT quantification

SPECT is favoured over planar imaging, as it results in more accurate activity quantification leading to improved dosimetry, despite being considered more time-consuming. As mentioned, certain correction factors must be applied to ensure improved quantification accuracy. These correction factors are similar to those discussed for planar quantification, with the differences discussed below.

### Attenuation Correction

CT images are typically used for attenuation correction, with SPECT/CT imaging (17). This is equivalent to using a transmission scan in planar imaging, although image quality, specifically image contrast is improved when CT images are used (17,22). A CT image is typically expressed in Hounsfield units (also referred to as CT numbers) and needs to be converted to linear attenuation coefficients. This should be performed for the specific photon energy of the emission radionuclide used (22). The conversion of CT numbers to linear attenuation coefficients is performed using a bi-linear model, which is based on measurements acquired with the Gammex RMI-465 phantom (25–27). An attenuation map representing the spatial distribution of linear attenuation coefficients in the ROI is generated and integrated into a reconstruction algorithm (28). This method of attenuation correction is adopted by most manufacturers and is the method of choice.

### Scatter Correction

As mentioned, several methods can be used to correct for Compton scatter in NM imaging. One such method recommended for SPECT imaging is the reconstruction-based scatter compensation method. This method allows for accurate modelling of full 3D spatial scatter response. Scatter response functions are modelled in an iterative reconstruction algorithm, mapping the path of the scattered photon (29). The effective scatter source estimate (ESSE) method (30) is a successful example of the reconstruction-based scatter compensation method. It uses precalculated MC based scatter kernels which are used to estimate the scatter in the photopeak window. Scatter kernels are simulated for the specific radionuclides with defined energy window settings and system energy resolution (16). The advantage of this method is that the modelled

scatter component better reflects the distribution of the true scatter in the photopeak compared to the energy window-based correction techniques. As for scatter correction in planar imaging, the disadvantage is that the kernels are only calculated in water and not for other tissue-equivalent materials.

#### Collimator-detector Response Correction

The gamma camera's spatial resolution is characterised by the spread of the profile obtained from an image of a point source. Spatial resolution is defined as the FWHM of the point spread function. It depends linearly on the distance between the source and the detector for a gamma camera employing absorptive parallel-hole collimation. This effect, known as the CDR, can be incorporated into the reconstruction algorithm (22). Compensating for the CDR in SPECT is essential for accurate quantification. CDR includes three components: a collimator scatter response, a geometric response as well as a septal penetration response. The geometric response can be modelled analytically, and this is the method of choice when the geometric response dominates, as with the lower photon energy emitting radionuclides, such as technetium-99m. With higher photon energy emitting radionuclides, such as with I-131 and to a certain extent I-123, septal penetration and collimator scatter response is significant. Thus it needs to be modelled in the CDR correction (31). The spatial resolution of the collimator is modelled so that the spatial resolution in the axial and transverse planes are equivalent, maintaining the precise shape of lesions. Recovery of resolution means that images of small lesions will be reconstructed with more interaction events positioned spatially correct, increasing image contrast, thus partially correcting for PVE (32). It is ideal to use precalculated MC-based kernels in which the effects from septal penetration, collimator scatter, and scatter from detector housing and electronics are considered (16).

#### Volume of Interest Definition and Calibration Factor

As with the definition of ROI in planar imaging, volumes of interest (VOIs) must be defined accurately to obtain accurate quantification results. CT imaging is typically used in conjunction with SPECT images to define VOIs. SPECT/CT systems generally provide registered SPECT and CT images; however, when SPECT/CT images are acquired at multiple timepoints, it is helpful to define a single set of VOIs and apply them to subsequent datasets. Count statistics can now be obtained for several VOIs from multiple timepoints (4,16).

However, as with planar quantification, a CF is needed to convert counts to units of activity. In contrast to planar imaging, there is merit in mimicking the clinical scenario when calculating a CF. Using a sphere (to mimic a tumour) in a water phantom, that approximates scatter and attenuation conditions in patient imaging, may be more suited (33). A calibration procedure based on a sphere in a cylindrical phantom has been proposed previously (13,34). The acquisition procedure and corrections applied are the same as those for routine patient imaging. The CF ultimately represents a system volume sensitivity. This can be incorporated into the reconstruction process, resulting in images representing activity distribution rather than count distribution. Activity values for each volume of interest (VOI), representing each organ at risk and tumour, can be obtained for each timepoint.

#### Partial Volume Effect Correction

An effective technique for improving PVE on reconstructed SPECT images is incorporating resolution recovery, by means of CDR correction, into the reconstruction algorithm. This option is available on most SPECT systems. It is mainly used to improve image resolution, resulting in a more quantitatively accurate image; however, residual partial volume effects (PVEs) will still be present. At best, PVEs are reduced in magnitude, provided a sufficient number of iterations are performed (21). A simple approach to correct the residual PVEs would be to estimate RCs for specific geometries (varying object size) within a phantom and then generate an RC curve, as described for planar imaging.

#### Time Activity Curves

A TAC can be created, similar to that for planar imaging, by plotting the activity in a VOI to the corresponding timepoint. SPECT/CT derived time activity curves (TACs) are considered quantitatively more accurate, thus should result in a more accurate absorbed dose estimation (4).

### **iii. Hybrid WB planar-SPECT/CT**

The downfall of planar imaging is its poor image contrast. This is overcome with tomographic SPECT imaging, allowing for improved quantification accuracy. However, a drawback of SPECT imaging for quantification purposes is its limited axial range of imaging. To perform SPECT imaging covering the WB of the patient would be impractical, as acquisition times are long. Conducting multiple WB SPECT studies per

patient in most clinics would be challenging due to a large patient load. Using a combination of WB planar and SPECT/CT imaging, one can take advantage of the effectiveness and speed of WB planar imaging with the improved quantification accuracy of SPECT/CT imaging. This hybrid method of imaging is beneficial in institutions with large patient throughput, resulting in quantification accuracies similar to that for SPECT/CT but with the speed of planar imaging. This method involves acquiring multiple WB planar images over a period of time, which are processed using the GM and corrections for scatter, attenuation and background activity. A single SPECT/CT study is acquired in combination with a WB study at a single timepoint. The construction of the TAC for each source organ is obtained by combining WB planar and SPECT/CT information. The typical shape of the TAC is determined from the series of WB planar images. The curve is then scaled to the quantified activity determined from the single SPECT/CT timepoint. The assumption made is that quantitative SPECT/CT data is more accurate than data obtained from WB planar images. The scaling factor is a simple ratio between the activities obtained from the WB planar and quantified SPECT studies at the same timepoint. This factor is then applied to all other timepoints, ultimately adjusting the amplitude of the TAC (4, 16). Studies show that hybrid methods perform better than purely planar-based methods and are comparable to fully SPECT/CT methods (35). For the hybrid method to be successful, patients must fall in the selection criteria. Three factors should be considered before performing hybrid WB planar-SPECT/CT quantification, namely; (i) there should be minimal overlap between ROIs with high activity uptake in WB planar images, (ii) the ROI should be included in the SPECT/CT study, and lastly, (iii) ROI uptake and boundaries should be visible on the WB planar image (35). If these criteria are met, this method of quantification can be performed.

### **1.1.3.2. Dosimetry**

It is useful to know the absorbed dose to tumours and organs at risk, especially when evaluating the radiobiological effect of radiopharmaceutical therapy (36).

Internal radiation dosimetry is used to describe the calculation of energy deposited by internal radionuclides in organs. The most commonly used method for performing internal radiation dosimetry is the method proposed by the Medical Internal Radiation Dosimetry (MIRD) Committee of the Society of Nuclear Medicine (37). This method is versatile in calculating the absorbed dose to selected organs as well as to the WB. MIRD considers variables

associated with the deposition of ionising radiation and those associated with the biological system for which dose is calculated. The MIRD formalism describes the mean absorbed dose to a particular target organ,  $Dr_k$ , as follows,

$$\overline{Dr_k} = \sum_h \widetilde{A}_h S(r_k \leftarrow r_h) \quad (1.4)$$

where  $r_h$  is the source organ,  $r_k$  is the target organ,  $\widetilde{A}_h$  is the cumulated activity for each source organ, and  $S$  is the mean absorbed dose per cumulated activity from the source organ to the target organ. The  $S$  value depends on the type and energy of the radiation, the size, shape and composition of the target and source organs, and the distance between them. Typical  $S$  values for multiple target and source organs for a range of radionuclides have been published in MIRD pamphlet 11 (38, 39).

The cumulated activity is the total number of disintegrations from the radionuclide located in a source organ. As mentioned, it can be calculated from as the area under the TAC. For pure exponential biological washout the cumulated activity in a source organ,  $\widetilde{A}_h$ , can be expressed as follows,

$$\widetilde{A}_h = A_0 \cdot f_h \cdot \tau \quad (1.5)$$

where  $A_0$  is the initial administered activity,  $f_h$  the fractional uptake and  $\tau$  is the so-called "average lifetime" or residence time in the source organ, which is defined as follows,

$$\tau = \frac{T_e}{\ln 2} \quad (1.6)$$

where  $T_e$  is the effective half-life of the radiopharmaceutical. The cumulated activity in a source organ, when eliminated by physical decay only, is the same as if the activity was present at a constant level  $A_0$  for a time equal to the average lifetime ( $\tau$ ) of the radionuclide. Cumulated activity depends on the amount of activity taken up by the source organ and the rate of elimination from the source organ. The rate of elimination is dependent on  $T_e$ . It can be determined by two factors, namely the biological half-life ( $T_B$ ) and the physical half-life ( $T_p$ ). The effective half-life is defined as follows (17),

$$T_e = \frac{T_p \cdot T_B}{T_p + T_B} \quad (1.7)$$

The  $S$  values used in the MIRD method are based on simplified assumptions that provide an estimated dose to an average adult, adolescent, child or foetus. This limits the effectiveness of



MIRD as organ shape, size, and position vary considerably from patient to patient (40). An alternative method based on MC radiation transport can be adopted to overcome the shortcomings of the MIRD method.

Full MC radiation transport is the most accurate method for patient-specific 3D absorbed dose calculations; however, it is not well established in the clinic, as it is relatively time-consuming (16). It uses quantitative NM images together with registered density maps to model radiation transport in the patient. The process involves sampling decay locations from the quantified NM images, assuming each voxel value indicates activity at a specific location in the patient, corresponding to the voxel location. The transport of photons and electrons are simulated based on the CT density map, and the energy deposited at each interaction site is mapped on a separate matrix, equivalent to that of the NM image. This matrix then indicates the absorbed dose in the patient.

The NM images required to perform MC dosimetry can either be planar (static or WB), SPECT/CT or a combination of planar and SPECT/CT images (16). Using hybrid WB planar-SPECT/CT quantification for dosimetry, one can take advantage of the high accuracy in 3D imaging and the minimal effort required for planar imaging (41).

#### **1.1.4. Monte Carlo techniques**

MC techniques have played an essential role in the NM discipline. They have become a method of choice to optimise instrumentation and clinical protocols, enhance image correction techniques, and develop and implement patient-specific dosimetry (42). MC simulations allow researchers to investigate what influence a parameter has on a system's performance in a way that otherwise is difficult or even impossible to measure (43). The MC method has been applied extensively in modelling gamma cameras for radionuclides, including technetium-99m, I-131 and lutetium-177 (13,20,44). There are various MC simulation codes available for NM imaging, such as Simulation of imaging nuclear detectors (SIMIND), SimSET and GATE (43,45–47).

In this work, the SIMIND MC code (48) was used to simulate WB planar and SPECT images. This program models a standard clinical SPECT gamma camera, and with simple modifications it can be used to perform a variety of calculations or measurements typically encountered in NM imaging. There are two main programs which can be run, namely, CHANGE and SIMIND. CHANGE allows the user to define the gamma camera to be

modelled and the experimental setup to be simulated. This data is then written to an external data file. SIMIND reads the input parameters created by CHANGE, and the actual simulation is performed. The progress and a summary of the simulation results are displayed on the screen, and several output files, including the simulated images, are saved. Considering MC simulations are by default tedious and time-consuming, SIMIND also provides a more efficient way of performing simulations by preparing a command file which allows a series of simulations to be run consecutively (49).

SIMIND allows the use of not only analytical but also digital models, which are specially designed objects that can be used for various purposes, from testing the effectiveness of a new detector system to simulating new pharmaceuticals. By using digital models, more controlled and consistent results can be obtained, in contrast to when using living subjects. Furthermore, there are no radiation risks to patients or staff when using digital models. It is, however, important that the models must mimic the response of human tissue (50). CT systems are used to produce high-resolution 3D images of physical phantoms or patients. These images give a good measure of the distribution of attenuating material within the phantom or patient. The CT dataset can be used to create a voxel-based digital model of the phantom or patient, where the CT numbers are used to assign a predetermined value to each voxel in a structure, organ or tissue. The process is known as segmentation and results in a single value being assigned to regions of similar density, thus eliminating small pixel to pixel variations, producing an image where like densities are represented as uniform. The use of voxel-based digital phantoms in MC simulations has become more important. It can be used to produce more realistic images of the internal distribution of radiopharmaceuticals in clinical studies (49,51).

LundADose is a MC-based dosimetry package developed by a team at the University of Lund in Sweden (52). It contains SPECT/CT voxel-based dosimetry methods, including ordered subsets-expectation maximisation (OS-EM) SPECT image reconstruction with corrections for attenuation, scatter and collimator detector response. It allows for deformable image registration as well as MC-based absorbed dose calculations. It also contains methods for WB planar dosimetry, including image-based activity quantification on a pixel-by-pixel basis, based on the conjugate view method, with appropriate corrections for attenuation, scatter and background. This software has successfully been used in patient-specific radiopharmaceutical therapy planning (52,53) and was used in this study.

## **1.2. Thesis rationale**

The goal of any radiation treatment is to deliver a lethal dose of radiation to tumour cells whilst maintaining safe levels of radiation to surrounding normal tissue. In external beam radiation therapy, as well as for brachytherapy, routine patient-specific treatment planning is performed. However, this is not the case in NM (54). Fixed levels of therapeutic radionuclides are often administered to all patients, with the idea that "one size fits all". This may lead to poor tumour control and, in some cases, high levels of normal tissue complications (3). Tailored radiopharmaceutical therapy planning aims at predicting the amount of activity to be administered to an individual, ensuring optimal tumour control whilst sparing surrounding normal tissues. For this reason, tailored radiopharmaceutical therapy planning should be mandatory, and with the introduction of theragnostics and significant technological improvements, it is now possible (3,4). Results from a European survey, on the implementation of dosimetry in the practice of molecular radiotherapy, showed that 59.0% of the 208 centres participating in the study, provide I-131-mIBG therapies, with some level of dosimetry, and only 18.0% employ dosimetry-based activity prescriptions (55,56).

This leads to the intention of this study, which was to introduce hybrid WB planar-SPECT/CT based dosimetry to Universitas Academic Hospital (UAH) in Bloemfontein, South Africa. As mentioned previously, in most clinics, performing multiple WB SPECT/CT imaging per patient for dosimetry purposes is impractical and nearly impossible due to the large patient load. Using a combination of WB planar and SPECT/CT imaging, one can take advantage of the effectiveness and speed of WB planar imaging with the improved quantification accuracy of SPECT/CT imaging. This hybrid method of imaging is beneficial in institutions with large patient throughput, resulting in quantitative accuracies similar to that obtained from full SPECT/CT imaging, with the speed of WB planar imaging.

## **1.3. Aim and objectives**

This thesis aimed to assess the accuracy of patient-specific dosimetry in I-131 therapy using hybrid WB planar-SPECT/CT imaging. The study was based on MC simulations of voxel-based digital phantoms, using the SIMIND MC code emulating the Siemens Symbia T16 dual-head gamma camera.

The following objectives were considered and presented in four papers,

- I. Validation of the accuracy of an energy resolution model for SIMIND
- II. Setup and verification of the SIMIND MC simulator for both I-123 (LEHR and ME collimator) and I-131 (HE collimator)
- III. Assess the accuracy of activity quantification for WB planar and SPECT images, for both I-123 (LEHR and ME collimator) and I-131 (HE collimator)
- IV. Evaluation of the accuracy of absorbed dose calculations for tumours and organs at risk, based on hybrid WB planar-SPECT/CT imaging, using quantification data of both I-123 (LEHR and ME collimator) and I-131 (HE collimator) to predict the absorbed dose for I-131-mIBG radiopharmaceutical therapy, using LundADose.

#### **1.4. Summary of papers**

Papers I to IV, summarised below, form the basis of Chapters 2 to 5.

##### ***Paper I: Modelling of energy-dependent spectral resolution for SPECT Monte Carlo simulations using SIMIND***

When making use of MC simulation software, it is essential to ensure that the intrinsic characteristics of the imaging system are defined correctly. One such characteristic is the energy resolution, which is described as the system's ability to distinguish between two radiation energies with a small energy difference. The purpose of this article was to validate the accuracy of an energy resolution model for the SIMIND MC code emulating the Siemens Symbia T16 dual-head gamma camera. This was achieved by fitting the proposed energy resolution model to measured energy resolution values as a function of photon energy, ranging between 27.0 and 637.0 keV. The accuracy of the fitted model was then validated by comparing measured and simulated energy spectra obtained from in-air and in-scatter measurements. Finally, the energy spectra from radionuclides simulated in a voxel-based digital patient phantom were compared and evaluated. This paper includes work that has been published in *Heliyon* (57). The front page of the article is shown in Appendix A.

**Paper II: Validation of a SIMIND Monte Carlo modelled gamma camera for Iodine-123 and Iodine-131 imaging**

The goal of this article was to validate the SIMIND modelled Siemens Symbia T16 dual-head gamma camera for I-123 using both the LEHR and ME collimators and I-131 using the HE collimator. This paper includes work that has been published in *Heliyon* (58). The front page of the article is shown in Appendix B.

**Paper III: Evaluation of Iodine-123 and Iodine-131 SPECT activity quantification: A Monte Carlo Study**

The purpose of this article was to develop and evaluate a SPECT activity quantification method for I-123 with the LEHR and ME collimators and I-131 with the HE collimator. This was achieved by optimising the number of OS-EM updates for the SPECT iterative reconstruction algorithm and the CF, determining appropriate RC curves, and validating the quantitative method with voxel-based digital simple and patient phantoms. This paper includes work that has been published in *European Journal of Nuclear Medicine and Molecular Imaging Physics* (59). The front page of the article is shown in Appendix C.

**Paper IV: Accuracy of patient-specific dosimetry using hybrid planar-SPECT/CT imaging**

The goal of this article was to assess the accuracy of patient-specific absorbed dose calculations for tumours and organs at risk based on hybrid WB planar-SPECT/CT imaging. The study used the true and quantitative activity data from both I-123, and I-131 MC simulated voxel-based digital patient phantoms to determine the accuracy of the absorbed dose for I-131-mIBG radiopharmaceutical therapy. A novel method of replacing the reconstructed quantified activity distribution with a uniform activity distribution, thereby eliminating the Gibbs artefacts, was proposed, and led to accurate dosimetry results. Furthermore, absorbed dose values to the liver and tumours were evaluated when dosimetry simulations were performed with both photon and beta interactions, as well as with beta interactions only. This paper is a publishable manuscript and is being finalised for submission for publication.

## 1.5. References

1. SNMMI. Historical Timeline. Available from: <https://www.snmmi.org/AboutSNMMI/Content.aspx?ItemNumber=4175> [accessed 08/06/2021]
2. Frangos S, Buscombe JR. Why should we be concerned about a “g”? *Eur J Nucl Med Mol Imaging*. 2019;46:519. doi: 10.1007/s00259-018-4204-z
3. Yordanova A, Eppard E, Kürpig S, Bundschuh RA, Schönberger S, Gonzalez-Carmona M. Theranostics in nuclear medicine practice. *Onco Targets Ther*. 2017;10:4821–8. doi: 10.2147/ott.s140671
4. Ljungberg M, Gleisner K. Hybrid Imaging for Patient-Specific Dosimetry in Radionuclide Therapy. *Diagnostics*. 2015;5(3):296–317. doi: 10.3390/diagnostics5030296
5. Silberstein E. Radioiodine : The Classic Theranostic Agent. *Semin Nucl Med*. 2012;42(3):164–70. doi: 10.1053/j.semnuclmed.2011.12.002
6. Sjögreen K, Ljungberg M, Strand S, Library PM. An activity quantification method based on registration of CT and whole-body scintillation camera images, with application to I-131. *J Nucl Med*. 2002;43(7):972–82. doi: 10.1.1.580.371
7. Kellett M, Arinc A, Bé M, Browne E, Chechev V, Chisté V. Laboratoire National Henri Becquerel. 2017. Available from: <http://www.lnhb.fr/en/> [accessed 17/06/2020]
8. Thomas SR. Options for radionuclide therapy: from fixed activity to patient- specific treatment planning. *Cancer BiotherRadiopharm*. 2002;17(1084-9785 SB-IM):71–82. doi: /10.1089/10849780252824091
9. Findlay VJ. Tositumomab. In: Enna S, Bylund D, editors. *xPharm: The Comprehensive Pharmacology Reference*. Elsevier; 2007. p. 1–4.
10. Bombardieri E, Giammarile F, Aktolun C, Baum RP, Bischof Delaloye A, Maffioli L. <sup>131</sup>I/<sup>123</sup>I-Metaiodobenzylguanidine (mIBG) scintigraphy: Procedure guidelines for tumour imaging. *Eur J Nucl Med Mol Imaging*. 2010;37(12):2436–46. doi: 10.1007/s00259-010-1545-7

11. Giammarile F, Chiti A, Lassmann M, Brans B, Flux G. EANM procedure guidelines for  $^{131}\text{I}$ -meta-iodobenzylguanidine ( $^{131}\text{I}$ -mIBG) therapy. *Eur J Nucl Med Mol Imaging*. 2008;35(5):1039–47. doi: 10.1007/s00259-008-0715-3
12. Siemens. Symbia S and T System Specifications. 2010. Available from: [www.siemens.com/healthcare](http://www.siemens.com/healthcare). [accessed 23/03/2020]
13. Dewaraja YK, Ljungberg M, Green AJ, Zanzonico PB, Frey EC. MIRD Pamphlet No. 24: Guidelines for Quantitative  $^{131}\text{I}$  SPECT in Dosimetry Applications. *J Nucl Med*. 2013;54(12):2182–9. doi: 10.2967/jnumed.113.122390
14. Rault E, Vandenberghe S, Holen R Van, Beenhouwer J De, Staelens S, Lemahieu I. Comparison of image quality of different iodine isotopes (  $\text{I-123}$  ,  $\text{I-124}$  , and  $\text{I-131}$  ). *Cancer Biother Radiopharm*. 2007;22(3). doi: 10.1089/cbr.2006.323
15. Dobbeleir AA, Hamb AE. Influence of high-energy photons on the spectrum of iodine-123 with low- and medium-energy collimators : consequences for imaging with  $^{123}\text{I}$ -labelled compounds in clinical practice. *Eur J Nucl Med*. 1999;26(6):655–8. doi: 10.1007/s002590050434
16. Ljungberg M, Sjögreen Gleisner K. Personalized Dosimetry for Radionuclide Therapy Using Molecular Imaging Tools. *Biomedicines*. 2016;4(4):25. doi: 10.3390/biomedicines4040025
17. Cherry SR, Sorenson J, Phelps ME, Methé BM. *Physics in Nuclear Medicine*. 4<sup>th</sup> ed. Philadelphia: Saunders; 2012. 1–544 p.
18. Gleisner KS, Ljungberg M. Patient-Specific Whole-Body Attenuation Correction Maps from a CT System for Conjugate-View-Based Activity Quantification: Method Development and Evaluation. *Cancer Biother Radiopharm*. 2012;27(10):652–64. doi: 10.1089/cbr.2011.1082
19. Ogawa K, Harata Y, Ichihara T, Kubo A, Hashimoto S. A practical method for position-dependent Compton-scatter correction in single photon emission CT. *IEEE Trans Med Imaging*. 1991;10(3):408–12. doi: 10.1109/42.97591
20. Ljungberg M, Celler A, Konijnenberg MW, Eckerman KF, Dewaraja YK, Sjögreen-Gleisner K. MIRD pamphlet no. 26: Joint EANM/MIRD guidelines for quantitative

- $^{177}\text{Lu}$  SPECT applied for dosimetry of radiopharmaceutical therapy. *J Nucl Med.* 2016;57(1):151–62. doi: 10.2967/jnumed.115.159012
21. Erlandsson K, Buvat I, Pretorius PH, Thomas B a, Hutton BF. A review of partial volume correction techniques for emission tomography and their applications in neurology, cardiology and oncology. *Phys Med Biol.* 2012;57(21):R119–59. doi: 10.1088/0031-9155/57/21/r119
  22. Ritt P, Vija H, Hornegger J, Kuwert T. Absolute quantification in SPECT. *Eur J Nucl Med Mol Imaging.* 2011;38:69–77. doi: 10.1007/s00259-011-1770-8
  23. Zeintl J, Vija AH, Yahil A, Hornegger J, Kuwert T. Quantitative Accuracy of Clinical  $^{99\text{m}}\text{Tc}$  SPECT/CT Using Ordered-Subset Expectation Maximization with 3-Dimensional Resolution Recovery, Attenuation, and Scatter Correction. *J Nucl Med.* 2010;51(6):921–8. doi: 10.2967/jnumed.109.071571
  24. Willowson K, Bailey DL, Baldock C. Quantitative SPECT reconstruction using CT-derived corrections. *Phys Med Biol.* 2008 Jun 21;53(12):3099–112. doi: 10.1088/0031-9155/53/12/002
  25. Blankespoor SC, Xu X, Kaiki K, Brown JK, Tang HR, Cann CE. Attenuation correction of SPECT using X-ray CT on an emission-transmission CT system: myocardial perfusion assessment. *IEEE Trans Nucl Sci.* 1996;43(4):2263–74. doi: 10.1109/23.531891
  26. Edyvean S, Weston J. Gammex RMI CT Phantom. 2007. Available from: <https://doczz.net/doc/4394046/gammex-rmi-ct-phantom--438> [accessed 20/07/2020]
  27. Brown S, Bailey DL, Willowson K, Baldock C. Investigation of the relationship between linear attenuation coefficients and CT Hounsfield units using radionuclides for SPECT. *Appl Radiat Isot.* 2008;66(9):1206–1212. doi: 10.1016/j.apradiso.2008.01.002
  28. Zaidi H, Hasegawa B. Determination of the attenuation map in emission tomography. *J Nucl Med.* 2003 Feb;44(2):291–315. PMID: 12571222
  29. Kadrmas DJ, Frey EC, Karimi SS, Tsui BMW. Fast implementations of reconstruction-based scatter compensation in fully 3D SPECT image reconstruction.



- Phys Med Biol. 1998;43(4):857–73. doi: 10.1088/0031-9155/43/4/014
30. Frey EC, Tsui BMW. A new method for modeling the spatially-variant, object-dependent scatter response function in SPECT. In: 1996 IEEE Nuclear Science Symposium Conference Record. IEEE; 1996:1082–1086. doi: 10.1109/nssmic.1996.591559
  31. Chun SY, Fessler JA, Dewaraja YK. Correction for Collimator-Detector Response in SPECT Using Point Spread Function Template. IEEE Trans Med Imaging. 2013;32(2):295–305. doi: 10.1109/tmi.2012.2225441
  32. Hawman E, Vija AH, Daffach R, Ray M. Flash 3D TM Technology Optimizing SPECT Quality and Accuracy. 2014. Available from: [https://www.researchgate.net/publication/265064101\\_Flash\\_3D\\_TM\\_Technology\\_Optimizing\\_SPECT\\_Quality\\_and\\_Accuracy](https://www.researchgate.net/publication/265064101_Flash_3D_TM_Technology_Optimizing_SPECT_Quality_and_Accuracy) [accessed 06/02/2019]
  33. Zhao W, Esquinas PL, Hou X, Uribe CF, Gonzalez M, Beauregard J. Determination of gamma camera calibration factors for quantitation of therapeutic radioisotopes. EJNMMI Phys. 2018;5(8):16. doi: 10.1186/s40658-018-0208-9
  34. EURAMET. Metrology for Molecular radiotherapy. 2015:1–33. Available from: <https://www.euramet.org/research-innovation/search-research-projects/details/project/metrology-for-molecular-radiotherapy/>. [accessed 01/05/2020]
  35. Roth D, Gustafsson J, Sundlöv A, Sjögreen Gleisner K. A method for tumor dosimetry based on hybrid planar-SPECT/CT images and semiautomatic segmentation. Med Phys. 2018;45(11):5004–18. doi: 10.1002/mp.13178
  36. Tagesson M, Ljungberg M, Strand SE. A Monte Carlo program converting activity distributions to absorbed dose distributions in a radionuclide treatment planning system. Acta Oncol (Madr). 1996;35(3):367–72. doi: 10.3109/02841869609101653
  37. Loevinger R, Budinger TF, Thomas F, Watson EE. Medical Internal Radiation Dose Committee. MIRD primer for absorbed dose calculations. Society of Nuclear Medicine; 1991;128. Available from: [https://books.google.co.za/books/about/MIRD\\_Primer\\_for\\_Absorbed\\_Dose\\_Calculatio.html?id=CGk5AAAACAAJ&redir\\_esc=y](https://books.google.co.za/books/about/MIRD_Primer_for_Absorbed_Dose_Calculatio.html?id=CGk5AAAACAAJ&redir_esc=y) [accessed 30/01/2020]

38. MIRDO. MIRDO Pamphlet #11: S, Absorbed dose per unit cumulative activity for selected radionuclides and organs. 1975;258. Available from: <http://snmmi.files.cms-plus.com/docs/hpra/MIRDO Pamphlet 11.pdf> [accessed 19/04/2020]
39. RADAR. The RADiation Dose Assessment Resource. 2019;0–3. Available from: [www.doseinfo-radar.com](http://www.doseinfo-radar.com) [accessed 22/07/2019]
40. Dewaraja YK, Wilderman SJ, Ljungberg M, Koral KF, Zasadny K, Kaminiski MS. Accurate dosimetry in <sup>131</sup>I radionuclide therapy using patient-specific, 3-dimensional methods for SPECT reconstruction and absorbed dose calculation. *J Nucl Med*. 2005;46(5):840–849. PMID: 15872359
41. Berker Y, Goedicke A, Kemerink GJ, Aach T, Schweizer B. Activity quantification combining conjugate-view planar scintigraphies and SPECT/CT data for patient-specific 3-D dosimetry in radionuclide therapy. *Eur J Nucl Med Mol Imaging*. 2011;38(12):2173–2185. doi: 10.1007/s00259-011-1889-7
42. Ljungberg M, Strand SE, King MA. Monte Carlo Calculations in Nuclear Medicine: Second Edition - Applications in Diagnostic Imaging. 2<sup>nd</sup> ed. Ljungberg M, Strand SE, King MA, editors. Taylor & Francis; 2012. 357.
43. Zaidi H. Relevance of accurate Monte Carlo modeling in nuclear medical imaging. *Med Phys*. 1999;26(February):574–608. doi: 10.1118/1.598559
44. Bahreyni Toossi M., Islamian P, Momennezhad M, Ljungberg M, Naseri S. SIMIND Monte Carlo simulation of a single photon emission CT. *J Med Phys*. 2010 1;35(1):42. doi: 10.4103/0971-6203.55967
45. Ljungberg M, Strand SE, King MA. The SIMIND Monte Carlo program. *Monte Carlo Calc Nucl Med Appl diagnostic imaging*. 1998;145–63.
46. Jan S, Benoit D, Becheva E, Carlier T, Cassol F, Descourt P. GATE V6 : a major enhancement of the GATE simulation platform enabling modelling of CT and radiotherapy. *Phys Med Biol*. 2011;56(4):881–901. doi: 10.1088/0031-9155/56/4/001
47. Sarrut D, Bardiès M, Bousson N, Freud N, Jan S, Létang J. A review of the use and potential of the GATE Monte Carlo simulation code for radiation therapy and dosimetry applications. *Med Phys*. 2014;41(6):064301-1–14. doi: 10.1118/1.4871617

48. Ljungberg M, Strand S. A Monte Carlo program for the simulation of scintillation camera characteristics. *Comput Methods Programs Biomed.* 1989 1;29(4):257–272. doi: 10.1016/0169-2607(89)90111-9
49. Ljungberg M, Strand S-E, King MA. *Monte Carlo Calculations in Nuclear Medicine: APPLICATIONS IN DIAGNOSTIC IMAGING.* CRC Press; 1998. 308.
50. Iturralde MP. *Dictionary and handbook of nuclear medicine and clinical imaging.* Taylor & Francis; 1990. 1–564.
51. Segars W, Tsui B, Cai J, Yin F, Fung G, Samei E. Application of the 4D XCAT phantoms in biomedical imaging and beyond. *IEEE Trans Med Imaging.* 2018;37(3):680–92. doi: 10.1109/tmi.2017.2738448
52. Sjögreen K, Ljungberg M, Wingårdh K, Minarik D, Strand S-E. The LundADose method for planar image activity quantification and absorbed-dose assessment in radionuclide therapy. *Cancer Biother Radiopharm.* 2005;20(1):92–97. doi: 10.1089/cbr.2005.20.92
53. Sundlöf A, Sjögreen-Gleisner K, Svensson J, Ljungberg M, Olsson T, Bernhardt P. Individualised <sup>177</sup>Lu-DOTATATE treatment of neuroendocrine tumours based on kidney dosimetry. *Eur J Nucl Med Mol Imaging.* 2017;44(9):1480–1489. doi: 10.1007/s00259-017-3678-4
54. Grimes J. Patient-specific internal dose calculation techniques for clinical use in targeted radionuclide therapy. 2013. PhD Thesis. The University of British Columbia. Vancouver.
55. Gear J, Chiesa C, Lassmann M, Gabiña PM, Tran-gia J, Stokke C. EANM Dosimetry Committee series on standard operational procedures for internal dosimetry for <sup>131</sup>I mIBG treatment of neuroendocrine tumours. *Eur J Nucl Med Mol imaging Phys.* 2020;7:15. doi: 10.1186/s40658-020-0282-7
56. Gleisner KS, Spezi E, Solny P, Gabina PM, Cicone F, Stokke C. Variations in the practice of molecular radiotherapy and implementation of dosimetry : results from a European survey. *EJNMMI Phys.* 2017;4(28):20. doi: 10.1186/s40658-017-0193-4
57. Morphis M, Staden JA Van, Raan H, Ljungberg M. Modelling of energy-dependent

spectral resolution for SPECT Monte Carlo simulations using SIMIND. *Heliyon*. 2021;7:12. doi: 10.1016/j.heliyon.2021.e06097

58. Morphis M, Staden JA Van, du Raan H, Ljungberg M. Validation of a SIMIND Monte Carlo modelled gamma camera for Iodine-123 and Iodine-131 imaging. *Heliyon*. 2021;7:11. doi: 10.1016/j.heliyon.2021.e07196
59. Morphis M, van Staden JA, du Raan H, Ljungberg M. Evaluation of Iodine-123 and Iodine-131 SPECT Activity Quantification : A Monte Carlo Study. 2021. *EJNMMI Phys*. doi: 10.1186/s40658-021-00407-1

# Chapter 2: Paper I

## **Modelling of energy-dependent spectral resolution for SPECT Monte Carlo simulations using SIMIND.**

This paper includes work which has been published in *Heliyon*  
(<https://doi.org/10.1016/j.heliyon.2021.e06097>).

The front page of the article is shown in Appendix A.

# Table of Contents

2.1. Introduction .....	2.2
2.2. Materials and methods.....	2.4
2.2.1 Modelling of intrinsic energy resolution .....	2.6
2.2.2 Validation of the fitted energy resolution model.....	2.8
2.2.3 Comparison of the energy resolution models in a simulated voxel-based digital patient phantom .....	2.9
2.3. Results .....	2.10
2.3.1 Modelling of intrinsic energy resolution .....	2.10
2.3.2 Validation of the fitted energy resolution model.....	2.14
2.3.3 Comparison of the energy resolution models in a simulated voxel-based digital patient phantom .....	2.16
2.4. Discussion.....	2.18
2.4.1 Modelling of intrinsic energy resolution .....	2.18
2.4.2 Validation of the fitted energy resolution model.....	2.19
2.4.3 Comparison of the energy resolution models in a simulated voxel-based digital patient phantom .....	2.20
2.5. Conclusion.....	2.21
2.6. References .....	2.23

## 2.1. Introduction

Monte Carlo (MC) modelling techniques have been used extensively in the field of nuclear medicine (NM) over the past 50 years. These techniques are ideal in NM because of the stochastic nature of radiation emission, transport, and the detection process. Essential applications of MC modelling techniques in NM include evaluation of collimator and detector design, image reconstruction and scatter correction techniques, as well as internal dosimetry. MC techniques are also useful in studying phenomena that may be impractical, or impossible to measure, such as collimator septal penetration and scatter. Various MC simulation codes with application to NM imaging, such as Simulation of imaging nuclear detectors (SIMIND) (1), SimSET (2) and GATE (3), are available, illustrating the significance of MC simulations in NM.

The importance of patient-specific radiopharmaceutical therapy for cancer therapy has increased over the past decade (4-8). Thus, accurate image quantification has become increasingly important in NM. MC techniques have been used extensively to evaluate quantification procedures in NM imaging (9-12). When making use of MC simulation software, it is essential to ensure that the intrinsic characteristics of the imaging system are defined correctly. One such characteristic is the energy resolution, which is described as the system's ability to distinguish between two radiation energies with a small energy difference (13). Factors such as variations in the number of light scintillation photons generated in the crystal, the number of photoelectrons produced in the photocathode, as well as the multiplication factor of the photomultiplier tubes, all contribute to variations in the signal amplitude produced by the photomultiplier tube. For every keV of absorbed energy in a sodium iodide (NaI) crystal, approximately 38 light photons are emitted. This relates to a single light photon per approximately 30.0 eV of absorbed energy (14). Depending on the quantum efficiency of the photocathode,  $N$  number of photoelectrons are released from the photocathode, upon absorption of a light photon. For events where the crystal has absorbed the same amount of energy, the resultant photomultiplier tube signal amplitude will vary depending on the number of photoelectrons released. If we assume Poisson statistics (discrete probability distribution), the variations can be described by the standard deviation,  $\sqrt{N}$ . Ultimately, this results in an energy spectrum, which is not a narrow line, but a Gaussian-shaped response (continuous probability distribution), as shown in Figure 2.1. A system will thus be able to resolve two energies if they are separated by at least the value of the system's full width half

maximum (FWHM), which is the width of the distribution at half the maximum value of the Gaussian photopeak, for a given photon energy.

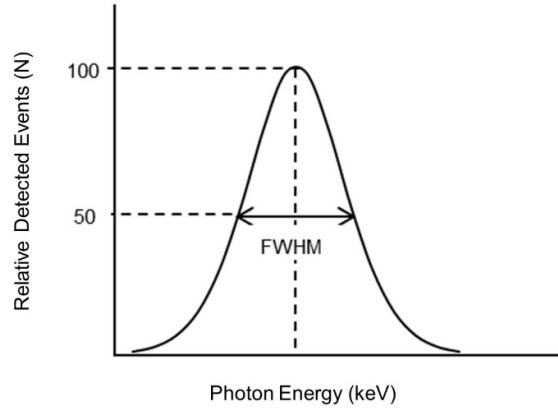


**Figure 2.1.** Definition of FWHM.

Considering the number of photoelectrons produced depends on the absorbed energy, ( $E$ ), one can assume the simple energy resolution relationship (14-15),

$$FWHM \propto 1/\sqrt{E} \quad (2.1)$$

It has been noted that this simplified relationship does not accurately predict the gamma camera detector response across all energies. When making use of the relationship above, the FWHM values at higher energies are underestimated (16-18). Any under- or overestimation of the energy resolution can ultimately affect the accuracy of the simulated image, which may lead to poor agreement between measured and simulated images. Inaccuracies could influence the quantification accuracy of scintillation images, which is vital in the process of performing internal dosimetry (18-19).

Hakimabad et al. (20) proposed a nonlinear response function (Equation 2.2) to model the energy resolution of a 3 x 3 in. NaI scintillation detector;

$$FWHM = a + b\sqrt{E} + cE^2 \quad (2.2)$$

with  $E$  the photon energy, and  $a$ ,  $b$  and  $c$  curve-fitting parameters. The use of this function to model the energy resolution of a gamma camera has not yet been reported in a scientific journal and was therefore evaluated in this study.

The study aimed to validate the accuracy of the proposed energy resolution model for the SIMIND MC code emulating the Siemens Symbia T16 dual-head gamma camera. This was



achieved by fitting the proposed energy resolution model to measured energy resolution values as a function of photon energy, ranging between 27.0 and 637.0 keV. The accuracy of this *fitted model* was then validated by comparing measured and simulated energy spectra obtained from in-air and in-scatter measurements. Finally, the energy spectra from radionuclides simulated in a voxel-based digital patient phantom were compared and evaluated.

## **2.2. Materials and methods**

A dual-head Siemens Symbia T16 (Siemens Healthcare, Erlangen, Germany) single-photon emission computed tomography/computed tomography (SPECT/CT) gamma camera is used for routine clinical studies at Universitas Academic Hospital (UAH), Bloemfontein, South Africa. The system is equipped with low energy high resolution (LEHR), medium energy low penetration (ME) and high energy (HE) collimators which were used for the respective extrinsic experimental measurements in this study. The Siemens Symbia T16 gamma camera was modelled using version 6.2 of the SIMIND MC code (1). The SIMIND MC code, written in FORTRAN-90, is a program, which simulates a standard clinical SPECT camera. With simple modifications, SIMIND can be used to perform a variety of calculations or measurements typically encountered in the field of NM.

When creating the virtual Siemens Symbia T16 system using the SIMIND MC code, all detector (crystal and collimator) characteristics were defined according to the Siemens Symbia T Series specification sheet (21). The thickness of the aluminium cover was set to 0.1 cm. SIMIND does not model the photomultiplier tubes nor any of the electronics; thus, a layer of backscatter material, mimicking the photomultiplier and electronic assembly, was simulated. This material has a density of  $1.47 \text{ g}\cdot\text{cm}^{-3}$  and consists of boron (4.0%), oxygen (54.0%), sodium (2.8%), aluminium (1.2%), silicon (37.7%) and potassium (0.3%). The thickness of backscatter material which mimicked the photomultiplier and electronic assembly of the physical gamma camera was set to 7.5 cm. The intrinsic spatial resolution of the physical gamma camera was obtained from acceptance test results and used as input into SIMIND. This ensured that the intrinsic characteristics of the virtual gamma camera were the same as that of the physical gamma camera.

The physical properties of the radionuclides used in this study and incorporated in SIMIND are shown in Table 2.1 (22). The minimum backscatter photon energy refers to the energy of the photon, originating from the backscattering medium (photomultiplier and electronic assembly), which has scattered at a  $180^\circ$  angle, before being absorbed in the crystal (14).

**Table 2.1**

**Characteristics of the radionuclides used in this study, including photopeak energies, abundances and minimum backscatter photon energies (22).**

Radionuclide	Photopeak energy (keV)	Abundance (%)	Minimum backscatter photon energy (keV)
Am-241 <sup>†</sup>	59.5 <sup>*</sup>	35.92	48.3
Ba-133	30.8 <sup>§</sup>	48.10	27.5
	35.5 <sup>§</sup>	11.34	31.2
	80.9 <sup>*</sup>	33.31	61.4
	356.0	62.05	148.7
	383.8	8.94	153.4
F-18	511.0 <sup>*</sup>	193.72	170.3
Ga-67 <sup>◇</sup>	93.3 <sup>*</sup>	38.10	68.3
	184.8 <sup>*</sup>	20.96	107.2
	300.2 <sup>*</sup>	16.60	138.0
	393.5	4.59	154.9
I-123 <sup>† ‡ ◇</sup>	27.3 <sup>§</sup>	35.34	24.7
	159.0 <sup>*</sup>	83.25	98.0
	528.9	1.28	172.3
I-131 <sup>† ‡ ◇</sup>	364.5 <sup>*</sup>	81.20	150.2
	636.9 <sup>*</sup>	7.12	182.3
	722.9	1.79	188.8
Lu-177 <sup>† ◇</sup>	55.2 <sup>§</sup>	2.19	45.4
	112.9 <sup>*</sup>	6.20	78.3
	208.4 <sup>*</sup>	10.38	114.8
Tc-99m <sup>† ‡</sup>	140.5 <sup>*</sup>	88.50	90.7

<sup>\*</sup> energy photopeaks included in the *fitted model*

<sup>†</sup> radionuclides considered for the extrinsic in-air energy spectra measurements and simulations

<sup>‡</sup> radionuclides considered for the extrinsic in-scatter energy spectra measurements and simulations

<sup>◇</sup> radionuclides considered for the voxel-based digital patient phantom simulations

<sup>§</sup> average energy and abundance for multiple emissions

## 2.2.1 Modelling of intrinsic energy resolution

### 2.2.1.1 Intrinsic energy spectra: measurements and modelling

Radioactive sources listed in Table 2.1 were positioned at 30.0 cm from one of the gamma camera detectors without a collimator and energy spectra were acquired from the source in air. Gamma camera acceptance tests showed little difference between the two detectors; thus, only a single detector was used in this study. The opposing detector was extended as far back as possible to minimise the contribution of backscatter from the second detector. The experimental setup is shown in Figure 2.2. Intrinsic energy spectra, with a digital resolution of 1.3 keV per channel, were acquired to obtain 30 000 counts in the channel with the highest count contribution. All intrinsic energy spectra acquisitions were repeated three times. The acquired energy spectra were exported from the manufacturer's computer and analysed using the public domain software, ImageJ (version 1.52r) (23). The main emission photopeaks were fitted with a Gaussian function, and the FWHM (keV) values were calculated for each photopeak. The measured intrinsic FWHM values (keV) were plot as a function of photon energy, and the curve fitting parameters of Equation 2.2 were determined using ImageJ.

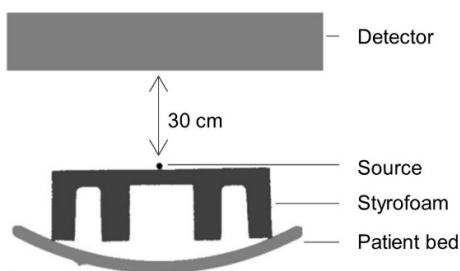


**Figure 2.2.** Experimental setup for measurement of in-air intrinsic energy spectra.

Computed tomography (CT) images were acquired of the setup, for use in the simulation. The CT acquisition was carried out in a  $512 \times 512$  image matrix with a pixel size of  $0.127 \times 0.127$  cm<sup>2</sup> and a slice thickness of 0.5 cm.

### 2.2.1.2 Intrinsic energy spectra: Monte Carlo simulations

SIMIND allows for three methods to incorporate energy resolution, based on (i) a *theoretical model* defined by Equation 2.1, normalised to Tc-99m, (ii) a predetermined fixed FWHM value for a specific photon energy, or (iii) a *fitted model* estimated from measured data, defined by Equation 2.2. When making use of method (i) and (ii), SIMIND requires the measured FWHM

value of Tc-99m, and that of the relevant photon energy, respectively. Method (iii) requires the user to specify the fitting parameters of the function (Equation 2.2) used to model the energy resolution. In this study, energy resolution estimation methods (i) and (iii) were utilised. Neither of these two methods require the user to determine the gamma camera energy resolution for the radionuclide of interest.

The CT images acquired with the CT of the physical gamma camera were segmented using ITK-SNAP version 3.6.0 (24). The segmented images were used to create a voxel-based digital phantom, as described by Ramonaheng et al. (25). This ensured that the setup for the simulation was identical to that of the measurement. Each segmented region was assigned a unique value, as shown in Figure 2.3. This value, together with the radioactivity concentration to be simulated, was defined in a text file. The CT images were converted from Hounsfield units to density values using an in-house software program developed in Visual Basic. The software program incorporates a bi-linear conversion model, which is based on measurements acquired with the Gammex RMI-465 phantom (26-27). The density images, along with the segmented images and text file, served as input for the SIMIND MC code.



**Figure 2.3.** Transverse slice of the segmented CT image of the source, Styrofoam block and patient bed.

Intrinsic energy spectra were simulated for each of the radionuclides listed in Table 2.1 using both the *theoretical* and the *fitted models*. The stop condition for each simulation was set equal to the duration of the energy spectra acquisitions on the physical gamma camera. A high number of histories (> 1 billion) were simulated for each energy spectrum. The FWHM was calculated for each main emission photopeak, in the same manner as for the measured energy spectra.

All MC simulations were performed on the computer cluster of the High-Performance Computing unit situated at the University of the Free States. The cluster has 36 computer nodes which perform calculations with 5560 CPU cores and 13.8 terabytes of system memory. The

simulations in this study made use of 2 of the 36 computer nodes, with 100 CPU cores per node.

## 2.2.2 Validation of the fitted energy resolution model

To validate the *fitted model*, a series of extrinsic (detector fitted with an appropriate collimator) energy spectra were acquired on the Siemens Symbia T16 gamma camera and also simulated. These energy spectra included in-air and in-scatter measurements and simulations for the radionuclides indicated in Table 2.1 (in-air (<sup>†</sup>) and in-scatter (<sup>‡</sup>)). All in-air acquisitions were repeated three times. However, due to long acquisition times and the lack of availability of the clinically used gamma camera, in-scatter acquisitions were only performed once.

### 2.2.2.1 Extrinsic energy spectra: measurements

A series of in-air extrinsic energy spectra were acquired on the physical gamma camera for Am-241, I-123 and Tc-99m using the LEHR collimator, I-123 and Lu-177 with the ME collimator and I-131 using the HE collimator, at a distance of 30.0 cm from the detector. The experimental setup is shown in Figure 2.4a. Additionally, in-scatter extrinsic energy spectra were acquired for Tc-99m and I-123 using the LEHR collimator, I-123 with the ME collimator and I-131 using the HE collimator. Similar to the in-air measurements, the individual sources were positioned 30.0 cm from the detector, with an added 15.0 cm of Perspex®, as shown in Figure 2.4b. The spectra were processed in the same manner as for the intrinsic energy spectra, and FWHM values were calculated for each main emission photopeak as listed in Table 2.1 (in-air (<sup>†</sup>)). The in-scatter energy spectra were visually evaluated. As before, CT images were acquired of each experimental setup for use in the simulation procedure.

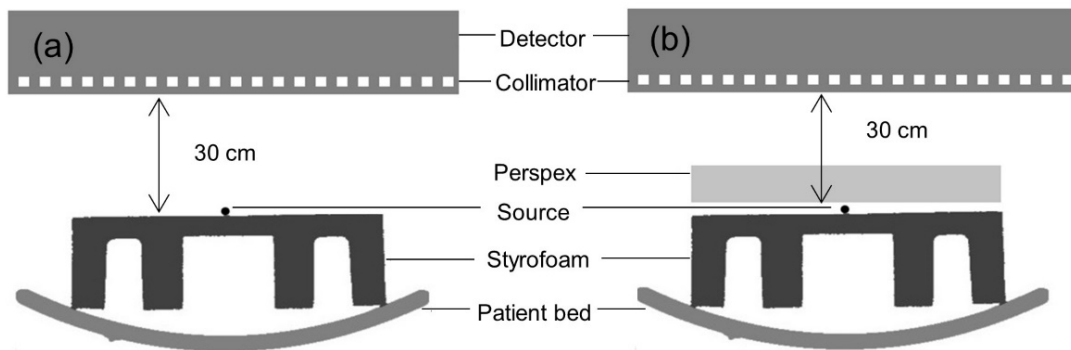


**Figure 2.4.** Experimental setup for measurement of extrinsic (a) in-air and (b) in-scatter.

### 2.2.2.2 Extrinsic energy spectra: Monte Carlo simulations

In-air and in-scatter extrinsic energy spectra were simulated, with the appropriate collimators, for radionuclides as listed in Table 2.1 (in-air (<sup>†</sup>) and in-scatter (<sup>‡</sup>)), using both the *theoretical* and *fitted models*. The stop condition and number of photons simulated per energy spectra were the same as that for the intrinsic energy spectra simulations. The FWHM values for the main photopeak's were calculated for the in-air extrinsic energy spectra.

The overall simulated and measured extrinsic energy spectra were visually evaluated and compared for both the in-air and in-scatter extrinsic energy spectra.

### 2.2.3 Comparison of the energy resolution models in a simulated voxel-based digital patient phantom

Energy spectra obtained from simulations of a voxel-based digital patient phantom, with both the *theoretical* and *fitted* energy resolution models, were compared. To create a voxel-based digital patient phantom, CT image data of a patient study carried out in UAH, was randomly and anonymously selected retrospectively from the Symbia T16 patient database. The voxel-based digital patient phantom was created as described before (Section 2.2.1.2). Three different sized spheres (0.5 cm, 3.0 cm and 5.0 cm diameters), mimicking spherical tumours, were digitally added to the thorax of the voxel-based digital patient phantom (Figure 2.5). Radionuclides typically used in targeted radionuclide treatment procedures as well as radionuclides with multiple photopeak's (listed in Table 2.1(<sup>◇</sup>)) were considered.



**Figure 2.5.** Schematic showing the position of the three spherical tumours in the patient phantom.

I-123, Lu-177, Ga-67 and I-131 radioactivity concentrations were assigned respectively to the tumours, lungs, liver and soft tissue of the patient phantom (tumour to background ratio of 100:1, tumour to liver ratio of 100:7.5 and tumour to lung ratio of 100:3.3). The radioactivity concentration values were based on clinical SPECT patient data. Anterior whole-body images were simulated for, I-123 with the LEHR collimator, I-123 and Lu-177 with the ME collimator, and I-131 with the HE collimator. Energy spectra generated from the simulated data, with both the *theoretical* and *fitted* energy resolution models, were visually evaluated.

### 2.3. Results

#### 2.3.1 Modelling of intrinsic energy resolution

The measured intrinsic energy resolution expressed as FWHM (keV) for photopeak's listed in Table 2.1 was plot as a function of energy in Figure 2.6. As a comparison, the *theoretical* and *fitted modelled* energy resolution values are also reported on the graph. The *fitted model* was determined as

$$FWHM = -0.534 + 0.946\sqrt{E} + 0.006E^2 \quad (2.3)$$

with an  $r^2$  value of 0.993.

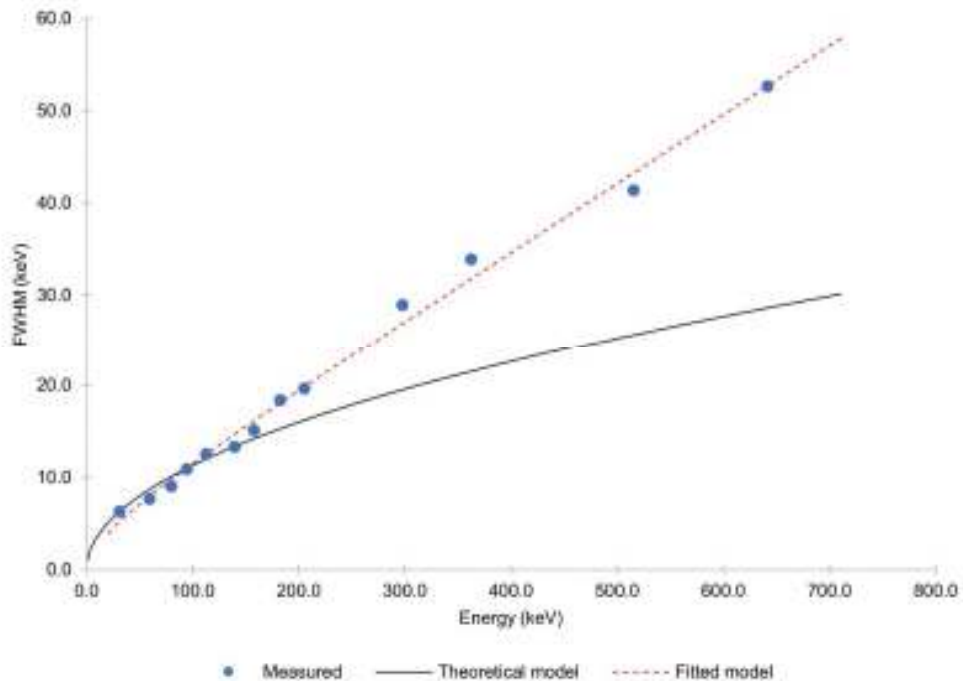


**Figure 2.6.** Comparison between the measured and simulated (*theoretical* and *fitted models*) intrinsic energy resolution.

It is important to note that all the radionuclides with multiple photon energies that could not be resolved by the gamma camera (i.e. Ba-133: 30.6, 30.9, 35.0 and 35.9 keV; Ba-133: 356.0 and 383.4 keV; I-123: 27.2, 27.4, 31.1 and 31.7 keV; Lu-177: 54.6 and 55.7 keV) were not considered in the model.

Table 2.2 shows the FWHM values obtained from the measured and simulated (using both the *theoretical* and *fitted models*) energy spectra for different photopeak's. FWHM differences between the simulated and measured results are reported for each of the radionuclides photopeak energies. FWHM average and standard deviation values for the three measurements of each photopeak energy are tabulated.

**Table 2.2**

**Intrinsic measured and simulated FWHM values and differences between measured and simulated data for each radionuclide at their photopeak energies.**

Radionuclide	Photopeak energy (keV)	Measured		Simulated			
				Theoretical model		Fitted model	
		FWHM (keV)		FWHM (keV)	Difference (keV)	FWHM (keV)	Difference (keV)
I-123	27.3	6.5	± 0.03	7.0	0.5	5.7	-0.8
Ba-133	30.8	6.4	± 0.01	7.4	1.0	6.0	-0.4
Lu-177	55.2	8.9	± 0.23	10.1	1.2	9.0	0.1
Am-241	59.5	7.3	± 0.04	9.0	1.7	8.2	0.9
Ba-133	80.9	9.1	± 0.09	10.6	1.5	10.3	1.2
Ga-67	93.3	10.9	± 0.04	11.3	0.4	11.3	0.4
Lu-177	112.9	12.5	± 0.19	12.7	0.2	13.2	0.7
Tc-99m	140.5	13.4	± 0.02	13.6	0.2	14.9	1.5
I-123	159.0	15.1	± 0.07	14.4	-0.7	16.4	1.3
Ga-67	184.8	18.4	± 0.22	15.9	-2.5	19.1	0.7
Lu-177	208.4	19.7	± 0.24	16.5	-3.2	20.2	0.5
Ga-67	300.2	29.0	± 0.16	19.8	-9.2	27.4	-1.6
Ba-133	356.0	36.4	± 0.27	22.0	-14.4	33.1	-3.3
I-131	364.5	33.9	± 0.06	21.8	-12.1	32.5	-1.4
F-18	511.0	41.4	± 0.14	25.8	-15.6	43.5	2.1
I-131	636.9	52.7	± 0.74	29.2	-23.5	53.8	1.1



According to Table 2.2, the largest standard deviation of the FWHM values calculated from the measured data was 0.74 keV for the 636.9 keV photopeak of I-131 (relative standard deviation of 1.5%). Note that the energy spectra were acquired with a digital resolution of 1.3 keV per channel; thus, the standard deviations obtained indicate that the inherent noise in the measurements was acceptable.

The measured and simulated intrinsic energy spectra, based on both the *theoretical* and *fitted models*, for each of the radionuclides listed in Table 2.2 are compared in Figure 2.7a to Figure 2.7h, respectively. All energy spectra were normalised and peaked to their respective main emission photopeaks for comparing the relative energy resolution of the spectra. The prominent photopeaks (P), backscatter peaks (B) and Compton edges (C) are indicated on the energy spectra.

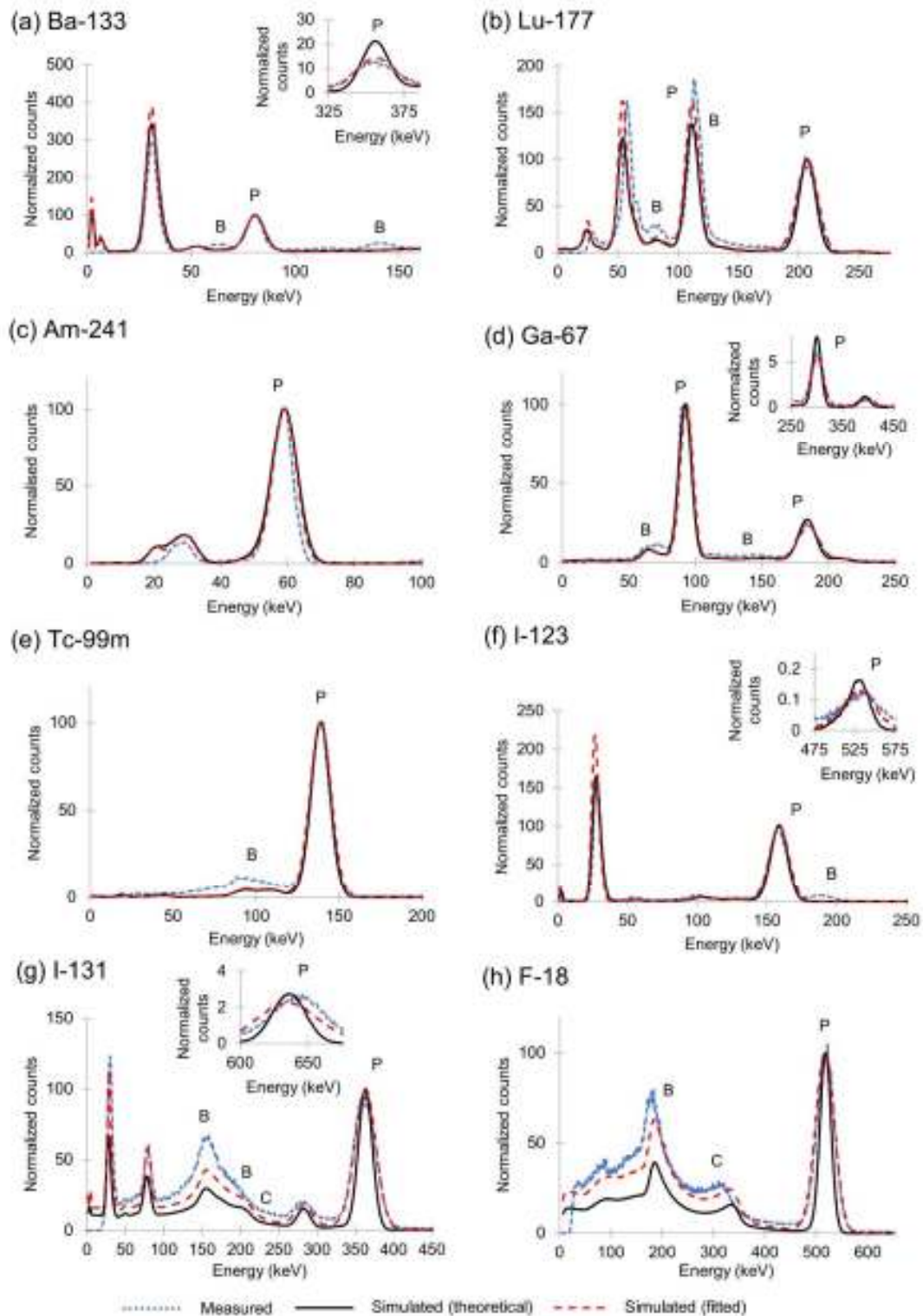


**Figure 2.7.** Comparison of the measured and simulated intrinsic energy spectra for the *theoretical* and *fitted models* for (a) Ba-133, (b) Lu-177, (c) Am-241, (d) Ga-67, (e) Tc-99m, (f) I-123, (g) I-131 and (h) F-18. The photon energy photopeak (P), backscatter peak (B) and Compton edge (C) are indicated on the energy spectra.

### 2.3.2 Validation of the fitted energy resolution model

Table 2.3 shows the calculated FWHM values and differences between the measured and simulated extrinsic in-air data for radionuclides listed in Table 2.1(†). As for the intrinsic measurements, average and standard deviation values for the three measurements of each photopeak energy are reported.

**Table 2.3**

**Extrinsic in-air FWHM values and differences between the measured and simulated data, for respective radionuclides photopeak energies with the highest abundance.**

Radionuclide	Photopeak energy (keV)	Measured FWHM (keV)	Simulated			
			Theoretical model		Fitted model	
			FWHM (keV)	Difference (keV)	FWHM (keV)	Difference (keV)
Lu-177 ME	55.2	8.7 ± 0.22	10.3	1.6	8.9	0.2
Am-241 LEHR	59.5	6.6 ± 0.01	9.0	2.4	8.3	1.7
Lu-177 ME	112.9	12.3 ± 0.18	12.9	0.6	13.5	1.2
Tc-99m LEHR	140.5	13.1 ± 0.03	13.6	0.5	14.9	1.8
I-123 LEHR	159.0	17.1 ± 0.05	17.4	0.3	20.2	3.1
I-123 ME	159.0	14.8 ± 0.04	14.8	0.0	16.6	1.8
Lu-177 ME	208.4	19.2 ± 0.11	16.6	-2.6	20.2	1.0
I-131 HE	364.5	38.6 ± 0.08	23.5	-15.1	36.5	-2.1

Figure 2.8 and Figure 2.9 show the extrinsic in-air and in-scatter energy spectra for radionuclides listed in Table 2.1 (in-air (†) and in-scatter (‡)). The standard deviation values reported in Table 2.3 for the average measured in-air extrinsic FWHM values indicate a small measurement error similar to the intrinsic measured data in Table 2.2.

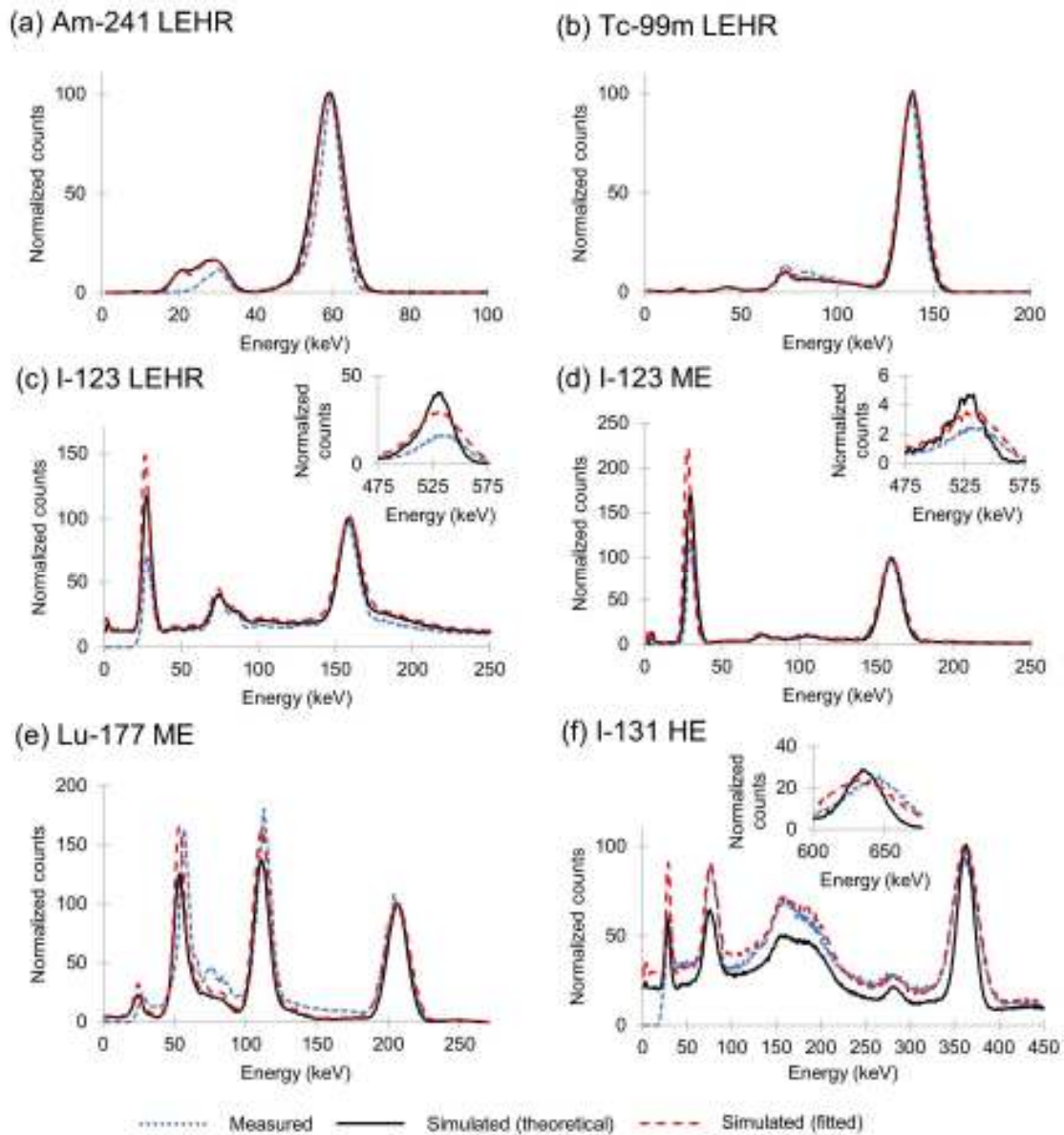


**Figure 2.8.** Comparison of the measured and simulated extrinsic in-air energy spectra for (a) Am-241 with the LEHR collimator, (b) Tc-99m with the LEHR collimator, (c) I-123 with the LEHR collimator, (d) I-123 with the ME collimator, (e) Lu-177 with the ME collimator and (f) I-131 with the HE collimator.

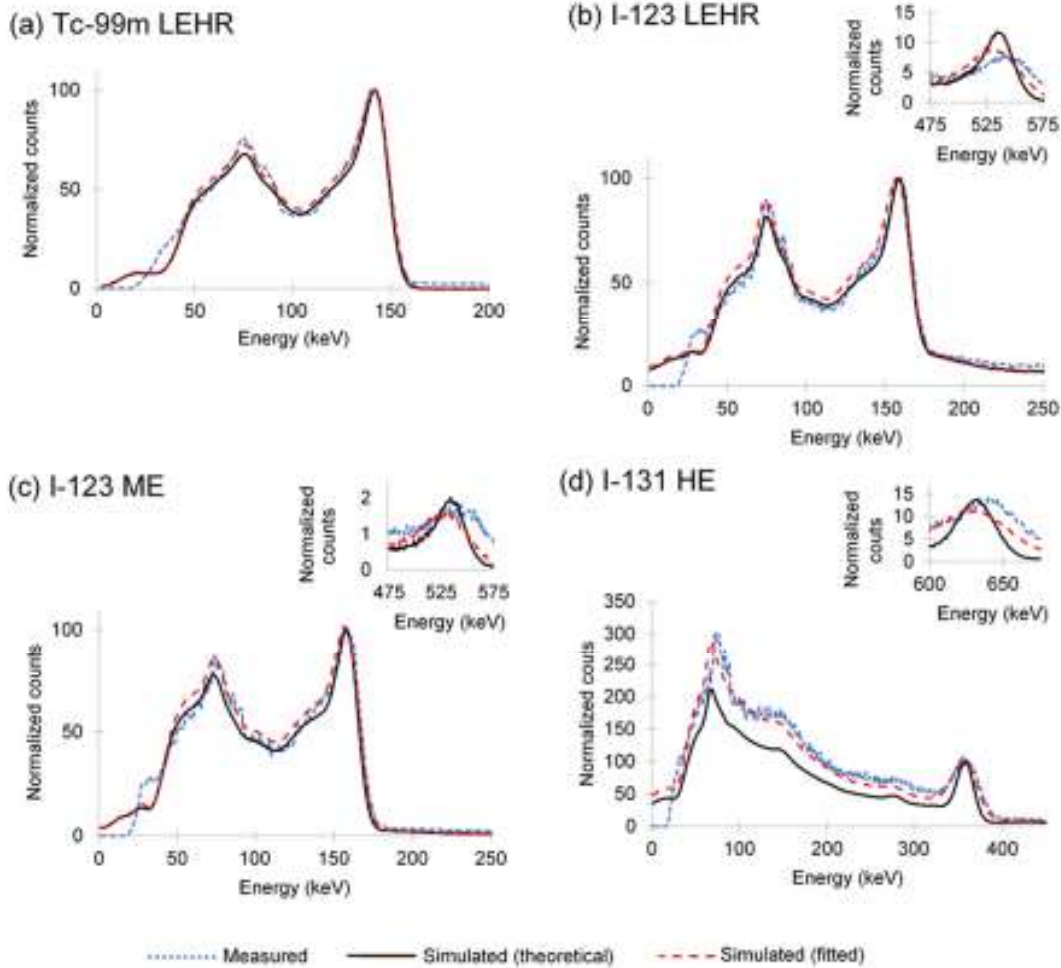


**Figure 2.9.** Comparison of the measured and simulated extrinsic in-scatter energy spectra with 15.0 cm scatter media for (a) Tc-99m with the LEHR collimator, (b) I-123 with the LEHR collimator, (c) I-123 with the ME collimator, and (d) I-131 with the HE collimator.

### 2.3.3 Comparison of the energy resolution models in a simulated voxel-based digital patient phantom

Figure 2.10 shows the simulated extrinsic energy spectra obtained with the voxel-based digital patient phantom for I-123 using both the LEHR and ME collimators, for Lu-177 and Ga-67 using the ME collimator and for I-131 with the HE collimator. These spectra were not normalised to their respective main emission photopeak's. The raw counts, obtained directly from the simulated image, are represented on the y-axis. The difference in sensitivity, as a result of the different energy resolution models, is clearly visible.

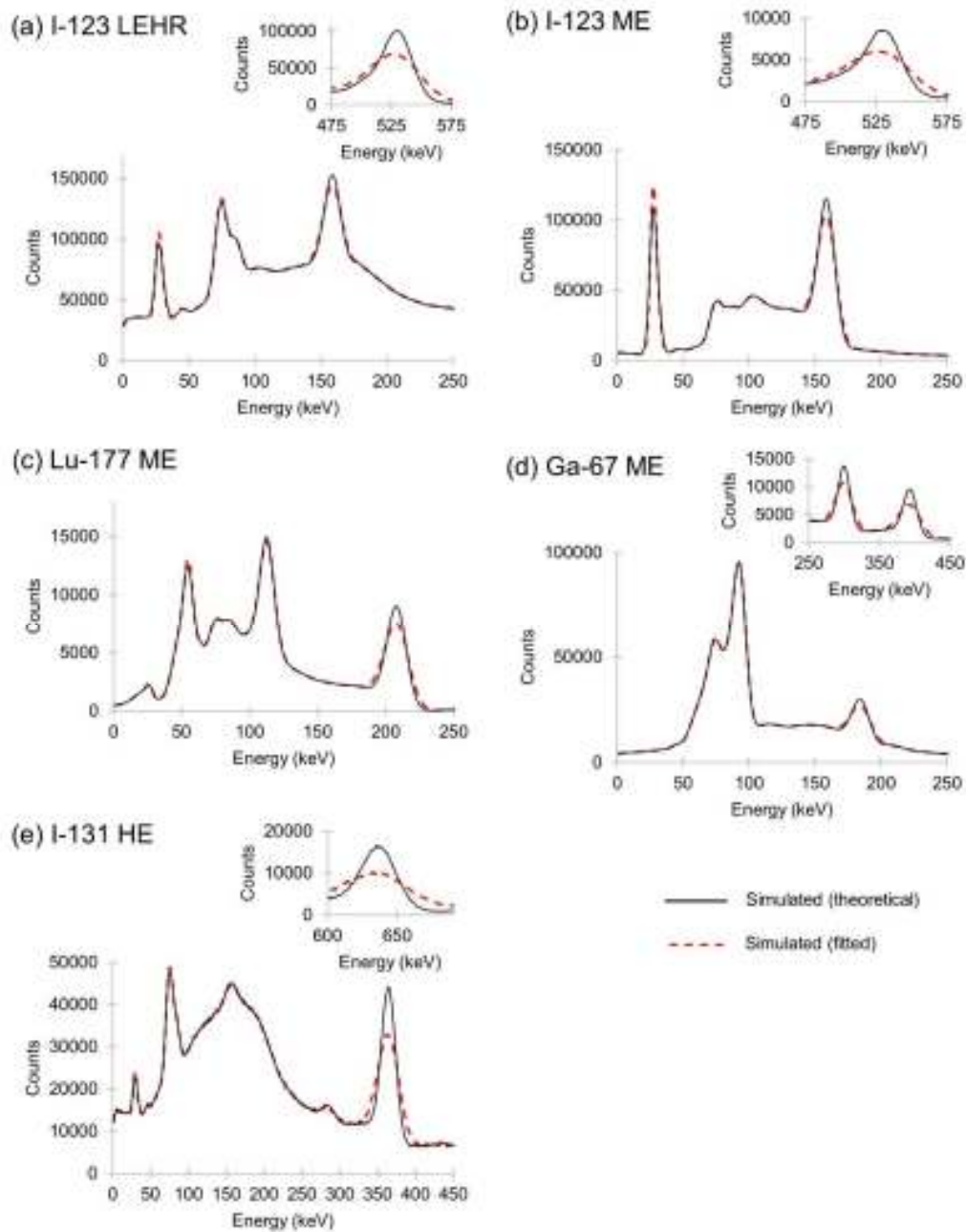


**Figure 2.10.** Comparison of the simulated extrinsic energy spectra obtained from the *theoretical* and *fitted models* of the patient phantom for (a) I-123 with the LEHR collimator, (b) I-123 with the ME collimator, (c) Lu-177 with the ME collimator, (d) Ga-67 with the ME collimator and (e) I-131 with the HE collimator.

## 2.4. Discussion

### 2.4.1 Modelling of intrinsic energy resolution

The measured and simulated FWHM values compare well at energies below 160.0 keV for simulations with both the *theoretical* and *fitted models* (Figure 2.6). For photon energies below 160.0 keV, the maximum absolute difference between the measured and simulated FWHM values using the *theoretical and fitted models* were 1.7 keV for Am-241 (59.5 keV) and 1.5 keV for Tc-99m (140.5 keV), respectively (Table 2.2). It is important to note that the simulations performed with the *theoretical model* made use of a predetermined intrinsic energy resolution value for Tc-99m, thus explaining the small difference (0.2 keV) between the measured and simulated intrinsic FWHM value. From Figure 2.6, it is evident that the *fitted model* accurately predicts the FWHM values above 160.0 keV, with a maximum absolute difference between the measured and simulated FWHM values of 3.3 keV for the 356.0 keV photopeak of Ba-133. In contrast, the *theoretical model* gradually underestimates the FWHM values as the photopeak energy increases above 160.0 keV, with a maximum difference of 23.5 keV for the 636.9 keV photopeak of I-131. This underestimation may lead to inaccurate radioactivity quantification when simulating NM images with high-energy photon emitting radionuclides (e.g. I-131), as well as radionuclides with multiple photopeak's (e.g. Lu-177, I-131 and Ga-67).

Energy spectra shown in Figure 2.7 are normalised and peaked to their respective main emission photopeak's allowing for easy comparison of energy resolution, however, this makes visual comparison of the measured and simulated energy spectra difficult. Notwithstanding this limitation, measured and simulated energy spectra, using the *fitted model*, show good agreement. It is important to note that the discrepancies noted on all the measured and simulated energy spectra at the low photon energies are due to the cut-off of photon energies at approximately 20.0 keV, respectively, for the Siemens Symbia gamma camera. Thus, photon energies below this are not reflected in any of the measured energy spectra. The cut-off of photon energies below 20.0 keV resulted in decreased amplitudes for the combined 30.8 keV and 35.5 keV photopeak for Ba-133 as well as for the 27.3 keV photopeak of I-123. The small offset between the measured and simulated photopeak's, visible on the spectra of Lu-177, F-18 and the high-energy I-123 and I-131 photopeak's is due to the nonlinear energy response of the detector to Compton and photoelectric events (14), which is not considered in the Monte Carlo simulation. This was also reported by Ramonaheng et al., for Lu-177 (25).

The difference noted between the measured and simulated energy spectra can be attributed to the addition of backscatter photons, originating from the second detector, which was included in the measurement, but not in the simulation. The simulated energy spectra only reflect backscatter originating from the detector components. Figure 2.7b shows the backscatter peak at 114.8 keV, originating from the 208.4 keV Lu-177 photopeak, which can't be distinguished from the 112.9 keV photopeak. This explains the difference between the amplitudes of the measured and simulated energy spectra at 112.9 keV.

The simulated energy spectra obtained with the *theoretical model*, however, show larger discrepancies when compared to the measured data. This is primarily due to the *theoretical model* not taking into account the variances of the photomultiplier tube gain and electronics as pointed out by Cherry et al. 14. Significant differences were visible, on Figure 2.7, at the higher energy photopeak's (Ba-133: 356.0 keV; Ga-67: 300.2 keV; I-123: 528.9 keV; I-131: 364.5 keV and 636.9 keV and F-18: 511.0 keV).

The small discrepancies visible in the Compton region for Lu-177 can be attributed to minor differences in the physical and simulated source geometries for this radionuclide. The large differences in the Compton regions for I-131 and F-18 measured and simulated with the *theoretical model*, is a result of incorrect modelling of the energy resolution at high energies. The limitations of the *theoretical model* were also reported by Rault et al. (17).

In general, Figure 2.7 shows that measured energy spectra at the higher energy range (> 160.0 keV) were better simulated using the *fitted model*.

#### **2.4.2 Validation of the fitted energy resolution model**

From Table 2.3, it is evident that the *theoretical model* underestimates the FWHM values at high photon energies (Lu-177 and I-131), with the largest absolute difference of 15.1 keV for the 364.5 keV photopeak of I-131. The FWHM values obtained with the *fitted model* is in better agreement with the measured data for Lu-177 (208.4 keV) and I-131 (364.5 keV). The largest discrepancy obtained between the FWHM values of the measured and simulated energy spectra, using the *fitted model*, was 3.1 keV.

The effect of septal penetration for I-123 with the LEHR collimator is evident, as the extrinsic in-air FWHM value at 159.0 keV (Table 2.3) is larger than that of the intrinsic FWHM value (Table 2.2). I-123 with the ME collimator shows a good agreement between the intrinsic and



extrinsic FWHM values at 159.0 keV. This is because the effect of septal penetration is less when using the ME collimator. As with I-123 with the LEHR collimator, the effect of septal penetration is evident in the increase in the extrinsic FWHM of I-131 using the HE collimator, in comparison to the intrinsic FWHM.

Differences noted between the measured and simulated extrinsic energy spectra (Figure 2.8 and Figure 2.9) were similar to that of the intrinsic energy spectra (Figure 2.7). As mentioned previously, the discrepancy noted between the measured and simulated energy spectra at low photon energies is due to the photon energy cut-off at 20.0 keV. Backscatter peaks in the extrinsic in-air measured energy spectra (Figure 2.9) were less prominent than in the measured intrinsic energy spectra (Figure 2.7) due to collimation. Due to the energy spectra being normalised and peaked to their respective main emission photopeak's, small differences are noted between the measured and simulated high-energy photopeak's of I-123 and I-131 for both the in-air and in-scatter energy spectra. The measured energy spectra at these high-energy photopeak's were better simulated using the *fitted model*. As for the intrinsic energy spectra, the slight offset noted between measured and simulated photopeak's can be attributed to the nonlinear energy response of the detector.

Figure 2.8f and Figure 2.9d show an overall underestimation of the I-131 lower energy Compton regions when simulating with the *theoretical model*. This can be attributed to the normalisation of the energy spectrum at the 364.5 keV photopeak. The *fitted model* better emulates both the in-air and in-scatter measured I-131 energy spectra.

#### **2.4.3 Comparison of the energy resolution models in a simulated voxel-based digital patient phantom**

Figure 2.10a and Figure 2.10b show minor differences between the energy spectra simulated with the *theoretical* and *fitted* energy resolution models for I-123 with both the LEHR and the ME collimator. However, the amplitude of the 159.0 keV photopeak obtained using the *theoretical model* exceeds that of the *fitted model*. This may lead to a difference in image quality and quantification. Figure 2.10c to Figure 2.10e shows a large discrepancy between the simulated high-energy photopeak's of Lu-177, Ga-67 and I-131. Differences are also noted in the scatter regions below and above the 208.4 keV Lu-177 photopeak, the 184.8 keV, 300.2 keV and 393.5 keV Ga-67 photopeak's and the 364.5 keV I-131 photopeak. If image quantification includes energy window-based scatter correction, inaccurate quantification may

result due to these differences. These differences are more pronounced with increasing photopeak energy, as expected. It is important to note the difference at the high-energy photopeak's for I-123 (528.9 keV) and I-131 (636.9 keV). There is a strong drive to correct for collimator septal scatter and penetration as part of quantification procedures. Thus, incorrect simulation of these photons may result in inaccurate quantification compensation techniques.

## 2.5. Conclusion

The measured and simulated FWHM values compare well at energies below 160.0 keV for both simulations with the *theoretical* and *fitted models*. At energies above 160.0 keV, the *theoretical model* gradually underestimates the FWHM values as the photopeak energy increases, with differences up to 23.5 keV. In contrast, the *fitted model* accurately predicts the FWHM values, across all photopeak energies, with a maximum absolute difference of 3.3 keV. Intrinsic energy spectra simulated with the *fitted model* for Ba-133, Lu-177, Am-241, Ga-67, Tc-99m, I-123, I-131 and F-18 compared well to the measured energy spectra. Intrinsic energy spectra simulated with the *theoretical model* resulted in large discrepancies for I-131 and F-18 as well as for the high-energy photopeak's of Ba-133 and I-123.

Similar results were obtained for the extrinsic energy spectra as for the intrinsic data when simulated using the *theoretical model*, with FWHM differences up to 15.1 keV. Overall, the energy spectra simulated with the *fitted model* compared well with the measured energy spectra. The most notable difference between the simulated spectra using the *theoretical model* and the measured data was seen for the I-131 spectrum. Minor differences noted between measured and simulated energy spectra, in the Compton region, could be attributed to the normalisation at respective photopeak's.

When a scatter medium was introduced, both the *theoretical* and *fitted models* show good agreement to the measured energy spectra for I-123 with the LEHR and ME collimators. However, for I-131, the overall energy spectrum simulated with the *fitted model* better matched the measured energy spectrum. Both the I-123 and I-131 higher energy photopeak's (528.9 keV and 636.9 keV) simulated with the *fitted model*, resembled the measured photopeak's more accurately.

The energy spectra obtained from simulations in a clinical scenario were compared when using the *theoretical* and *fitted models* for I-123, Lu-177, Ga-67 and I-131. Differences observed were more pronounced as the photon energy increased. Image quantification may be affected

due to these differences. Accurate image quantification becomes increasingly important with the demand for patient-specific radiopharmaceutical therapy planning and dosimetry.

This study did not make provision for estimating the quantification error that may be introduced due to incorrect modelling of the energy resolution of the gamma camera. A follow-up study should be conducted that considers different patient geometries, with a complete quantification protocol, including scatter and attenuation correction of planar and SPECT images.

This study shows that modelling of the energy resolution across all energies is essential when simulating NM studies with high-energy photon emitting radionuclides (e.g. I-131), as well as radionuclides with multiple photopeak's (e.g. Lu-177, Ga-67 and I-131). The *fitted* energy resolution model proposed in this study showed that it was accurate, also under circumstances where scatter was introduced. The comparison between the *theoretical* and *fitted models* in the simulated clinical environment shows that possible errors can be introduced in the simulation if the energy resolution model is not selected with great care. These errors can affect the accuracy of radioactivity quantification, which is vital for dosimetry purposes in patient-specific radiopharmaceutical therapy.

Accurate modelling of the Siemens Symbia T16 dual-head gamma cameras' energy resolution with the *fitted model* will result in accurately simulated images for all radionuclides used in NM, using the SIMIND MC code. These simulated images can be used to optimise image processing software as well as radioactivity quantification and internal dosimetry.

## 2.6. References

1. Ljungberg M, Strand SE. A Monte Carlo program for the simulation of scintillation camera characteristics. *Comput Methods Programs Biomed*, 1989; 29(4):257–272. doi:10.1016/0169-2607(89)90111-9.
2. Harrison RL, Laymon CM, Vannoy SD, Lewellen TK. Validation of the SPECT features of a simulation system for emission tomography. *IEEE Nucl Sci Symp Conf Rec (Cat. No.01CH37310)*, San Diego, CA, USA, 2001; 3:1363–1365. doi:10.1109/NSSMIC.2001.1008590.
3. Jan S, Santin G, Strul D, Staelens S, Assié K, Autret D. GATE: a simulation toolkit for PET and SPECT. *Phys Med Biol*, 2004; 49(19):4543–4561. doi:10.1088/0031-9155/49/19/007.
4. Jimenez C, Erwin W, and Chasen B. Targeted Radionuclide Therapy for Patients with Metastatic Pheochromocytoma and Paraganglioma: From Low-Specific-Activity to High-Specific-Activity Iodine-131 Metaiodobenzylguanidine. *Cancers*, 2019; 11(7). doi:10.3390/cancers11071018.
5. Kelkar SS, and Reineke TM. Theranostics : Combining Imaging and Therapy. *Bioconj Chem*, 2011; 22:1879–1903. doi:10.1021/bc200151q.
6. Chalkia MT, Stefanoyiannis A, Chatziioannou S, Round WH, and Efstathopoulos EP. Patient-Specific Dosimetry in Peptide Receptor Radionuclide Therapy: A Clinical Review. *Australas Phys Eng Sci Med*, 2014; 38: 7–22. doi:10.1007/s13246-014-0312-7.
7. Sjögreen Gleisner K, and Ljungberg M. Patient-Specific Whole-Body Attenuation Correction Maps from a CT System for Conjugate-View-Based Activity Quantification: Method Development and Evaluation. *Cancer Biother Radiopharm*, 2012; 27 (10): 652–664. doi:10.1089/cbr.2011.1082.
8. Roth D, Gustafsson J, Sundlöv A, and Sjögreen Gleisner K. A Method for Tumor Dosimetry Based on Hybrid Planar-SPECT/CT Images and Semiautomatic Segmentation. *Med Phys* 45, 2018; (11): 5004–5018. doi:10.1002/mp.13178.

9. Ljungberg M, Celler A, Konijnenberg MW, Eckerman KF, Dewaraja YK, and Sjögren Gleisner K. MIRDO Pamphlet No. 26: Joint EANM/MIRDO Guidelines for Quantitative  $^{177}\text{Lu}$  SPECT Applied for Dosimetry of Radiopharmaceutical Therapy. *J Nucl Med*, 2016; 57 (1): 151–62. doi:10.2967/jnumed.115.159012.
10. Ljungberg M, and Strand SE. A Monte Carlo Program for the Simulation of Scintillation Camera Characteristics. *Comput Methods Programs Biomed*, 1989; 29 (4): 257–272. doi:10.1016/0169-2607(89)90111-9.
11. Sjögren K, Ljungberg M, and Strand SE. An Activity Quantification Method Based on Registration of CT and Whole-Body Scintillation Camera Images, with Application to I131. *J Nucl Med*, 2002; 43 (7): 972–982.
12. Dewaraja YK, Wilderman SJ, Ljungberg M, Koral KF, Zasadny K, and Kaminiski MS. Accurate Dosimetry in  $^{131}\text{I}$  Radionuclide Therapy Using Patient-Specific, 3-Dimensional Methods for SPECT Reconstruction and Absorbed Dose Calculation. *J Nucl Med*, 2005; 46 (5): 840–849.
13. Murphy PH. Acceptance testing and quality control of gamma cameras, including SPECT. *J Nucl Med*, 1987; 28(7):1221–1227.
14. Cherry SR, Sorenson J, Phelps M. *Physics in Nuclear Medicine*. 3<sup>rd</sup> ed. Philadelphia: Saunders Elsevier, 2003.
15. Knoll GF. *Radiation detection and measurement*. 3<sup>rd</sup> ed. New York: John Wiley & Sons, 2005.
16. Birks JB. *The theory and practice of scintillation counting*. International series of monographs on electronics and instrumentation. London: Pergamon Press. Elsevier, 1967.
17. Rault E, Staelens S, Van Hoken R, De Beenhouwer J, Vandenberghe S. Accurate Monte Carlo modelling of the back compartments of SPECT cameras. *Phys Med Biol*, 2011; 56(1):87–104. doi:10.1088/0031-9155/56/1/006
18. Ejuh J. Accuracy of iodine-131 activity quantification and dosimetry for three-dimensional patient-specific models [thesis]. Bloemfontein, South Africa: University of

the Free State, 2019.

19. Frey EC, Humm JL, Ljungberg M. Accuracy and precision of radioactivity quantification in nuclear medicine images. *Semin Nucl Med*, 2012; 42(3):208–218. doi:10.1053/j.semnuclmed.2011.11.003
20. Hakimabad HM, Panjeh H, Vejdani-Noghreiyani A. Nonlinear response function of a 3×3 in. NaI scintillation detector. *Asian J Exp Sci*, 2007; 21(2):233–237.
21. Siemens Healthcare. Symbia S and T System Specifications, 2010, [https://static.healthcare.siemens.com/siemens\\_hwem-hwem\\_sxa\\_websites-context-root/wcm/idc/groups/public/@us/@imaging/@molecular/documents/download/mda1/mdkw/~edisp/symbia-t-spec-sheet-2010-01977049.pdf](https://static.healthcare.siemens.com/siemens_hwem-hwem_sxa_websites-context-root/wcm/idc/groups/public/@us/@imaging/@molecular/documents/download/mda1/mdkw/~edisp/symbia-t-spec-sheet-2010-01977049.pdf), 1–12 [accessed 18 June 2020].
22. Kellett M, Arinc A, Browne E, Christé V, Galan M, Huang X. Laboratoire National Henri Becquerel, 2017, [http://www.lnhb.fr/ddep\\_wg/](http://www.lnhb.fr/ddep_wg/) [accessed 18 June 2020].
23. Ferreira T, Rasband W. ImageJ User Guide: IJ 1.46r, 2012, <https://imagej.nih.gov/ij/docs/guide> [accessed 18 June 2020].
24. Yushkevich PA, Piven J, Hazlett HC, Smith RG, Ho S, Gee JC. User-guided 3D active contour segmentation of anatomical structures: significantly improved efficiency and reliability. *Neuroimage*, 2006; 31(3):1116–1128. doi:10.1016/j.neuroimage.2006.01.015
25. Ramonaheng K, van Staden JA, du Raan H. Validation of a Monte Carlo modelled gamma camera for Lutetium-177 imaging. *Appl Radiat Isot*, 2020; 163:109200. doi:10.1016/j.apradiso.2020.109200
26. Blankespoor SC, Xu X, Kaiki K, Brown JK, Tang HR, Cann CE. Attenuation correction of SPECT using X-ray CT on an emission-transmission CT system: myocardial perfusion assessment. *IEEE Trans Nucl Sci*, 1996; 43:2263–2274.
27. Edyvean S, Weston J. Imaging performance assessment of CT scanners. Gammex RMI CT Phantom. User Guide. London: St. Georges Hospital, 2007; 438:428.

# Chapter 3: Paper II

## **Validation of a SIMIND Monte Carlo modelled gamma camera for Iodine-123 and Iodine-131 imaging**

This paper includes work which has been published in *Heliyon*  
(<https://doi.org/10.1016/j.heliyon.2021.e07196>).

The front page of the article is shown in Appendix B.

# Table of Contents

3.1	Introduction .....	3.2
3.2	Materials and methods.....	3.5
3.2.1	Measurements.....	3.5
3.2.2	Simulations.....	3.10
3.3	Results .....	3.11
3.3.1	Static planar validation tests.....	3.11
3.3.2	WB planar validation tests .....	3.17
3.3.3	SPECT validation tests.....	3.19
3.4	Discussion.....	3.20
3.5	Conclusion.....	3.23
3.6	References .....	3.25



### 3.1 Introduction

Due to the increased interest in theragnostics in Nuclear Medicine (NM), the importance of image quantification using iodine-131 (I-131) and iodine-123 (I-123) has been re-emphasised (1–3). I-131 is one of the earliest radionuclides used for radiopharmaceutical therapy. Since the 1940s, I-131 has been used to treat differentiated thyroid carcinoma, and is the radionuclide of choice for thyroid diseases (4). However, it has also gained popularity in the treatment of non-Hodgkin lymphomas and neuroendocrine tumours (NETs). I-131 emits a principal gamma photon of 364.5 keV (81.2% abundance), one with 284.3 keV (6.1% abundance) and two higher energy photons of 636.9 keV (7.1% abundance) and 722.9 keV (1.8% abundance). Despite the low abundance of these two high-energy photons, they are still of importance due to their ability to penetrate the gamma cameras' collimator septa. I-131 has a physical half-life of 8.04 days and emits beta particles with a maximum and mean energy of 606.0 keV and 192.0 keV, respectively (5). Iodine naturally accumulates in the thyroid; however, it can be attached to a pharmaceutical, allowing targeted imaging and therapy. I-131 labelled to a noradrenaline analogue, meta-iodobenzylguanidine (mIBG), is typically used to detect and treat NETs. It naturally accumulates in NETs as well as the lungs, liver, kidneys, spleen, bladder, bone marrow and salivary glands (6,7).

In contrast to I-131, which emits both gamma photons and beta particles, I-123 is a pure gamma photon emitter. It emits a principal gamma photon of 159.0 keV (83.2% abundance) and additionally at 27.3 keV (70.7% abundance) and 528.9 keV (1.3% abundance) and has a physical half-life of 13.2 hours. These characteristics make I-123 ideal for diagnostic imaging. Since the uptake pattern of I-123 and I-131 are similar in the body, I-123 can be used in a treatment planning process of I-131 radiopharmaceutical therapy. I-123 carries a reduced radiation burden compared to I-131 due to its shorter half-life and lack of beta particles, and higher quantities of I-123 can therefore be administered for diagnostic purposes. As with I-131-mIBG, I-123-mIBG naturally accumulates in NETs as well as the lungs, liver, kidneys, spleen, bladder, bone marrow and salivary glands.

Because of the accumulation of these radiopharmaceuticals in healthy normal tissue, accurate dose calculations should be performed prior to therapy to predict the radiation burden organs at risk may encounter. The accuracy of absorbed dose calculations depends on several factors such as tumour and organ size, but most importantly on the radiopharmaceuticals' biokinetics. Factors that influence the estimation of biokinetic data include, but are not limited to, image

modality and the radionuclide-collimator combination used. Biokinetic information can be estimated from static or whole-body (WB) planar two-dimensional (2D) images, or single-photon emission computed tomography (SPECT) three-dimensional (3D) images. The use of quantitative SPECT imaging at multiple time points is potentially quantitatively more accurate in comparison to those obtained from planar imaging, considering it is a 3D modality. However, SPECT imaging can be highly time-consuming due to longer acquisition times and the limited field of view which required more than one bed-position acquisition. A compromise is to use the hybrid WB planar-SPECT/CT dosimetry method, proposed by Ljungberg and Gleisner (8). This method uses a set of WB data at multiple time points, to obtain the shape of the time-activity curve for a specific organ, which is then scaled to a single SPECT quantitative data point obtained at a single time point. This method can be useful in the case of large patient throughputs, since results in dosimetry accuracies are comparable to that of multiple SPECT/computed tomography (CT) images but with the speed of planar imaging (9).

The radionuclide-collimator combination is another important factor to consider. Imaging I-131 with a high energy (HE) collimator is well established (10), but it is not clear as to whether I-123 imaging should be performed with a low energy high resolution (LEHR) collimator or a medium energy (ME) collimator. For quantitatively accurate images, the ME collimator is favoured, as it reduces the effect of collimator septal scatter and penetration, resulting in improved image contrast (11). However, the LEHR collimator can provide superior spatial resolution images, but only if appropriate scatter and collimator resolution corrections are applied (11,12).

Monte Carlo (MC) techniques have played a significant role in the NM discipline and have become a method of choice to optimise instrumentation and clinical protocols, enhance image correction techniques, and develop and implement patient-specific dosimetry (13). By MC simulations, researchers can investigate what influence a parameter has on a system's performance and study the effect that a parameter has, in a way that otherwise is difficult or even impossible to measure (14). The MC method has been applied extensively in the modelling of gamma cameras for radionuclides, including technetium-99m, I-131 and lutetium-177 (10,15,16). There are various MC simulation codes available for NM imaging, such as Simulation of imaging nuclear detectors (SIMIND), SimSET and GATE (14,17,19,20).

In this study, we have used the SIMIND MC code which models a standard clinical scintillation camera for both planar and SPECT acquisitions (20). SIMIND has been extensively used to

estimate the quantification accuracy of planar and SPECT imaging (14,21,22). The energy resolution (ER) was simulated based on a fitted model ( $ER = a + b\sqrt{Energy} + (c \times Energy^2)$ ) where  $a$ ,  $b$  and  $c$  are estimated from measured data), as described by Morphis et al. (23). This ER estimation method was used in this study since recent results reported a significant improvement in the modelling of ER of high-energy photon emitting radionuclides (e.g., I-131), as well as for radionuclides with multiple photopeaks (e.g., I-131, I-123 and lutetium-177).

It is essential to validate any MC codes' capability in modelling a specific clinical gamma camera for the radionuclides of interest prior to its use as a clinical simulator (24). The SIMIND program has been used to model gamma cameras for radionuclides, including technetium-99m, I-131 and lutetium-177 (15,25–27). However, to our knowledge, modelling of the Siemens Symbia T16 gamma camera with SIMIND using a fitted ER model for I-123 with both the LEHR and ME collimators and I-131 with the HE collimator has not been reported.

This study therefore aimed to validate the SIMIND modelling of a Siemens Symbia T16 SPECT/CT system for I-123 using the LEHR and ME collimators (referred to as I-123 LEHR and I-123 ME, respectively) and I-131 using the HE collimator (referred to as I-131 HE), by comparing gamma camera measurements with simulations. A successful validation can further facilitate a more extensive evaluation of static planar, WB planar and SPECT I-123 and I-131 activity quantification accuracy using simulations.

A WB planar scan measurement differs in principle from a static planar measurement in that it involves a continuous bed motion in an axial direction, with a pre-set scanning speed. Since motion of the bed during an ongoing acquisition may influence image quality the performance criterion for WB planar imaging was therefore validated in addition to static planar imaging.

### 3.2 Materials and methods

The dual-head Siemens Symbia T16 (Siemens Healthcare, Erlangen, Germany) SPECT gamma camera is a SPECT/CT system used at Universitas Academic Hospital (UAH), Bloemfontein, South Africa. A series of static planar, WB planar and SPECT validation tests were measured on the gamma camera. These validation tests were then simulated using version 6.2 of the SIMIND MC code. The planar validation tests included a comparison of measured and simulated extrinsic (with a collimator) energy pulse-height distributions (EPHDs), static and WB planar system sensitivity and system spatial resolution in air (in-air spatial resolution). Additionally, the static planar system spatial resolution was obtained in a scattering medium (in-scatter spatial resolution). These specific tests were chosen in accordance with literature reports for MC gamma camera validations (15,27,28).

The SPECT validation test compared the measured and simulated SPECT sensitivity values obtained using the simple geometry of a sphere of activity in a cylindrical water-filled phantom.

Where applicable, the percentage difference and the difference between measured and simulated values were reported.

$$\% \text{ Difference} = \frac{\text{simulated value} - \text{measured value}}{\text{measured value}} \times 100 \quad (3.1)$$

$$\text{Difference} = \text{simulated value} - \text{measured value} \quad (3.2)$$

All measurements and simulations were performed for (i) I-123 LEHR, (ii) I-123 ME, and (iii) I-131 HE. Photopeak data was obtained within a 15% energy window centred over the 159.0 keV and 364.5 keV photopeak's for I-123 and I-131, respectively.

#### 3.2.1 Measurements

All static and WB planar measurements were acquired with a single detector only, as the gamma camera acceptance tests showed little difference between the system's two detectors. The amount of radioactivity used was sufficiently low that the camera did not display any dead-time effects; thus, no dead-time correction was necessary. Before measurements, the detector was peaked relative to the 159.0 keV and 364.5 keV photopeak's for all I-123 and I-131 measurements, respectively. SPECT measurements were, however, conducted using both detectors to increase sensitivity for a given acquisition time.

I-123 and I-131 activities were measured using a Biodex Atomlab 500 dose calibrator (Biodex Medical Systems, New York, NY, USA). The accuracy of the dose calibrator for both I-123 and I-131 was traceable to a secondary standard through the National Metrology Institute of South Africa (NMISA) in Cape Town, South Africa.

CT images were acquired for each static planar, WB planar and SPECT validation test setup, for use in both the SIMIND simulation and in the reconstruction processes, as explained below. The CT images were acquired in a standard imaging protocol (image matrix:  $512 \times 512$ , pixel size:  $1.2 \times 1.2 \text{ mm}^2$ , slice thickness: 5.0 mm, reconstruction kernel: standard smoothing body kernel (B08s)).

### *3.2.1.1 Static planar validation tests*

The validation procedure for static planar imaging was performed according to guidelines stipulated in the National Electrical Manufacturers Association (NEMA) recommendations for gamma camera performance criteria (29).

#### *Energy pulse-height distributions*

Extrinsic EPHDs (spectrum showing the distribution of counts as a function of photon energy, acquired with a collimator) were acquired from small point-like I-123 and I-131 sources, positioned on a Styrofoam block at source-to-collimator distances (SCDs) of  $150 \pm 2 \text{ mm}$ ,  $300 \pm 2 \text{ mm}$ , and  $650 \pm 2 \text{ mm}$  (Figure 3.1a). The EPHDs were acquired from the respective sources in air to obtain 30 000 counts in the channel with the highest count contribution. The acquired EPHDs were exported from the manufacturer's computer and analysed using the public domain software, ImageJ (version 1.52r) (30). Each energy pulse-height distribution (EPHD) was corrected for background radiation. A Gaussian function was fitted to the main emission photopeak data points, and the full width at half maximum (FWHM) values were calculated and reported in keV for each photopeak.

#### *System sensitivity*

A petri-dish (internal diameter: 87 mm) was filled with a homogenous solution of 92.8 MBq of I-123, up to a depth of approximately 2 mm. The petri-dish was positioned on a Styrofoam block in the centre of the detector's field-of-view, at a source-to-collimator distance (SCD) of  $100 \pm 2 \text{ mm}$  (Figure 3.1b). A four-million-count static planar image was acquired in a  $256 \times 256$  image matrix with a pixel size of  $2.4 \times 2.4 \text{ mm}^2$ . A second petri-dish of 61.8 MBq of I-131 was filled in the same way, and the acquisition was repeated. The count rate in counts

per second (cps) in a region-of-interest (ROI) with dimensions equal to that of the detector's useful-field-of-view (UFOV) was calculated. The system sensitivity, for each radionuclide-collimator combination, was calculated as follows,

$$\text{Sensitivity (cps/MBq)} = \frac{\text{count rate (cps)}}{\text{decay corrected activity (MBq)}} \quad (3.3)$$

#### *In-air spatial resolution*

A pair of capillary tubes was filled with 24.0 MBq of I-123 each and placed on a Styrofoam block,  $100 \pm 2$  mm apart, at SCDs of  $50 \pm 2$  mm,  $100 \pm 2$  mm, and  $150 \pm 2$  mm (Figure 3.1c). Static planar images were acquired in a  $512 \times 512$  image matrix with a pixel size of  $1.2 \times 1.2$  mm<sup>2</sup> until at least 10 000 counts in the peak location of each line spread function (LSF) was reached. An additional pair of capillary tubes was filled with 24.0 MBq of I-131 each, and static planar images were acquired, as before, at the same three distances. Profiles representing line-spread functions (LSFs) for each capillary tube were obtained from the measured images. Each LSF profile was fit with a Gaussian function, and from this fit, the FWHM and full width at tenth maximum (FWTM) values were calculated and reported in mm.

#### *In-scatter spatial resolution*

Planar static images were acquired, as above, but the imaging setup differed in that a 50 mm slab of Perspex® was positioned on top of the capillary tubes to introduce scatter (Figure 3.1d). FWHM and FWTM values were calculated for all radionuclide-collimator combinations.

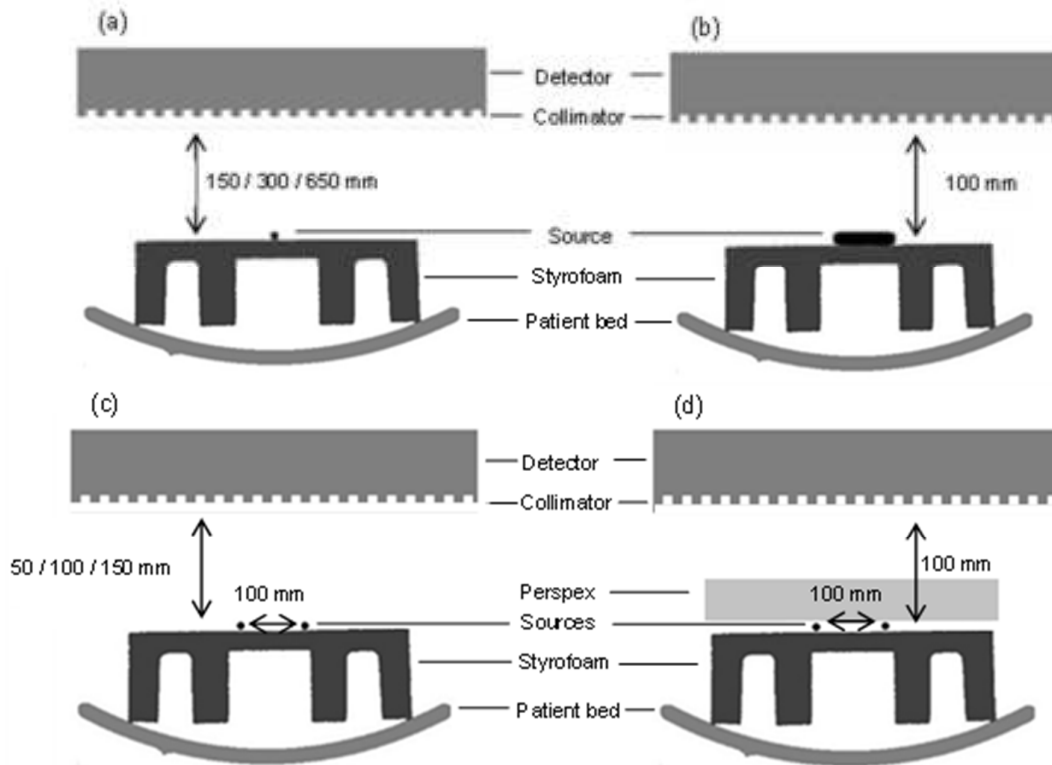


**Figure 3.1.** Gamma camera setup for the acquisition of (a) EPHD, (b) system sensitivity, (c) system in-air spatial resolution and (d) system in-scatter spatial resolution.

### 3.2.1.2 Whole-body planar validation tests

In this study, all WB planar images were acquired with the standard clinical imaging protocol (scan speed: 6.0 cm/min, image matrix size:  $256 \times 1024$ , pixel size:  $2.4 \times 2.4 \text{ mm}^2$ ). The sources were positioned at a SCD of  $100 \pm 2 \text{ mm}$ .

#### System sensitivity

Using the setup as shown in Figure 3.1b, WB planar system sensitivity images were acquired for all three radionuclide-collimator combinations. Similar to the static planar sensitivity, the WB system sensitivity was calculated using Equation 3.3 and counts obtained in a ROI, with dimensions equal to that of the detectors' useful field of view.

#### In-air spatial resolution

WB planar system spatial resolution images were acquired in both the X and Y orientations, using the setup, as shown in Figure 3.1c, for the three radionuclide-collimator combinations. Average FWHM and FWTM values were obtained and reported, as described for the static planar spatial resolution images.

### 3.2.1.3 SPECT validation test

A SPECT sensitivity value was obtained from a simple geometry of a Perspex sphere suspended in a water-filled cylindrical phantom (diameter: 216 mm, height: 186 mm), as shown in Figure 3.2. The sphere (diameter: 42 mm) was filled with 164.1 MBq and 86.9 MBq of I-123 and I-131, respectively. SPECT projection images were acquired using the standard clinical imaging protocol (step and shoot mode, non-circular orbit of rotation, 60 projections, 40 seconds per projection, matrix size:  $128 \times 128$ , pixel size:  $4.8 \times 4.8 \text{ mm}^2$ ). Images were acquired for all radionuclide-collimator combinations.

The SPECT projection images were reconstructed using an ordered subset-expectation maximisation (OS-EM) iterative reconstruction package, developed by Frey and Tsui (31), which is incorporated into software developed at Lund University, Sweden (32). The iterative reconstruction performs a CT-based attenuation correction, model-based scatter correction by the Effective Scatter Source Estimation (ESSE), and a collimator-detector response (CDR) correction, which includes septal penetration and scatter corrections, using precalculated MC simulated kernels. In this study, the SPECT images were reconstructed with six iterations and six subsets, into a  $128 \times 128 \times 128$  matrix with a voxel size of  $4.8 \times 4.8 \times 4.8 \text{ mm}^3$ .

Using the public domain software Amide (33), spherical volumes of interest (VOIs), corresponding to each sphere's physical size, were used to obtain the sphere counts (using fractional voxels which is the sum of voxel weights giving an indication of how large a region is in voxel space, instead of total voxels which are the total number of voxels both partial and total inclusion). Results were reported in units of cps/MBq for all three radionuclide-collimator combinations.

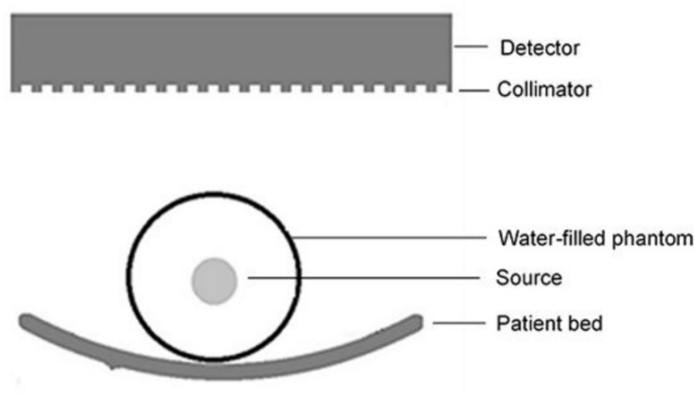


**Figure 3.2.** Gamma camera setup for the SPECT acquisition of sphere in a water-filled cylindrical phantom.



### 3.2.2 Simulations

The above-mentioned static planar, WB planar and SPECT validation test measurements were simulated using the SIMIND code. Voxel-based digital phantoms were created from the CT images obtained for each measurement setup to ensure the simulation setup was comparable. This process, together with the gamma camera's physical parameters (including intrinsic characteristics) and setup (including backscatter elements), as used in this study, has recently been described by Morphis et al. (23). It is important to note that the collimators were modelled with particle tracking, allowing for collimator septal scatter and penetration modelling.

The variation of the ER was modelled by a fitted ER function, ( $ER = a + b\sqrt{Energy} + (c \times Energy^2)$ ), proposed by Morphis et al. (23). The fitted model is estimated from measured data and was found to better model the gamma cameras' ER over the complete energy range when compared to the  $1/\sqrt{Energy}$  model that varies with an energy-dependent ER relative to a known value for a reference energy, as described in Cherry et al. (34).

Acquisition parameters (image matrix size, pixel size, energy window settings, activity values, acquisition time and radionuclide-collimator combinations) were kept the same as that used during the measurements, as described in Section 3.2.1.

#### 3.2.2.1 Static planar validation tests

Static planar images were simulated using the voxel-based digital phantoms created from each static planar validation acquisition setup. Image analysis was performed, as explained in Section 3.2.1.1 for the measured data.

As part of the simulation, SIMIND provides the percentage of penetrated photons after collimation. As this information was readily available, it was reported for the EPHDs.

#### 3.2.2.2 Whole-body planar validation tests

SIMIND does not mimic any motion of the patient bed (35). Thus, to simulate a WB scan, the detector's length was defined as the scan length (i.e., the length of the patient bed), in this case, 200.0 cm. The WB simulation time was calculated according to Equation 3.4, to ensure that the simulation mimics a measurement acquired at the specified patient bed scan speed.

$$WB \text{ simulation time (min)} = \frac{\text{length of physical detector (cm)}}{\text{scan speed (cm/min)}} \quad (3.4)$$

The WB simulation time equals 6.45 min, for a detector with length 38.7 cm and a scan speed of 6.0 cm/min. The voxel-based digital phantoms created for each planar validation test were used to simulate the WB planar images. The images were analysed as described in Section 3.2.1.2.

Considering that the WB planar simulation with SIMIND is a static process, the WB system spatial resolution was not repeated in a scatter medium, as it is assumed to be similar to static planar in-scatter spatial resolution.

#### *3.2.2.3 SPECT validation test*

The voxel-based digital phantom, of the sphere suspended in a water-filled cylindrical phantom was used to simulate SPECT data sets for the three radionuclide-collimator combinations. The SPECT projection images were reconstructed and analysed as for the measured data, described in Section 3.2.1.3.

### **3.3 Results**

#### **3.3.1 Static planar validation tests**

##### *Energy pulse-height distributions*

Figure 3.3 shows the measured and simulated extrinsic in-air EPHDs for all radionuclide-collimator combinations, at distances of 150 mm, 300 mm, and 650 mm, normalised to the respective main photopeak's of I-123 and I-131 (159.0 keV and 364.5 keV). It is important to note that the lower energy cut-off for the Siemens Symbia T16 gamma camera is at approximately 20.0 keV. Thus, photon energies below 20.0 keV are not reflected on any of the measured EPHDs.

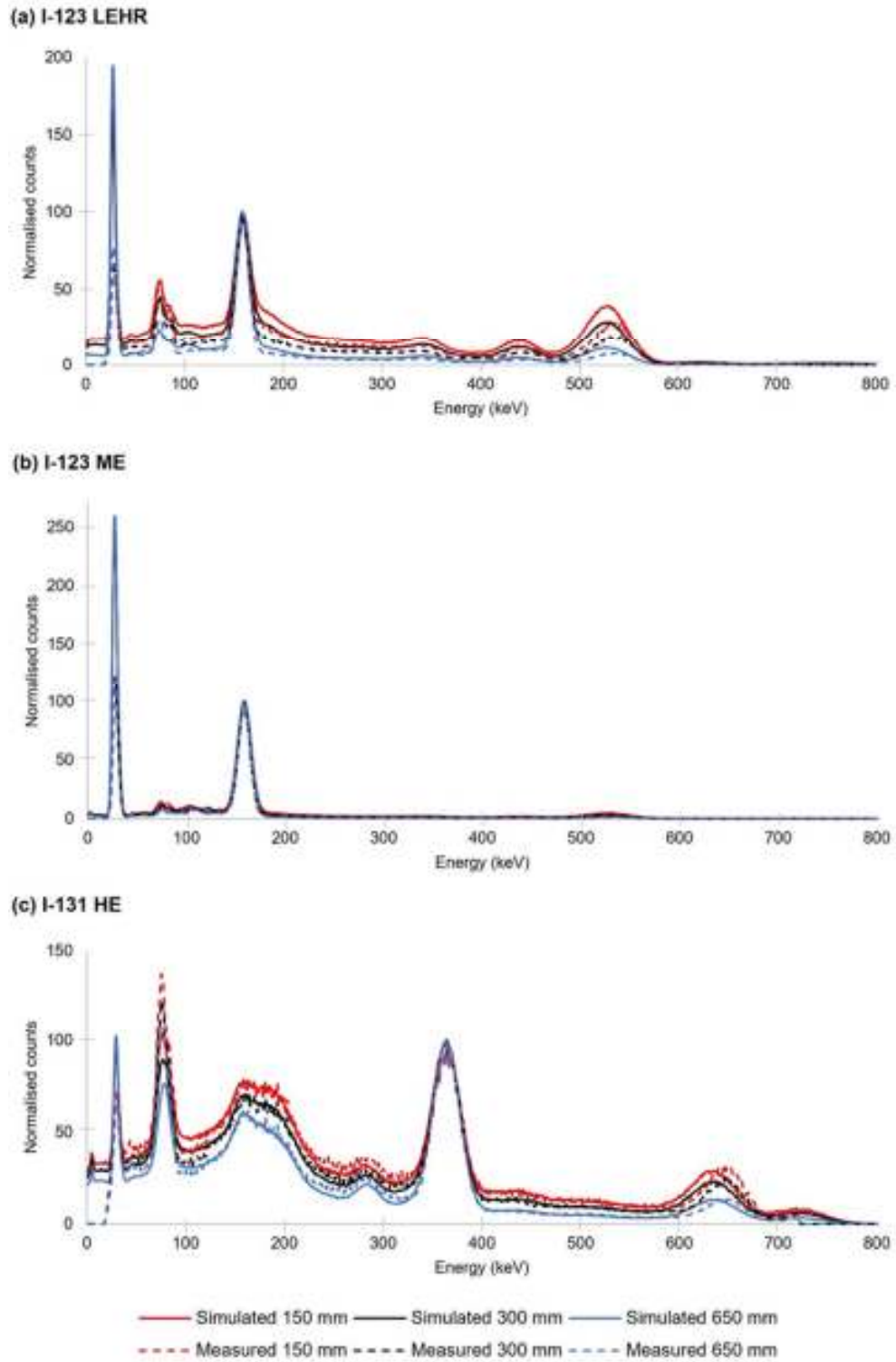


**Figure 3.3.** Comparison of the measured and simulated extrinsic EPDs of a small point-like source at SCDs of 150 mm, 300 mm, and 650 mm, for (a) I-123 LEHR, (b) I-123 ME and (c) I-131 HE.

The FWHM values obtained from the main photopeak's for the I-123 and I-131 EPHDs shown in Figure 3.3 are reported in Table 3.1. The differences between the measured and simulated main photopeak's are also shown for the three radionuclide-collimator combinations. Average and standard deviation values are reported for the measurements. Standard deviations not exceeding 0.3 keV were reported. The largest discrepancy between the measured and simulated FWHM values and percentage simulated penetration photons was 4.6 keV and 64.9%, respectively, for I-123 LEHR at a SCD of 150 mm.

**Table 3.1**

**Extrinsic in-air FWHM values and percentage simulated penetration photons for all isotope collimator combinations, at SCDs of 150 mm, 300 mm, and 650 mm.**

Radionuclide, collimator and photopeak energy (keV)	Distance (mm)	FWHM (keV)		Difference (keV)	*Simulated penetration photons (%)
		Measured	Simulated		
I-123 LEHR 159.0	150	18.1 ± 0.2	22.7	4.6	64.9
	300	16.7 ± 0.2	20.5	3.8	64.3
	650	15.4 ± 0.3	17.7	2.3	54.1
I-123 ME 159.0	150	14.9 ± 0.3	16.9	2.0	23.2
	300	14.7 ± 0.3	16.8	2.1	21.6
	650	14.6 ± 0.3	16.6	2.0	13.7
I-131 HE 364.5	150	39.0 ± 0.2	38.1	-0.9	34.3
	300	36.9 ± 0.2	36.5	-0.4	33.8
	650	34.7 ± 0.2	34.5	-0.2	31.8

\* Percentage simulated penetration photons after collimation

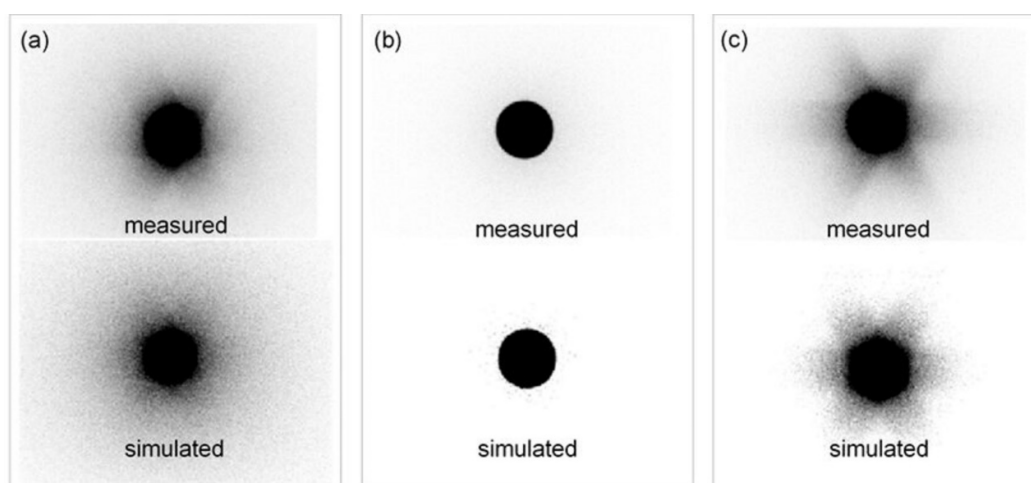
### System sensitivity

Table 3.2 shows measured and simulated static planar system sensitivity values for the three radionuclide-collimator combinations. The system sensitivity values compare well for all radionuclide-collimator combinations. I-123 LEHR displayed the largest differences of 12.7 cps/MBq, which relates to 6.9% difference, between measured and simulated sensitivity values.

**Table 3.2****Static planar system sensitivity values for I-123 LEHR, I-123 ME and I-131 HE.**

	Sensitivity (cps/MBq)		Difference (cps/MBq)	Percentage difference (%)
	Measured	Simulated		
I-123 LEHR	184.7 ± 0.09	172.0	12.7	-6.9
I-123 ME	121.6 ± 0.07	123.4	-1.8	1.5
I-131 HE	48.8 ± 0.02	48.8	0.0	0.0

Figure 3.4 shows that the measured and simulated petri-dish images compare well for all radionuclide-collimator combinations. The starlike pattern, typical of collimator septal penetration with a hexagonal-shaped collimator hole, is evident on both the measured and simulated images of I-123 LEHR and I-131 HE.



**Figure 3.4.** Measured and simulated static planar system sensitivity images, obtained from a petri-dish at a SCD of 100 mm, for (a) I-123 LEHR, (b) I-123 ME and (c) I-131 HE.

### *In-air spatial resolution*

The measured and simulated static planar system spatial resolution images and LSFs at a SCD of 100 mm, for the radionuclide-collimator combinations, are shown in Figure 3.5. The effects of septal penetration for I-123 LEHR and I-131 HE is visible in a raised tail region on the LSFs. Figure 3.6 shows the measured and simulated static planar system spatial resolution values (mm) in FWHM and FWTM, for all radionuclide-collimator combinations, at SCDs of 50, 100 and 150 mm. The error bars on the measured data represent two standard deviations. The measured and simulated FWHM and FWTM values compare well for all radionuclide-collimator combinations, with percentage differences not exceeding 6.4% and 10.0%, respectively.

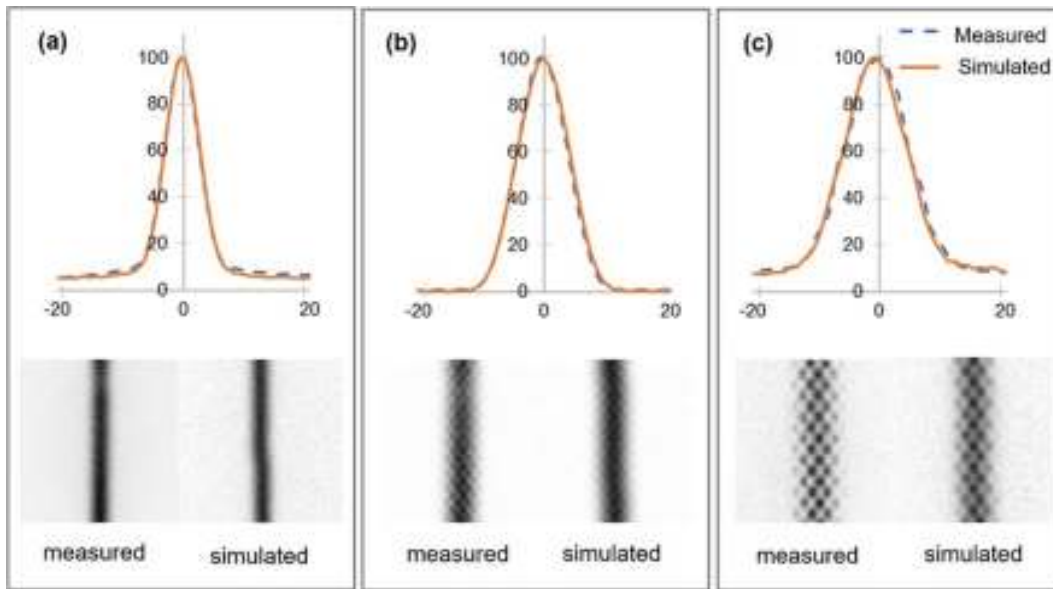


**Figure 3.5.** Measured and simulated LSFs and static planar system spatial resolution images of a capillary tube in air, at a SCD of 100 mm, for (a) I-123 LEHR, (b) I-123 ME and (c) I-131 HE.

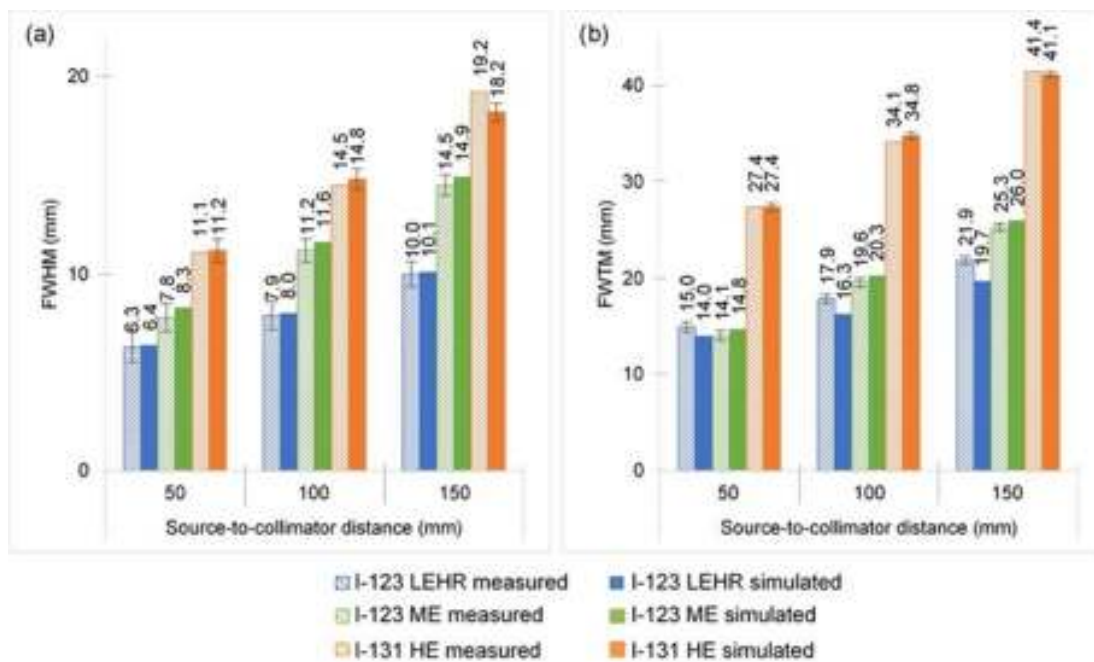


**Figure 3.6.** Measured and simulated static planar (a) FWHM and (b) FWTM values, obtained from capillary tubes in air, for SCDs of 50, 100 and 150 mm, for I-123 LEHR, I-123 ME and I-131 HE.

In-scatter spatial resolution

The measured and simulated static planar system spatial resolution images and LSFs with 50 mm of scatter medium for the three radionuclide-collimator combinations, for a SCD of 100 mm, are shown in Figure 3.7. The corresponding resolution values (mm) are shown in Figure 3.8.

A good agreement is noted between the measured and simulated FWHM and FWTM values, with percentage differences not exceeding 5.8% and 12.6%, respectively. The LSFs shown in Figure 3.7 also confirm this.

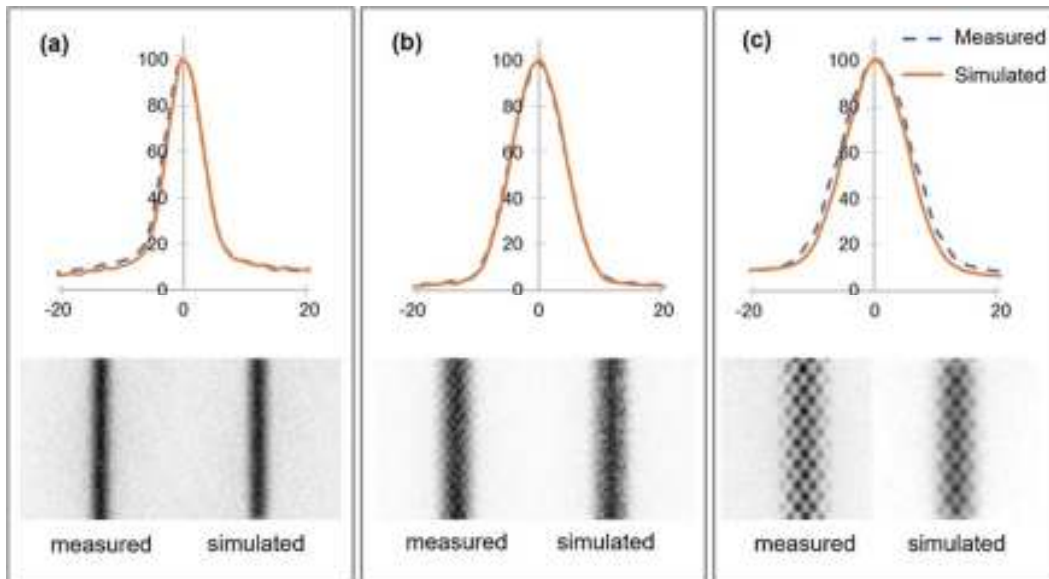


**Figure 3.7.** Measured and simulated LSFs and static planar system spatial resolution images with 50 mm of added scatter, at a SCD of 100 mm, for (a) I-123 LEHR, (b) I-123 ME and (c) I-131 HE.

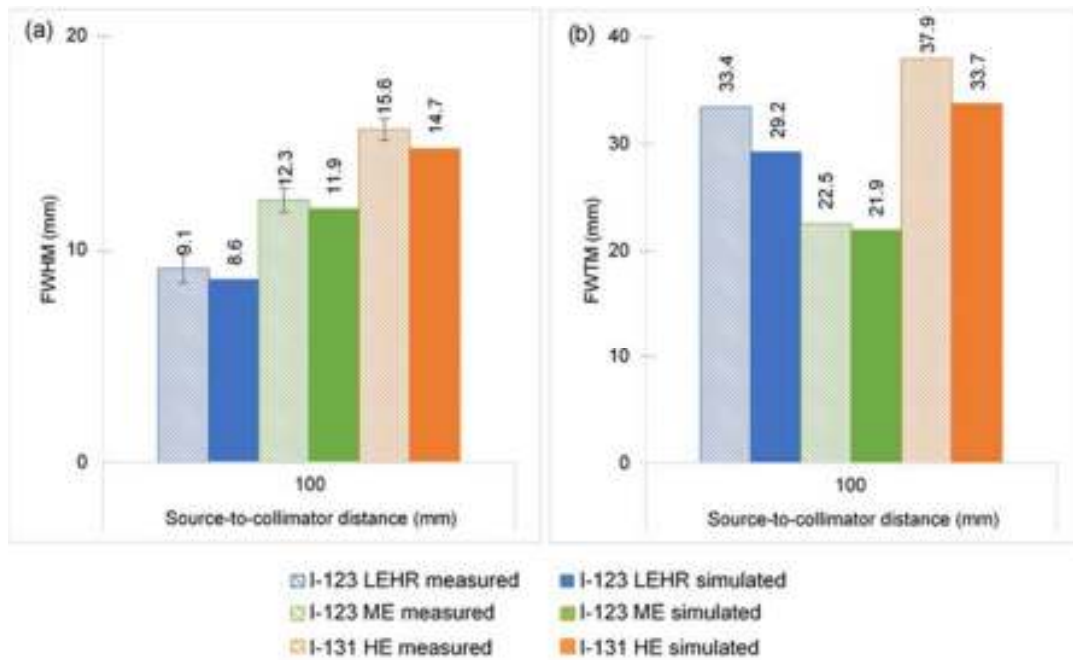


**Figure 3.8.** Measured and simulated static planar (a) FWHM and (b) FWTM values, with 50 mm of added scatter, for a SCD of 100 mm, for I-123 LEHR, I-123 ME and I-131 HE.

### 3.3.2 WB planar validation tests

#### *System sensitivity*

Table 3.3 shows measured and simulated WB planar system sensitivity values for the three radionuclide-collimator combinations. The measured and simulated WB planar system sensitivity values compare well. I-123 LEHR shows the largest deviation with a difference and percentage difference of 11.7 cps/MBq and 6.3%, respectively. The measured and simulated petri-dish images, shown in Figure 3.9, compare well.

**Table 3.3**

**WB planar system sensitivity values for I-123 LEHR, I-123 ME and I-131 HE.**

	Sensitivity (cps/MBq)		Difference (cps/MBq)	Percentage difference (%)
	Measured	Simulated		
I-123 LEHR	184.9 ± 0.89	173.2	11.7	-6.3
I-123 ME	120.4 ± 0.21	123.3	2.9	2.4
I-131 HE	48.3 ± 0.06	48.2	0.1	-0.2



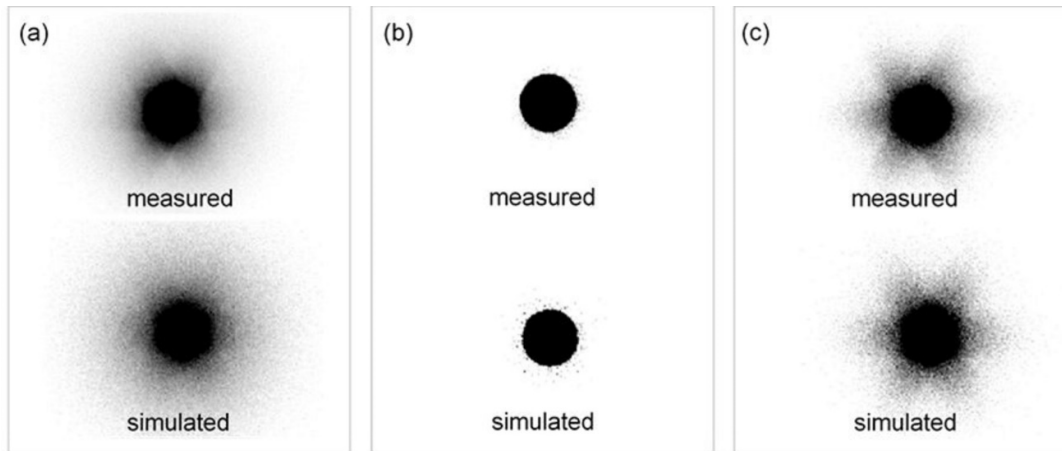


**Figure 3.9.** Measured and simulated WB planar system sensitivity images, obtained from a petri-dish at a SCD of 100 mm, for (a) I-123 LEHR, (b) I-123 ME and (c) I-131 HE.

*In-air spatial resolution*

Figure 3.10 shows the measured and simulated WB planar system spatial resolution images and LSFs, and Figure 3.11 the corresponding spatial resolution values (mm) in air for the three radionuclide-collimator combinations at a SCD of 100 mm. There are good agreements between the measured and simulated FWHM and FWTM values for all radionuclide-collimator combinations, and the percentage differences do not exceed 5.1% and 5.4%, respectively. The measured and simulated LSFs compare well for all radionuclide-collimator combinations.

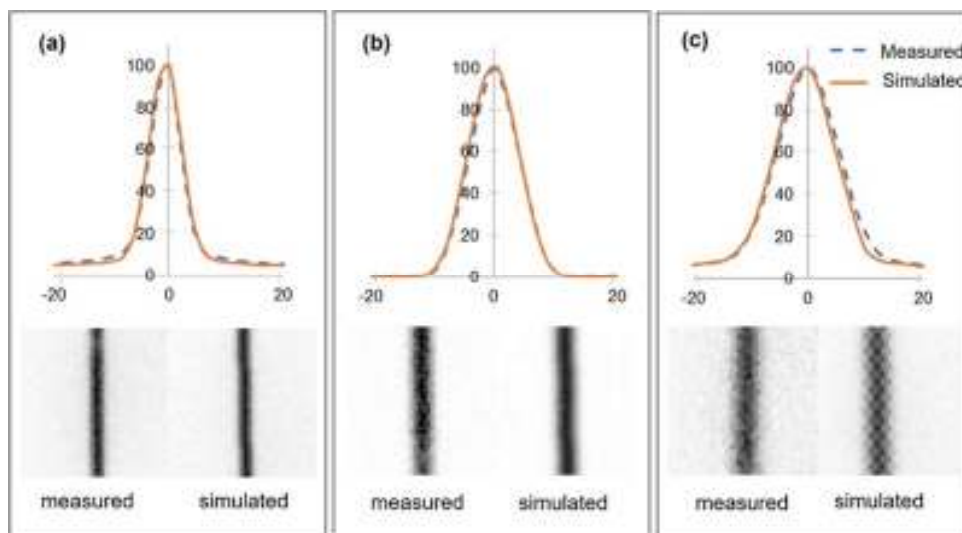


**Figure 3.10.** Measured and simulated LSFs and static WB system spatial resolution images of the capillary tubes in air, at a SCD of 100 mm, for (a) I-123 LEHR, (b) I-123 ME and (c) I-131 HE.

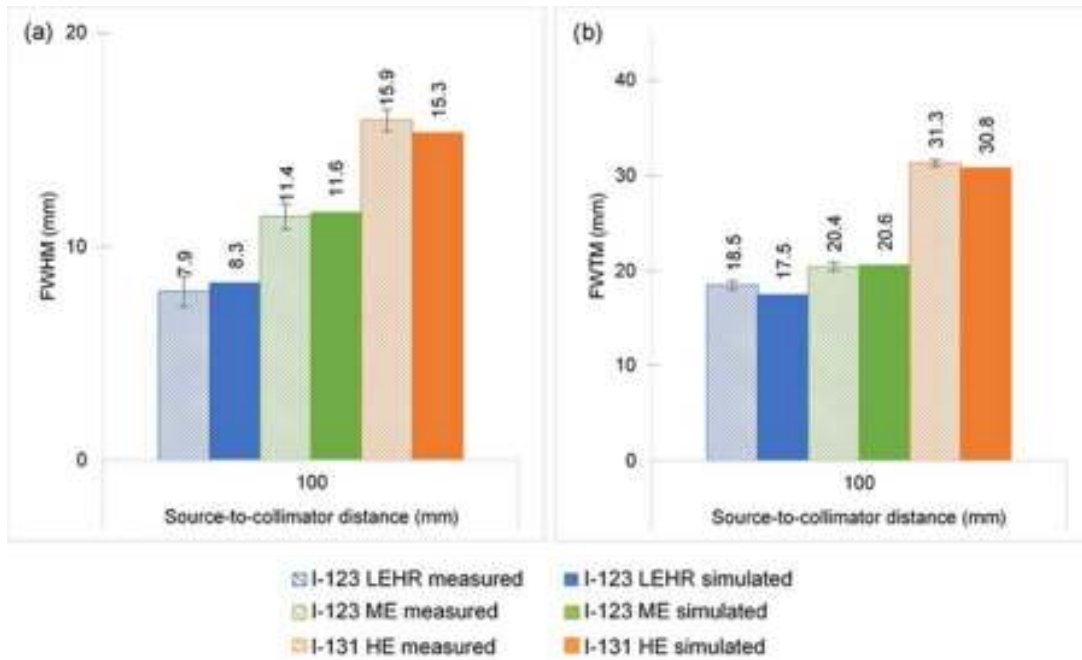


**Figure 3.11.** Measured and simulated WB planar (a) FWHM and (b) FWTM values obtained from the capillary tubes in air, at a SCD of 100 mm, for I-123 LEHR, I-123 ME, and I-131 HE.

### 3.3.3 SPECT validation tests

Measured and simulated SPECT sensitivity values for the three radionuclide-collimator combinations are shown in Table 3.4. The results show a good agreement for all radionuclide-collimator combinations, with differences and percentage differences not exceeding 2.5 cps/MBq and 3.6%, respectively. A transaxial slice through each of the reconstructed images is shown in Figure 3.12. Overall, the measured and simulated images compare well for all radionuclide-collimator combinations.

**Table 3.4**

**SPECT sensitivity values for I-123 LEHR, I-123 ME, and I-131 HE.**

	SPECT sensitivity (cps/MBq)		Difference (cps/MBq)	Percentage difference (%)
	Measured	Simulated		
I-123 LEHR	84.2 ± 0.11	83.4	0.8	-1.0
I-123 ME	121.4 ± 0.10	118.9	2.5	-2.0
I-131 HE	22.4 ± 0.21	21.6	0.8	-3.6

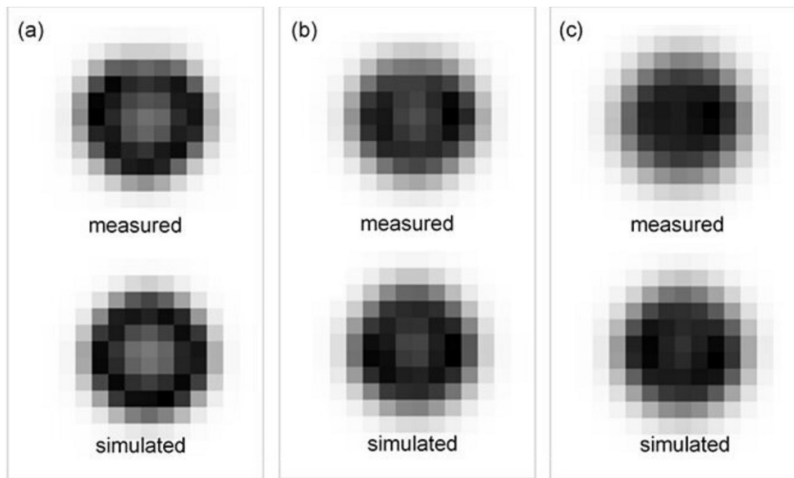


**Figure 3.12.** Transaxial slices through the reconstructed measured and simulated SPECT spheres in water for (a) I-123 LEHR, (b) I-123 ME and (c) I-131 HE.

### 3.4 Discussion

Overall, the results show a good agreement between the measured and simulated validation results for planar (static and WB) and SPECT imaging.

#### Energy pulse-height distributions

The underestimation in the modelling of the ER for low photon energies with the fitted ER model, as described by Morphis et al. (23), resulted in an increased amplitude of the 27.3 keV and the 29.6 keV photopeak's in the simulated EPHD of I-123 and I-131, respectively. This difference is further affected by the cut-off of photon energies below 20.0 keV. The small offset between the measured and simulated photopeak's, visible at the high-energy part of the I-123 and I-131 EPHD, is due to the nonlinear energy response of the physical gamma camera detector (34). The small differences seen between the amplitudes of the measured and simulated high-energy photopeak's of I-123 and I-131 can be attributed to the normalisation of the EPHDs to their respective main emission photopeak's. Similar measurement-simulation comparisons have been reported in literature (28,36); however, not necessarily using the SIMIND MC code.

Table 3.1 shows, as expected, a decrease in the percentage penetrated photons at increased SCD for all radionuclide-collimator combinations, which can also be seen in Figure 3.3. The effect of septal penetration is less pronounced for I-123 ME, as the percentage of photons penetrating the collimator septa is considerably less, thus, there is little difference between the

EPHDs and the calculated FWHM values at the three distances. The minor difference between the measured and simulated EPHD for I-123 LEHR (indicated by the arrows on Figure 3.3a) can be attributed to the backscattering of high-energy photons from the second detector at large angles up to 180°. The contribution of scattering of the high-energy photons from the second detector was not included in the simulation. Figure 3.3b shows that the septal scatter and penetration components of I-123 ME are negligible, and because of this, we see a good comparison between the measured and simulated EPHD. However, for I-123 LEHR and I-131 HE, the high-energy photons will substantially contribute to the number of counts detected in the photopeak area due to Compton scattering in the collimator and penetration through the collimator septa. This emphasises the need for accurate collimator modelling in the compensation methods when aiming for an accurate activity quantification of the radioactivity in situations where these radionuclide-collimator combinations are used.

#### System sensitivity

Accurate knowledge of the reference activity used to determine the system sensitivity value (static planar, WB planar and SPECT) is essential for quantitative imaging. The accuracy of the reference activity is dependent on the calibration of the dose calibrator for I-123 and I-131 which should be traceable to a secondary standards laboratory. During the calibration of the Biodex Atomlab 500 dose calibrator, performed by NMISA, it was found to underestimate the I-123 activity by 1.4% and overestimate the I-131 activity by 4.3%. From these results, correction factors were used when the I-123 and I-131 system sensitivity values were calculated.

The largest difference between the measured and simulated static planar and WB planar system sensitivity values were 6.9% (Table 3.2) and 6.3% (Table 3.3) for I-123 with the LEHR collimator, respectively. These discrepancies may also be attributed to scattered photons from the second detector, present in the measurement but not in the simulation. Discrepancies may also be attributed to small differences in source geometries used in this study and the geometries used by NMISA. A good agreement was found between the simulated static and WB planar sensitivity values (Table 3.2 and Table 3.3) for all three radionuclide-collimator combinations, with percentage differences not exceeding 1.2%. The measured and simulated static and WB planar images of the petri-dish source, as shown in Figure 3.4 and Figure 3.9, respectively, compare well and the starlike patterns, typical of collimator septal penetration,

are similar for the measured and simulated I-123 LEHR and I-131 HE images (10,25,37). Similar results have been reported in literature for I-131 planar system sensitivity (25,37).

The SPECT sensitivity results corroborate with values reported in literature (28,38). The differences noted between the SPECT sensitivity values (Table 3.4) and the planar and WB system sensitivity values (Tables 3.2 and 3.3) are as expected and show the effect of collimator septal scatter and penetration. I-123 LEHR and I-131 HE have large amounts of collimator septal scatter and penetration, which is corrected for in the SPECT reconstruction process, but not for planar imaging. I-123 ME has significantly less collimator septal scatter and penetration, thus the difference between the planar and SPECT sensitivity values is much less. Both the measured and simulated reconstructed images (Figure 3.12) show the so-called Gibbs artefacts, when incorporating the collimator response compensation in the reconstruction process. These artefacts are characterised by increased count levels located at the edges of an object and a corresponding lower count level in the centre (16). Small differences noted between measured and simulated SPECT sensitivity results may be attributed to the inconsistent VOI position across all scenarios, combined with the overestimated voxels at the sphere boundaries. Similar results have been reported in literature (27,39).

#### Spatial resolution

The measured and simulated FWHM values compare well for all radionuclide-collimator combinations, as shown in Figure 3.6 and Figure 3.11, for static and WB planar system spatial resolution in air, respectively. As expected, the spatial resolution deteriorates with increasing SCD (34). Both measured and simulated FWTM values for the static and WB planar images compare well for I-123 ME. Larger discrepancies are, however, noted for I-123 LEHR and I-131 HE, resulting in FWTM percentage differences of 10.0% and 5.4% for static and WB planar images, respectively.

Figure 3.5 reveals small discrepancies at the tail regions of I-123 LEHR LSF, which could explain the difference between the measured and simulated FWTM values, displayed in Figure 3.6. The measured and simulated LSFs for WB planar (Figure 3.10) compare well for all radionuclide-collimator combinations. However, minor discrepancies can be seen in the tail regions of the LSFs for I-123 LEHR and I-131 HE. This discrepancy correlates to the difference noted in the FWTM values reported in Figure 3.11.

The effect of the hexagonal pattern of holes, due to the construction of the collimator, can be seen on the static planar images obtained from I-123 ME and I-131 HE (Figure 3.5). Because of the necessity of large hole diameters and thicker septa, a lower spatial resolution can be expected (25,40). However, the pattern is less prominent on the WB planar measured I-123 ME and I-131 HE images (Figure 3.11). This may be attributed to the sources' movement relative to the detector during a WB planar acquisition – an effect that was not included in the static WB simulation.

When considering the system spatial resolution obtained from the in-air and in-scatter static planar images (Figure 3.6 and Figure 3.8), the FWHM values compare well. The increased values of the measured FWTM, shown in Figure 3.8, originates from photons that were scattered in the scatter medium with a lower resulting photon energy that was absorbed in the sodium iodide (NaI) crystal, and still fell within the 15.0% imaging energy window due to the ER. Additionally, photons that originate from Compton scatterings in the collimator of the second detector, have a probability of being included in the measurement; however, this effect is not simulated and thus, may also contribute to discrepancies in the FWTM values. It is important to note that when describing the spatial resolution in terms of FWTM, the result will be affected by events from potentially high-energy photon emissions, such as those that occur in the I-123 and I-131 decays. With the presence of septal scatter and penetration, the FWTM measurement can be problematic and is therefore often omitted (40). Similar to the in-air results, the small discrepancies between the measured and simulated FWTM values observed for I-123 LEHR and I-131 HE, are confirmed in the LSF tail regions, as shown in Figure 3.5 and Figure 3.7.

Overall, the results show a better spatial resolution for I-123 LEHR than for I-123 ME. Thus, when imaging with I-123, the LEHR collimator would be better suited for studies prioritising spatial resolution. I-131 HE results in poorer spatial resolution in comparison to I-123. Similar results have been reported in literature (11,12,25,40).

### **3.5 Conclusion**

Existing gamma camera models simulated with MC codes lack an accurate implementation of the gamma camera's energy response across all photon energies. Morphis et al. (23) addressed this deficiency by implementing a fitted function which models the Siemens Symbia T16 gamma camera's energy response across all energies and used it together with the SIMIND MC

code to improve the simulations with the gamma camera. In this study, we have validated this model by comparing results from physical measurements with the gamma camera to simulations with SIMIND using this improved fitted ER model for the radionuclide-collimator combinations: I-123 LEHR, I-123 ME, and I-131 HE.

Results show that when using I-123 and I-131 with the LEHR and HE collimator, respectively, appropriate collimator response corrections, including modelling of septal scatter and penetrations, are essential when accurate activity quantification is required. The use of a ME collimator for I-123 imaging reduces the effects of septal penetration and collimator scatter from the high-energy photons. The ME collimator is therefore a better choice when no septal scatter and penetration corrections are available.

Overall, this study has shown the SIMIND MC code's potential usefulness, combined with our improved ER model, to further develop activity quantification methods for I-123 and I-131 static planar, WB planar and SPECT acquisitions with the Siemens Symbia T16 gamma camera.

### 3.6 References

1. Sjögreen K, Ljungberg M, Strand S, Library PM. An activity quantification method based on registration of CT and whole-body scintillation camera images, with application to I131. *J Nucl Med.* 2002;43(7):972–982. doi: 10.11.580.371
2. Silberstein E. Radioiodine : The Classic Theranostic Agent. *Semin Nucl Med.* 2012;42(3):164–170. doi: 10.1053/j.semnuclmed.2011.12.002
3. Yordanova A, Eppard E, Kürpig S, Bundschuh R, Schönberger S, Gonzalez-carmona M. Theranostics in nuclear medicine practice. *Onco Targets Ther.* 2017;10:4821–4828. doi: 10.2147/ott.s140671
4. Thomas SR. Options for radionuclide therapy: from fixed activity to patient- specific treatment planning. *Cancer BiotherRadiopharm.* 2002;17(1084-9785 SB-IM):71–82. doi: 10.1089/10849780252824091
5. Kellett M, Arinc A, Bé M, Browne E, Chechev V, Chisté V. Laboratoire National Henri Becquerel. 2017. Available from: <http://www.lnhb.fr/en/>
6. Bombardieri E, Giammarile F, Aktolun C, Baum RP, Bischof Delaloye A, Maffioli L. <sup>131</sup>I/<sup>123</sup>I-Metaiodobenzylguanidine (mIBG) scintigraphy: Procedure guidelines for tumour imaging. *Eur J Nucl Med Mol Imaging.* 2010;37(12):2436–2446. doi: 10.1007/s00259-003-1357-0
7. Giammarile F, Chiti A, Lassmann M, Brans B, Flux G. EANM procedure guidelines for <sup>131</sup>I-meta-iodobenzylguanidine (131I-mIBG) therapy. *Eur J Nucl Med Mol Imaging.* 2008;35(5):1039–47. doi: 10.1007/s00259-008-0715-3
8. Ljungberg M, Gleisner K. Hybrid Imaging for Patient-Specific Dosimetry in Radionuclide Therapy. *Diagnostics.* 2015;5(3):296–317. doi: 10.3390/diagnostics5030296
9. Garkavij M, Nickel M, Sjogreen-Gleisner K, Ljungberg M, Ohlsson T, Wingardh K. Lu-177[ DOTA0 , Tyr3 ] Octreotate Therapy in Patients With Disseminated Neuroendocrine Tumors : Analysis of Dosimetry With Impact on Future Therapeutic Strategy. *Cancer.* 2010;116(4 Suppl):1084–1092. doi: 10.1002/cncr.24796



10. Dewaraja YK, Ljungberg M, Green AJ, Zanzonico PB, Frey EC. MIRD Pamphlet No. 24: Guidelines for Quantitative <sup>131</sup>I SPECT in Dosimetry Applications. *J Nucl Med.* 2013;54(12):2182–2189. doi: 10.2967/jnumed.113.122390
11. Rault E, Vandenberghe S, Holen R Van, Beenhouwer J De, Staelens S, Lemahieu I. Comparison of image quality of different iodine isotopes ( I-123 , I-124 , and I-131 ). *Cancer Biother Radiopharm.* 2007;22(3). doi: 10.1089/cbr.2006.323
12. Dobbeleir AA, Hambÿe AE, Franken PR. Influence of high-energy photons on the spectrum of iodine-123 with low- and medium-energy collimators : consequences for imaging with <sup>123</sup>I-labelled compounds in clinical practice. *Eur J Nucl Med.* 1999;26(6):655–658. doi: 10.1007/s002590050434
13. Ljungberg M, Strand SE, King MA. Monte Carlo Calculations in Nuclear Medicine: Second Edition - Applications in Diagnostic Imaging. 2<sup>nd</sup> ed. Ljungberg M, Strand S-E, King MA, editors. Taylor & Francis; 2012;357
14. Zaidi H. Relevance of accurate Monte Carlo modeling in nuclear medical imaging. *Med Phys.* 1999;26(February):574–608. doi: 10.1118/1.598559
15. Bahreyni Toossi M., Islamian P, Momennezhad M, Ljungberg M, Naseri S. SIMIND Monte Carlo simulation of a single photon emission CT. *J Med Phys.* 2010;35(1):42. doi: 10.4103/0971-6203.55967
16. Ljungberg M, Celler A, Konijnenberg MW, Eckerman KF, Dewaraja YK, Sjögren-Gleisner K. MIRD pamphlet no. 26: Joint EANM/MIRD guidelines for quantitative <sup>177</sup>Lu SPECT applied for dosimetry of radiopharmaceutical therapy. *J Nucl Med.* 2016;57(1):151–62. doi: 10.2967/jnumed.115.159012
17. Ljungberg M, Strand SE, King M. The SIMIND Monte Carlo program. *Monte Carlo Calc Nucl Med Appl diagnostic imaging.* 1998;145–63. doi: 10.1201/b13073-8
18. Jan S, Benoit D, Becheva E, Carlier T, Cassol F, Descourt P. GATE V6 : a major enhancement of the GATE simulation platform enabling modelling of CT and radiotherapy. *Phys Med Biol.* 2011;56(4):881–901. doi: 10.1088/0031-9155/56/4/001
19. Sarrut D, Bardiès M, Boussion N, Freud N, Jan S, Létang J. A review of the use and

- potential of the GATE Monte Carlo simulation code for radiation therapy and dosimetry applications. *Med Phys*. 2014;41(6):064301-1–14. doi: 10.1118/1.4871617
20. Ljungberg M, Strand SE. A Monte Carlo program for the simulation of scintillation camera characteristics. *Comput Methods Programs Biomed*. 1989;29(4):257–72. doi: 10.1016/0169-2607(89)90111-9
  21. Kalantari F, Rajabi H, Saghari M. Quantification and reduction of the collimator-detector response effect in SPECT by applying a system model during iterative image reconstruction : a simulation study. *Nucl Med Commun*. 2012;33(3):228–38. doi: 10.1097/MNM.0b013e32834e755f
  22. Minarik D, Sjögreen Gleisner K, Ljungberg M. Evaluation of quantitative <sup>90</sup>Y SPECT based on experimental phantom studies. *Phys Med Biol*. 2008;53:5689–5703. doi: 10.1088/0031-9155/53/20/008
  23. Morphis M, van Staden JA, du Raan H, Ljungberg M. Modelling of energy-dependent spectral resolution for SPECT Monte Carlo simulations using SIMIND. *Heliyon*. 2021;7:12. doi: 10.1016/j.heliyon.2021.e06097
  24. Staelens S, Strul D, Santin G, Vandenberghe S, Koole M, Asseler YD. Monte Carlo simulations of a scintillation camera using GATE : validation and application modelling. *Phys Med Biol*. 2003;48(18):3021–3042. doi: 10.1088/0031-9155/48/18/305
  25. Ejeh JE, van Staden JA, du Raan H. Validation of SIMIND Monte Carlo Simulation Software form Modelling a Siemens Symbia T SPECT Scintillation Camera. 2018. IFMBE proceedings. doi: 10.1007/978-981-10-9035-6\_106
  26. Islamian JP, Taghi M, Toossi B, Momenzhad M, Ljungberg M. Simulation of a Quality Control Jaszczak Phantom with SIMIND Monte Carlo and Adding the Phantom as an Accessory to the Program. *Iran J Med Phys*. 2012;9(2):135–140. doi: 10.22038/ijmp.2012.319
  27. Ramonaheng K, van Staden J, du Raan H. Validation of a Monte Carlo Modelled Gamma Camera for Lutetium-177 Imaging. *Appl Radiat Isot*. 2020;163. doi: 10.1016/j.apradiso.2020.109200

28. Ejeh J. Accuracy of iodine-131 activity quantification and dosimetry for three-dimensional patient-specific models. 2019. [thesis] University of the Free State, Bloemfontein, South Africa
29. National Electrical Manufacturers Association. NEMA Standards Publication NU 1-2012: Performance Measurements of Gamma Cameras. 2012;50.
30. Ferreira T, Rasband W. ImageJ User Guide. 2012;198. Available from: <http://imagej.nih.gov/ij/docs/guide/user-guide.pdf>
31. Frey EC, Tsui BMW. A new method for modeling the spatially-variant, object-dependent scatter response function in SPECT. 1996. IEEE Nuclear Science Symposium Conference Record. IEEE; 1996;1082–1086. doi: 10.1109/NSSMIC.1996.591559
32. Sjögreen K, Ljungberg M, Wingårdh K, Minarik D, Strand SE. The LundADose method for planar image activity quantification and absorbed-dose assessment in radionuclide therapy. *Cancer Biother Radiopharm*. 2005;20(1):92–97. doi: 10.1089/cbr.2005.20.92
33. Loening AM, Gambhir SS. AMIDE: A Completely Free System for Medical Imaging Data Analysis. *J Nucl Med*. 2001;42(5):192.
34. Cherry SR, Sorenson J, Phelps ME, Methé BM. *Physics in Nuclear Medicine*. 4<sup>th</sup> ed. Philadelphia: Saunders; 2012. 1–544
35. Mcgurk RJ. Variation of image counts with patient anatomy and development of a Monte Carlo simulation system for whole-body bone scans. 2007. [thesis] University of Canterbury
36. Tanaka M, Uehara S, Kojima A. Monte Carlo simulation of energy spectra for <sup>123</sup>I. *Phys Med Biol*. 2007;52:4409–4425. doi: 10.1088/0031-9155/52/15/004
37. Westerberg F. Quantification of I-131 Activity from Gamma Camera Images of Thyroid Cancer Patients. 2019. [thesis] Lund University, Lund, Sweden
38. Dewaraja YK, Wilderman SJ, Ljungberg M, Koral KF, Zasadny K, Kaminiski MS. Accurate dosimetry in <sup>131</sup>I radionuclide therapy using patient-specific, 3-dimensional

methods for SPECT reconstruction and absorbed dose calculation. *J Nucl Med.* 2005;46(5):840–849. PMID: PMC2804106

39. Kangasmaa T, Sohlberg A, Kuikka JT. Reduction of Collimator Correction Artefacts with Bayesian Reconstruction in Spect. *Int J Mol Imaging.* 2011;2011:6. doi: 10.1155/2011/630813
40. Autret D, Bitar A, Ferrer L, Lisbona A, Bardiès M. Monte Carlo modeling of gamma cameras for I-131 imaging in targeted radiotherapy. *Cancer Biother Radiopharm.* 2005;20(1):77–84. doi: 10.1089/cbr.2005.20.77

# Chapter 4: Paper III

## **Evaluation of Iodine-123 and Iodine-131 SPECT radioactivity quantification: A Monte Carlo study**

This paper includes work which has been published in *European Journal of Nuclear Medicine and Molecular Imaging Physics* (<https://doi.org/10.1186/s40658-021-00407-1>).

The front page of the article is shown in Appendix C.

# Table of Contents

4.1	Introduction .....	4.2
4.2	Materials and Methods .....	4.7
4.2.1	Optimisation of OS-EM updates.....	4.8
4.2.2	Calibration factors.....	4.9
4.2.3	Recovery coefficient curves.....	4.10
4.2.4	Quantification .....	4.10
4.3	Results .....	4.12
4.3.1	Optimisation of OS-EM updates.....	4.12
4.3.2	Calibration factors.....	4.14
4.3.3	Recovery coefficient curves.....	4.16
4.3.4	Quantification .....	4.16
4.4	Discussion .....	4.19
4.5	Conclusion.....	4.22
4.6	References .....	4.23

## 4.1 Introduction

The branch theragnostics (1) has become a milestone in personalised cancer treatment, bridging the gap between Oncotherapy and Nuclear Medicine (NM). The principle of theragnostics lies in the combination of individualised targeted imaging of a cancer disease and its therapy. Both the diagnostic imaging and therapy procedures typically use the same pharmaceutical; however, in some cases, the diagnostic radionuclide may differ from that used in therapy. This allows for the visualisation of potential target volumes, such as tumours and organs at risk, enabling estimation of potential toxicities and predicting the benefits of such therapy (2,3). Metaiodobenzylguanidine (mIBG), a noradrenaline analogue, was developed in the early 1970s to image tumours in the adrenal medulla (4). mIBG labelled to iodine-123 (I-123) and iodine-131 (I-131) have long been a theragnostic pair. However, due to the recent development of peptide agents, the theragnostics approach has been heightened and the importance of accurate image quantification using I-123 and I-131 re-emphasised (2,5,6).

In I-123 decay, mainly photons are emitted (159.0 keV with 83% abundance, 27.3 keV with 71% abundance and 528.9 keV with 1% abundance) and the decay has a physical half-life of 13.2 hours. I-131, with a physical half-life of 8.04 days, emits both photons (364.5 keV with 82% abundance, 636.9 keV with 7% abundance and 722.9 keV with 1.8% abundance) and several beta particles (with a maximum energy of 606.0 keV and mean energy of 192.0 keV). Due to its shorter half-life and absence of beta particles, I-123 carries a reduced radiation burden compared to I-131, allowing for a higher administered activity for diagnostic imaging and is therefore better suited and favoured for diagnostic imaging. However, in centres where I-123 is not available, I-131 may be administered in lower activities for diagnostic imaging (7,8). Both I-123-mIBG and I-131-mIBG accumulate in neuroendocrine tumours (NETs) as well as in the lungs, liver, kidneys, spleen, bladder, bone marrow and salivary glands (9,10). Therefore, it is essential that accurate activity uptake and related absorbed dose calculations be performed prior to therapy, to optimise the theragnostics' effectiveness by quantitative imaging. Consequently, inaccuracies in the image quantification process may result in incorrect absorbed dose calculations and can lead to a reduction in therapeutic treatment efficacy. Physical factors which can potentially affect the accuracy in the activity estimation from an image are the radionuclide-collimator combination used, the accuracy and precision in the scatter and attenuation correction methods, and the compensation for the limited spatial resolution that results in partial volume effects (PVEs).

High-energy (HE) collimators with thicker septa are needed when imaging I-131 due to the relatively high primary photon energy of 364.5 keV used for imaging and because of the otherwise high septal scatter and penetration from the emission of the 636.9 keV and 722.9 keV photons (11). However, I-123 imaging can be performed with either a low energy high resolution (LEHR) or a medium energy (ME) collimator (12–14). The ME collimator reduces the septal penetration and scatter from the higher-energy photons of I-123, resulting in improved image contrast and more accurate activity quantification. However, when appropriate septal scatter and penetration corrections are applied during image reconstruction, imaging with a LEHR collimator may very well be a useful alternative to a ME collimator (15,16).

Corrections for object scatter, non-homogenous attenuation and collimator-detector response (CDR) as well as collimator-septal scatter and septal penetration can be made by incorporating these effects in the camera/patient model that is the essential part of any iterative reconstruction algorithm. The iterative maximum likelihood-expectation maximisation (ML-EM) algorithm and the closely related ordered subset-expectation maximisation (OS-EM) algorithm are routinely used and typically available on most commercial single-photon emission computed tomography/computed tomography (SPECT/CT) systems (17,18). The basic steps in an iterative reconstruction algorithm are shown in Figure 4.1. The main assumption is that if starting with an initial estimate of the activity distribution (blank or uniform image), the imaging process and the radiation transport are modelled in a forward projection to obtain the expected SPECT projections. These expected projections are then compared to measured projections, and an error projection is calculated as either the difference or the ratios of the expected and measured projections. The error projection is then back projected to create an error image. Once sufficient angles are processed (all or a subset of angles depending on the reconstruction algorithm), the error image is then used to update the source distribution estimate. The process is repeated (iterates) until the ratios converge to unity (i.e. maximizing the likelihood). When the expected and measured projections agree, within a defined margin, it is assumed that the reconstructed images reflect the activity distribution in the patient and the process stops. However, the assumption is only valid if the same physical processes present in the real measurement are also modelled in the forward projection of the expected projection.



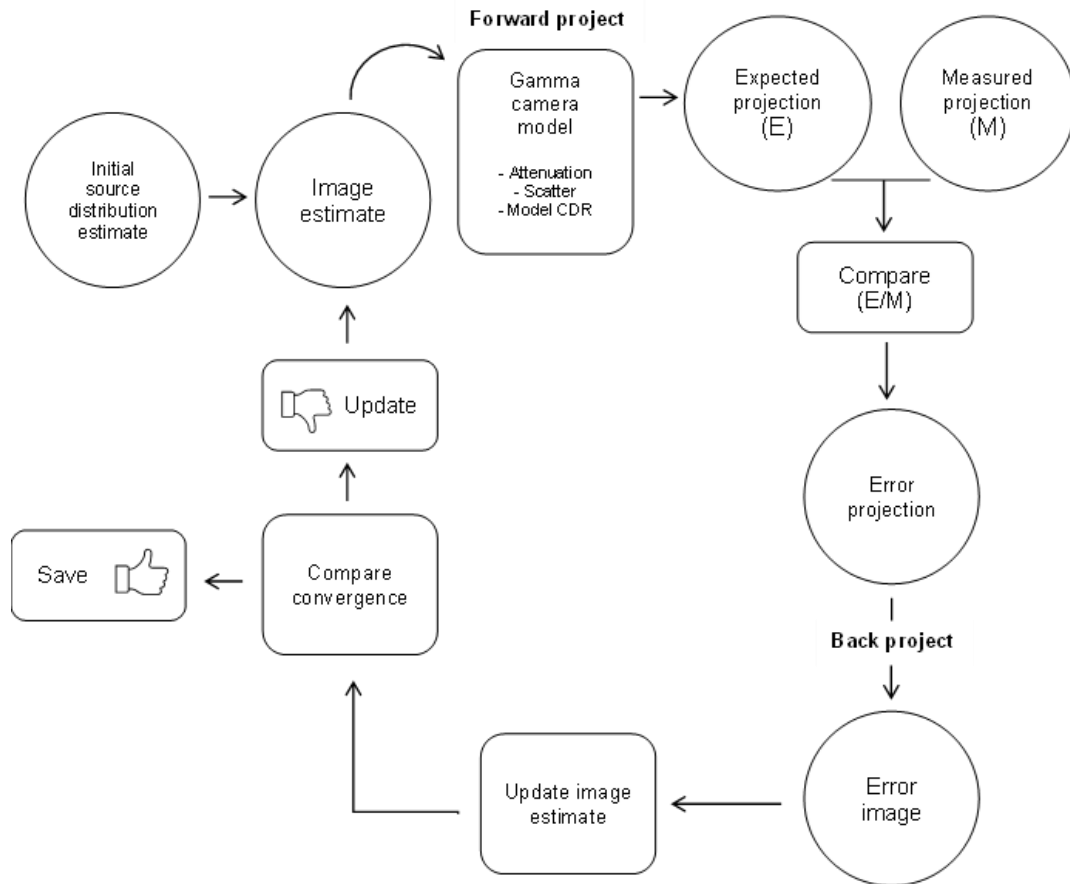


**Figure 4.1.** Schematic describing basic steps of iterative reconstruction method.

As the number of iterations increases, the reconstruction bias (difference between the estimated and measured data) is reduced, at the cost of image noise and reconstruction time. At a certain point, a further increase in the number of iterations will only increase image noise and reconstruction time (19). Thus, it is important to determine the optimal number of OS-EM updates (number of subsets multiplied by the number of iterations) prior to reconstructing SPECT images for activity quantification purposes.

Another prerequisite for absolute SPECT activity quantification is the conversion of reconstructed image counts to activity or activity concentration, using a gamma camera calibration factor (CF) (20). Different methods of establishing such calibration factors (CFs) have been suggested. The simplest method is a planar acquisition of a small point-like source in air, where self-attenuation within the source is kept minimal, and corrections for scatter have been applied (21). The gamma camera system sensitivity obtained from a petri-dish source in air, as defined by the National electrical manufacturers association (NEMA), has also been proposed (22). However, according to the definition of system sensitivity, counts in the entire

image are used. This may be problematic for radionuclide-collimator combinations such as I-123 with the LEHR collimator and I-131 with the HE collimator. For these radionuclide-collimator combinations, a significant number of counts, originating from the higher energy photons which have penetrated the collimators' septa, are detected within the main photopeak energy window. It is generally believed that a CF obtained with a source geometry that mimics the scatter and attenuation conditions in a patient is better suited (11). SPECT acquisitions of geometries such as spheres in air or in water-filled cylindrical phantoms have been recommended, thereby reducing the effects of inadequate compensation for scatter and attenuation (20). Both planar-based and SPECT-based CF methods rely on accurate corrections for scatter and attenuation (23,24). Unlike for planar imaging, corrections for scatter, attenuation and CDR are now often implemented in clinical workstations and thus can be routinely performed on SPECT/CT image data sets, making the SPECT-based CF the method of choice. Considering that the same corrections are applied to both the clinical and the CF data set, any effects of imperfect correction methods would be minimised.

In SPECT imaging, the partial volume effect (PVE) is the result of the gamma camera's finite spatial resolution and the discretisation of the measured coordinates from the gamma camera to a digital image. This results in a reduction of image contrast between the regional uptake and surrounding areas. The PVE is also a primary source-of-error when estimating activity in volumes-of-interest (VOIs) with sizes that are in the order of the camera's resolution. Typically, VOIs smaller than three times the systems spatial resolution appear to contain less than the actual activity concentrations (25). PVEs are only partially compensated for when SPECT images are reconstructed with CDR compensations. Therefore, a simple and effective method for the correction of residual PVEs is to use recovery coefficients (RCs) determined for objects of similar sizes as the VOIs. RCs are often expressed as the ratio of the estimated activity concentration in a volume of interest (VOI) to the true activity concentration. RCs can be obtained from phantom measurements where the geometry of the sources and its activity concentrations are known or through Monte Carlo (MC) simulations where RCs for more irregular and arbitrary shapes can be defined (26). A curve of RCs as a function of object size can be generated and a recovery coefficient (RC) value for a relevant VOI size can then be applied in the activity quantification process (24,27–29). Often spherical sources are used to obtain RCs, but it should be noted that the RC also depends on the shape of the object (30). Since the variation of tumours can vary significantly, it is hard to obtain RC curves for every possible tumour shape. It is common to compensate for PVEs of non-spherical tumours by

applying volume-specific RCs which were determined from spherical phantoms, but this method has been reported to have limitations (31).

The MC method is an important tool to evaluate the quantification accuracy and its effects on the accuracy of dosimetry for a given SPECT/CT procedure. The MC modelling of gamma cameras for imaging of radionuclides (including technetium-99m (Tc-99m), I-131 and lutetium-177 (Lu-177)) have been reported extensively (11,32,33). There are various MC simulation codes available for NM imaging (34–36). In this study we used the Simulation of imaging nuclear detectors (SIMIND) MC code which models a standard clinical scintillation camera and has been successfully used to evaluate activity quantification accuracy (27,37–39). SIMIND allows for three methods to simulate the energy resolution, based on either (i) a simplified theoretical model assuming a  $1/\sqrt{E}$  dependence (25,40), (ii) a fixed energy resolution used over the entire energy range, or (iii) a fitted model estimated from measured data (41). A fitted energy resolution model improves the energy resolution modelling of high-energy photon emitting radionuclides (e.g., I-131) and radionuclides with multiple photopeak's (e.g., I-123, I-131 and Lu-177) and was therefore used in this study. SIMIND has been validated for simulating I-123 and I-131 images with the proposed fitted energy resolution model by Morphis et al. (41).

Although activity quantification accuracy with SIMIND has been reported in literature (27,42,43), little work has been done using voxel-based digital phantoms for I-123 and I-131. Furthermore, to our knowledge, evaluating activity quantification accuracy in a clinically realistic phantom, using SIMIND with the fitted energy resolution model, has not yet been reported in literature.

The aim of the study was to evaluate SPECT activity quantification accuracy for I-123 with both the LEHR and ME collimators, and I-131 with the HE collimator, using the SIMIND MC code with a fitted energy resolution model. The objectives included (i) the optimisation of the number of OS-EM updates for the SPECT iterative reconstruction algorithm, (ii) determination of a CF, (iii) determination of RC curves, and (iv) evaluation of the quantitative method in voxel-based digital simple and patient phantoms.

## 4.2 Materials and Methods

The Siemens Symbia T16 (Siemens Healthcare, Erlangen, Germany) dual-head SPECT/CT system with LEHR, ME and HE collimators, in use at Universitas Academic Hospital (UAH) (Bloemfontein, South Africa), was modelled using version 6.2 of the SIMIND MC code (39). The setup of the virtual gamma camera (detector and collimators) and the simulation specifications were the same as that described and validated by Morphis et al. (41,44).

Voxel-based digital phantoms were created from CT images of a water-filled cylindrical phantom (internal diameter: 20.3 cm, external diameter: 21.6 cm and length: 31.7 cm) (45), as well as from a randomly selected retrospective patient SPECT/CT dataset from the UAH patient database. These voxel-based digital phantoms were segmented and created as described by Ramonaheng et al. (27,46) and Morphis et al. (41,44).

SPECT projections images were simulated for I-123 for both the LEHR and ME collimators (further referred to as I-123 LEHR and I-123 ME, respectively) and I-131 using the HE collimator (I-131 HE). As part of the simulation process, Poisson noise was added to the projection data. Energy windows of 15.0% were centred over the 159.0 keV and 364.0 keV photopeak's of I-123 and I-131, respectively. The images were simulated according to a standard clinical imaging protocol (step and shoot mode, non-circular orbit of rotation, 60 projections in total, 40 seconds per projection, matrix size:  $128 \times 128$ , pixel size:  $4.8 \times 4.8 \text{ mm}^2$ ). Simulations were performed with a high number of histories ( $> 10^9$ ) (43).

SPECT reconstruction was performed using software developed at Lund University, Sweden (47), which incorporates an OS-EM iterative reconstruction package, developed by Frey and Tsui (48). The iterative reconstruction algorithm performs a CT-based attenuation correction, model-based scatter correction by the Effective Scatter Source Estimation algorithm (ESSE), and a CDR correction, which accounts for collimator septal penetration and scatter by using pre-calculated MC simulated kernels (49). The SPECT images were reconstructed in a  $128 \times 128 \times 128$  matrix with a voxel size of  $4.8 \times 4.8 \times 4.8 \text{ mm}^3$ . Reconstructed image count statistics (total, mean and standard deviations) were obtained using the public domain software, Amide (50).

### 4.2.1 Optimisation of OS-EM updates

When determining the optimal number of OS-EM updates, it is essential to consider the trade-off between bias, image noise and reconstruction time. To determine the optimal number of OS-EM updates and evaluate activity recovery as a function of the number of OS-EM updates, four spheres, with volumes of 1.8, 14.1, 47.7 and 113.1 mL (diameters: 1.5, 3.0, 4.5 and 6.0 cm), were digitally added to a segmented image of the water-filled cylindrical phantom. Different sized spheres were chosen to ensure coverage of at least one to four times the planar spatial resolution of I-131 when imaged with the HE collimator (spatial resolution of 1.3 cm).

SPECT projections were simulated, with simulation parameters as explained above, for I-123 and I-131, using sphere activity concentration values of 0.7 MBq/mL and 1.1 MBq/mL, respectively. The concentration values were based on clinical I-123 and I-131 mIBG tumour data at approximately 24 hours post-administration, assuming diagnostic injected activity of 370.0 MBq and 185.0 MBq for I-123 and I-131, respectively. The SPECT projections were reconstructed using LundADose, as described above. A series of 17 reconstructions were performed for each radionuclide-collimator combination, with six subsets, as proposed in literature (11,19), and OS-EM updates varying from 18 to 168. Count statistics (expressed as counts per second per mL) were obtained for each reconstructed sphere, with spherical VOIs equal to the sphere's physical size. Each VOI value was normalised to the overall maximum VOI value (33).

Brambilla et al. (51) and Leong et al. (52) evaluated reconstruction noise by assessing the change in the reconstruction noise level within a uniform area of a single slice. However, Ramonaheng et al. (27) suggested assessing the change in reconstruction noise level within a target VOI, obtained using the object's physical size. The object's physical size provides a constant and reliable delineation method, which is the same as that used to assess count recovery. As proposed by Ramonaheng et al. (27), the reconstruction noise levels in each sphere were calculated using Equation 4.1,

$$SD_{relative} = \frac{SD}{mean} \times 100 \quad (4.1)$$

where  $SD_{relative}$  is the relative standard deviation,  $SD$  and  $mean$  are the standard deviation and mean counts per voxel of the reconstructed counts from the VOI of the sphere. It is important to note that  $SD_{relative}$  is only an estimation of reconstruction noise (53). Furthermore, in scenarios where CDR correction is included in the iterative reconstruction, the effect of the

Gibbs artifact increases with an increase in the number of iterations, thus the  $SD_{relative}$  will include this variation.

The normalised recovered counts and  $SD_{relative}$  values per sphere size were plotted as a function of the number of OS-EM updates. The optimal number of OS-EM updates was determined from the recovered counts based on the graphs for each radionuclide-collimator combination and used in the subsequent reconstructions.

The optimal number of OS-EM updates was confirmed in a clinically realistic voxel-based digital patient phantom, where the activity recovery in a 14.1 mL (diameter: 3.0 cm) sphere was evaluated at several of the OS-EM updates.

#### 4.2.2 Calibration factors

For each radionuclide-collimator combination, four different source geometries were used to determine the gamma camera SPECT CFs. The source geometries included a large activity-filled cylindrical phantom ( $CF_{cylinder}$ ), a 113.1 mL (diameter: 6.0 cm) activity-filled sphere in the water-filled (cold) cylindrical phantom ( $CF_{water}$ ), a 113.1 mL activity-filled sphere in air ( $CF_{air}$ ) and a point-like source (volume < 1 mL) in air ( $CF_{point}$ ). Concentration values for the four different CF source geometries were the same as the concentration value used to determine the optimal number of OS-EM updates.

SPECT projection images were simulated with the phantoms placed at the centre of the gamma camera's field of view and reconstructed using the optimised reconstruction parameters. Count statistics were obtained for each reconstructed CF source geometry. Cylindrical or spherical VOIs were defined based on the CF source geometry (cylindrical for  $CF_{cylinder}$  and spherical for the remaining geometries). Three VOI sizes with diameters of (i) less than the physical size, (ii) the physical size plus a 3.0 cm margin or (iii) the physical detector size, were defined. To determine the  $CF_{cylinder}$ , all three VOI diameters were used but only VOI diameter (ii) and (iii) were chosen for the remaining CFs. Due to the presence of Gibbs artefacts in the  $CF_{water}$  and  $CF_{air}$  images, and to the limited size of the point source for  $CF_{point}$ , VOIs smaller than the sources physical size were not considered. The CFs were calculated using Equation 4.2,

$$CF = \frac{Cnt}{A \times t} \left( \frac{cps}{MBq} \right) \quad (4.2)$$

where  $Cnt$  is the total image counts obtained in each VOI,  $A$  is the simulated activity in the source, and  $t$  the simulated acquisition time. From this, an appropriate CF source geometry was determined for all radionuclide-collimator combinations.

Energy spectra were also obtained from the  $CF_{point}$  SPECT simulations for each radionuclide-collimator combination to determine any possible contributions of septal scatter and penetration to the CFs.

### 4.2.3 Recovery coefficient curves

RCs were determined for the dual-head Siemens Symbia T16 SPECT/CT gamma camera. Eight spheres, with volumes ranging from 8.2 to 523.6 mL (diameters: 2.5 to 10.0 cm), were digitally added to the segmented images of the water-filled cylindrical phantom. SPECT projections were simulated, with sphere activity concentration values and simulation parameters as explained above. Simulations were performed without background activity in the cylindrical phantom, to avoid any biased results in the quantification accuracy. The SPECT projections were reconstructed using the optimised reconstruction parameters. Count statistics with VOIs defined by the physical sphere size were obtained for each sphere using the predetermined CF geometry and reported in units of MBq/mL. The recovered and true activity concentration ( $[A]_{recovered}$  and  $[A]_{true}$ ) values were used to calculate the RCs, according to Equation 4.3,

$$RC = \frac{[A]_{recovered}}{[A]_{true}} \quad (4.3)$$

The RCs for each radionuclide-collimator combination were plotted as a function of sphere diameter and fitted with a mono-exponential function (Equation 4.4), proposed by Willowson et al. (24),

$$RC = a - be^{-cx} \quad (4.4)$$

where  $x$  represents the sphere diameter (cm), and  $a$ ,  $b$  and  $c$  are the curve fitting parameters.

### 4.2.4 Quantification

#### 4.2.4.1 Spheres in the cylindrical phantom

To evaluate the accuracy of the quantification method, the error of the estimated activity in spheres (volumes ranging from 8.2 to 523.6 mL) in an activity-filled cylindrical phantom was determined. Activity concentration values were based on clinical I-123 and I-131 mIBG pharmacokinetic data observed at 24-hours post-injection (sphere to background ratio of

100:1). The recovered activity concentration was calculated using the predetermined CF and corrected for PVE using RCs obtained from the RC curve, for each radionuclide-collimator combination. The quantification error was defined as the percentage difference between the recovered activity concentration ( $[A]_{recovered}$ ) and the true activity concentration ( $[A]_{true}$ ) defined in SIMIND, shown in Equation 4.5,

$$Quantification\ Error\ (\%) = \frac{[A]_{recovered} - [A]_{true}}{[A]_{true}} \times 100 \quad (4.5)$$

#### 4.2.4.2 Voxel-based digital patient phantoms

Two different sized spheres were added to a voxel-based digital patient phantom, to determine the accuracy in a clinically realistic phantom. As shown in Figure 4.2, two scenarios were considered; scenario 1 included a sphere with a diameter of 5.0 cm positioned above the liver between the lungs, and a second sphere with a diameter of 3.0 cm positioned below the liver. For scenario 2, the positions of the two spheres were switched. Activity concentration values were based on clinical I-123 and I-131 mIBG pharmacokinetic data observed at 24-hours post-injection (sphere to background ratio of 100:1, sphere to liver ratio of 100:7.5 and sphere to lung ratio of 100:2.8).

I-123 and I-131 SPECT projections were simulated and reconstructed as previously described. Count statistics were obtained with VOIs defined according to the physical size of the spheres and the liver. Sphere and liver activity concentrations were calculated using the predetermined CF geometry and corrected for PVE using the appropriate RC obtained from the RC curve. The error in the recovered activity concentration was determined using Equation 4.5.

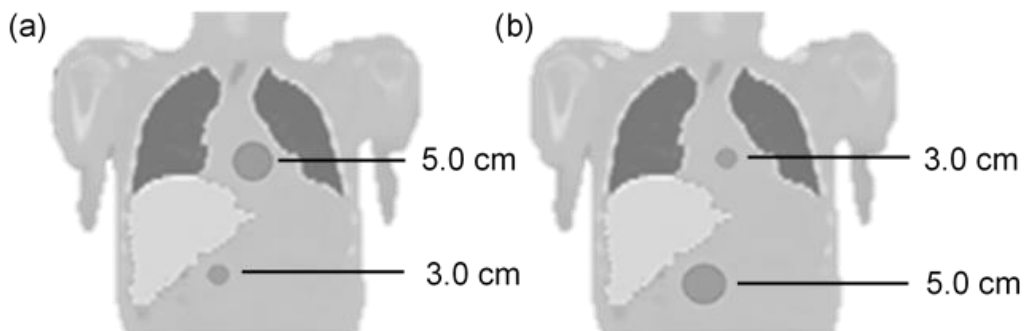


**Figure 4.2.** Segmented coronal CT slices of the voxel-based digital patient phantom with spheres' positions for (a) scenario 1 and (b) scenario 2.



## 4.3 Results

### 4.3.1 Optimisation of OS-EM updates

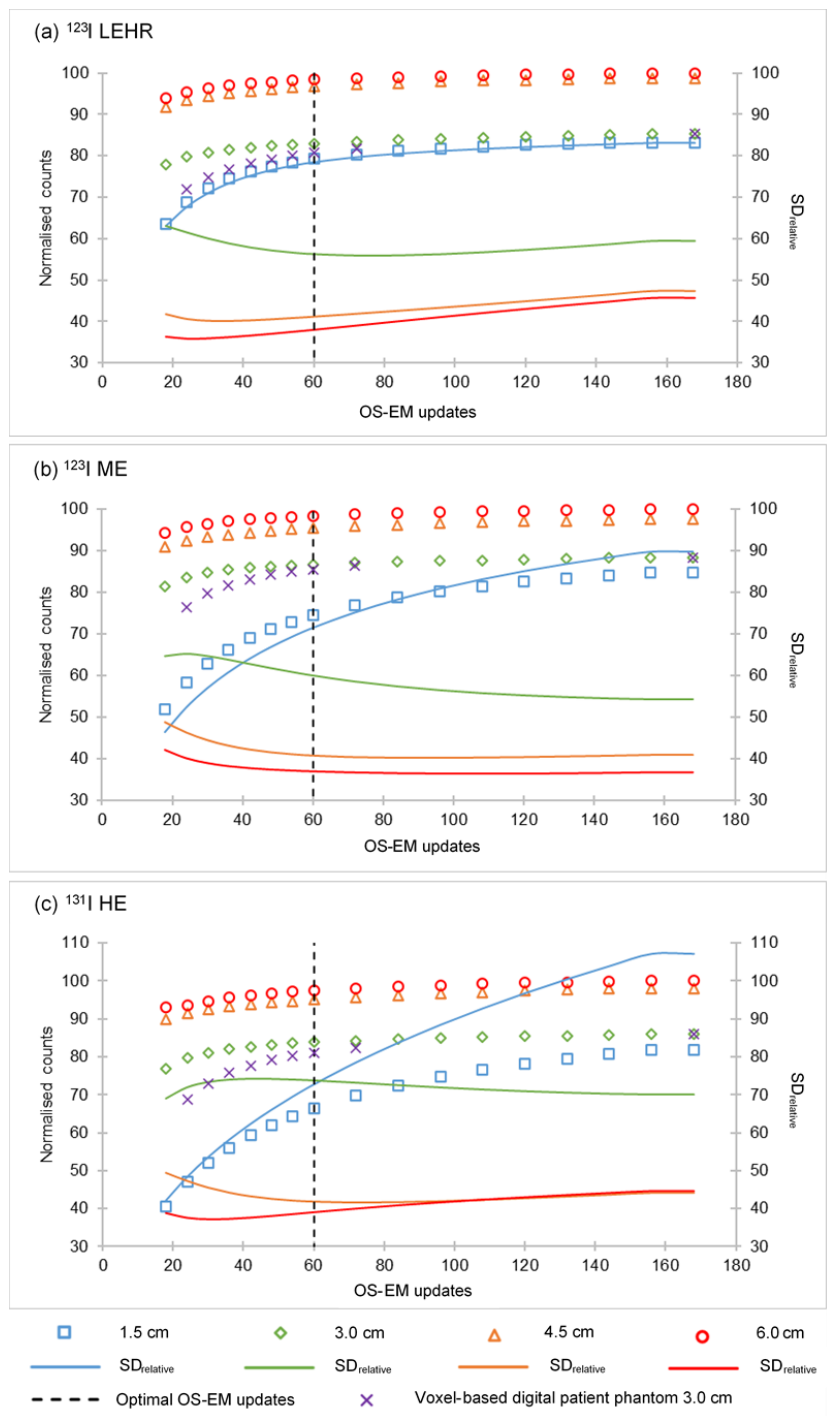
The relationship between the number of OS-EM updates and (i) the recovered counts and (ii)  $SD_{relative}$ , for each sphere size is illustrated in Figure 4.3 for all radionuclide-collimator combinations.

Figure 4.3a, Figure 4.3b and Figure 4.3c show that count convergence (fast increase followed by a slower approach towards an asymptote) is reached relatively quickly for the three largest spheres, compared to the smallest sphere. Eighteen OS-EM updates resulted in more than 90% count recovery for the two larger spheres (4.5 cm and 6.0 cm), for all radionuclide-collimator combinations. However, more OS-EM updates were required to reach count convergence for the two smallest spheres (1.5 cm and 3.0 cm). This can be attributed to the limited spatial resolution and the pronounced PVE of I-123 LEHR, I-123 ME and I-131 HE (16).

The graphs in Figure 4.3 show that for all radionuclide-collimator combinations reaching 60 OS-EM updates, a further increase in OS-EM updates would not improve count recovery by more than 3.0% for the three larger spheres and 16.0% for the smallest sphere. The change in  $SD_{relative}$  from 18 OS-EM updates to 60 OS-EM updates was less than 8.0% for the three larger spheres. The smallest sphere resulted in a  $SD_{relative}$  increase of 15.0% (improved count recovery of 16.0%), 16.0% (improved count recovery of 23.0%) and 25.0% (improved count recovery of 26.0%) for I-123 LEHR, I-123 ME and I-131 HE, respectively. The count recovery improved by a maximum of 1.0% for the three largest spheres (2.0% increase in  $SD_{relative}$ ) and 6.0% for the smallest sphere (9.0% increase in  $SD_{relative}$ ), when moving from 54 OS-EM updates to 72 OS-EM updates, across all radionuclide-collimator combinations. With the goal of accurate activity quantification, an improvement in count recovery was favoured. However, based on only a 1.0% increase in count recovery from 54 OS-EM updates to 72 OS-EM updates (excluding the smallest sphere), 60 OS-EM updates were considered optimal for all radionuclide-collimator combinations. This was confirmed by the recovered activity in the 3.0 cm sphere (mimicking a tumour) in the voxel-based digital patient phantom. The average increase in count recovery from 54 OS-EM updates to 72 OS-EM updates was 1.8%. A further increase in the number of OS-EM updates did not improve count recovery by more than 4.7%.

If the goal is to perform accurate activity quantification for small objects (1.5 cm and less), it may be considered to further increase the number of OS-EM updates, keeping in mind the

simultaneous increase in image noise. It should also be noted that for the smallest sphere, full recovery is not reached at 168 OS-EM updates, however, the use of a RC could further improve the quantification accuracy.



**Figure 4.3.** Normalised counts and  $SD_{relative}$  as a function of OS-EM updates for spheres with diameters of 1.5 cm, 3.0 cm, 4.5 cm, and 6.0 cm, for (a) I-123 LEHR, (b) I-123 ME and (c) I-131 HE.

### 4.3.2 Calibration factors

Table 4.1 shows the CFs for the different source geometries and VOI diameters. The relative SDs for the average of the four CFs, when selecting a VOI diameter equal to the physical source diameter plus 3.0 cm, were 2.9%, 1.1% and 1.5% for I-123 LEHR, I-123 ME and I-131 HE, respectively. Similar results were obtained when selecting the VOI equal to the detector's physical size (relative SDs of 1.9%, 0.8% and 4.7% for I-123 LEHR, I-123 ME and I-131 HE, respectively). For I-123 LEHR, the selection of the different VOI margins resulted in a 5.0% difference in CF between VOI selection (i) and (ii), 13.0% difference in CF between VOI selection (i) and (iii) and 19.0% difference in CF between VOI selection (ii) and (iii). The corresponding differences obtained for I-123 ME were all less than 2.2%. I-131 HE resulted in differences of 1.1%, 7.2% and 8.4%, respectively. These results show that the effect of VOI selection is more pronounced for I-123 LEHR and I-131 HE. This can be attributed to unwanted septal scatter and penetration, which were not fully corrected for using the OS-EM reconstruction and the appropriate correction methodologies.

**Table 4.1**

**CFs for I-123 with the LEHR and ME collimator and I-131 with the HE collimator, in cps/MBq, for the four CF source geometries. VOI diameters were defined as (i) less than the physical source diameter, (ii) equal to the physical source diameter plus a 3 cm margin, and (iii) equal to the physical size of the detector.**

VOI diameter		I-123 LEHR (cps/MBq)	I-123 ME (cps/MBq)	I-131 HE (cps/MBq)
i	CF <sub>cylinder</sub>	89.3	119.0	27.7
	CF <sub>cylinder</sub>	88.4	115.6	26.8
ii	CF <sub>water</sub>	84.4	118.2	27.6
	CF <sub>air</sub>	82.4	116.4	27.2
	CF <sub>point</sub>	84.1	115.5	27.8
	Average ± SD	84.8 ± 2.5	116.4 ± 1.3	27.4 ± 0.4
	Relative SD (%)	2.9	1.1	1.5
iii	CF <sub>cylinder</sub>	100.4	118.9	28.6
	CF <sub>water</sub>	102.2	120.2	29.1
	CF <sub>air</sub>	98.4	117.7	29.4
	CF <sub>point</sub>	102.4	118.7	31.7
	Average ± SD	100.9 ± 1.9	118.9 ± 1.0	29.7 ± 1.4
	Relative SD (%)	1.9	0.8	4.7

To better visualise the effect of septal scatter and penetration, simulated energy spectra of  $CF_{\text{point}}$  projection images are shown in Figure 4.4. Higher levels of septal penetration (indicated by the arrows) can be seen in Figure 4.4a compared to Figure 4.4b and Figure 4.4c. This further highlights the importance of accurate septal scatter and penetration corrections, which could be the cause of the larger difference between CFs with VOI diameters (i) and (ii) to that of (iii) for I-123 LEHR, as shown in Table 4.1. For this reason, the use of VOI diameter (iii) was not considered further.

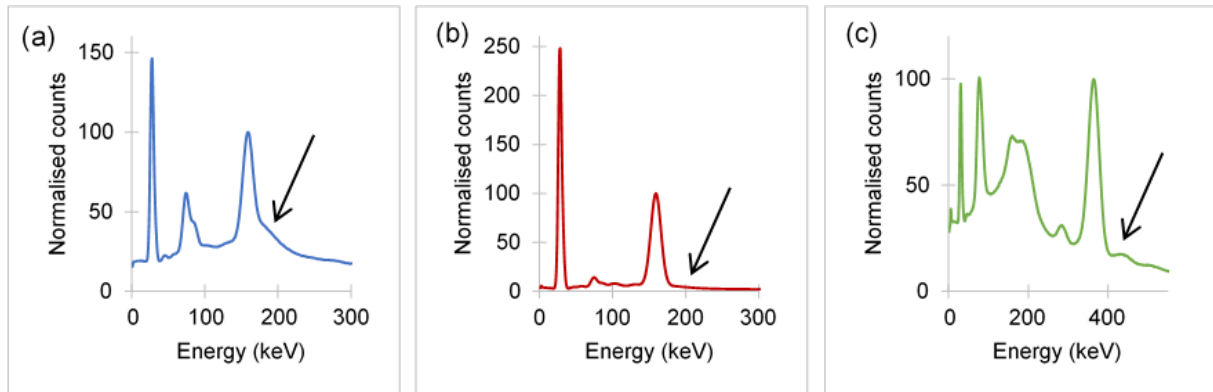


**Figure 4.4.** Simulated energy spectra of  $CF_{\text{point}}$  projection images for (a) I-123 LEHR, (b) I-123 ME, and (c) I-131 HE.

When considering the use of I-131 in the clinic, considering the high-cost implications, the possibility of contamination, the high radiation risk to staff members due to its high photon energy, emission of beta particles, long half-life and volatility, as well as its impracticality of use in the clinical environment, the use of  $CF_{\text{cylinder}}$  was not considered further, despite being recommended by others (29,62). For this reason, VOI diameter (i) was also not considered further. When comparing the results of the remaining three geometries under the remaining VOI diameter (ii), maximum differences of 2.0 cps/MBq (between  $CF_{\text{water}}$  and  $CF_{\text{air}}$ ), 3.7 cps/MBq (between  $CF_{\text{water}}$  and  $CF_{\text{point}}$ ) and 0.6 cps/MBq (between  $CF_{\text{air}}$  and  $CF_{\text{point}}$ ) were noted for I-123 LEHR, I-123 ME and I-131 HE, respectively.

Based on these findings, the  $CF_{\text{point}}$  with a VOI diameter equal to the physical size plus a 3.0 cm margin, representing the simplest geometry and easiest to replicate in the clinical environment, was considered appropriate to use as a CF for all radionuclide-collimator combinations.

### 4.3.3 Recovery coefficient curves

Figure 4.5 shows the calculated RCs as a function of sphere diameter for all radionuclide-collimator combinations. The mono-exponential functions fitted to the data, allowing for interpolation between sphere sizes, had  $R^2$  values of 0.99 for all radionuclide-collimator combinations. From Figure 4.5 it is evident that for I-123 LEHR and I-123 ME, more than 90.0% ( $RC > 0.9$ ) of the activity concentration is recovered for spherical sources with diameters equal to and larger than 5.0 cm. Comparatively, more than 80.0% ( $RC > 0.8$ ) of the activity concentration was recovered for I-131 HE at sphere diameters of 5.0 cm and more, and 90.0% ( $RC > 0.9$ ) at sphere diameters equal to and larger than 7.0 cm. This emphasises the impact of PVEs for radionuclide-collimator combinations with poorer spatial resolution, such as I-131 HE.

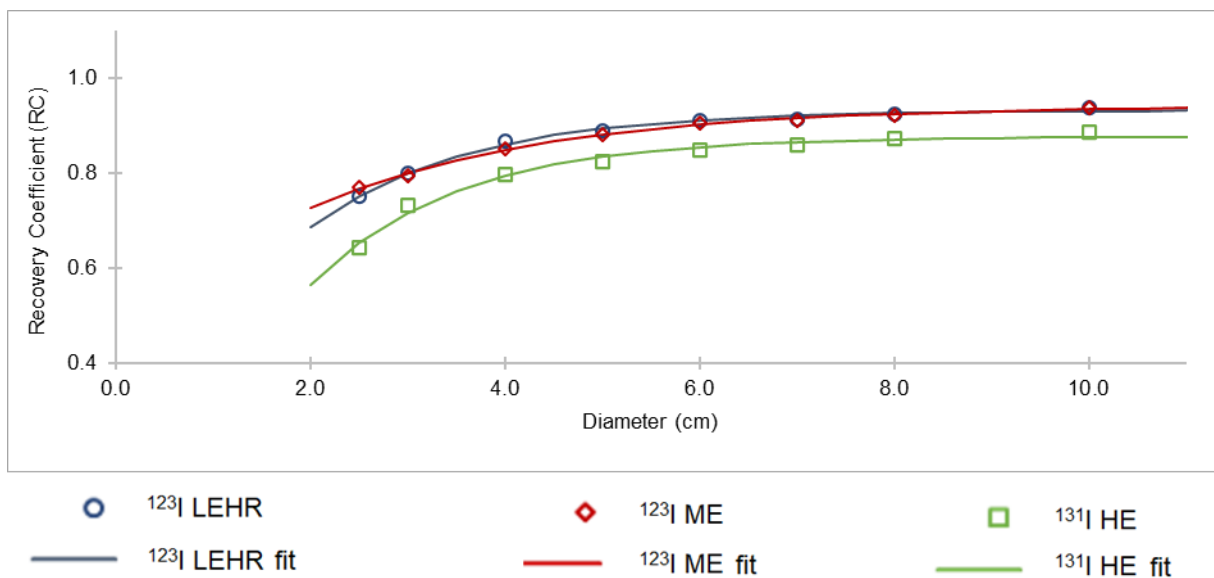


**Figure 4.5.** RC as a function of sphere diameter for I-123 LEHR, I-123 ME and I-131 HE, with the solid lines showing the fitted functions.

### 4.3.4 Quantification

#### 4.3.4.1 Spheres in the cylindrical phantom

The quantification error, as defined by Equation 4.5, for spheres with diameters ranging from 2.5 to 10.0 cm, in the activity-filled cylindrical phantom, for all radionuclide-collimator combinations, is shown in Figure 4.6. Overall, percentage quantification errors were less than 3.2% for all radionuclide-collimator combinations.

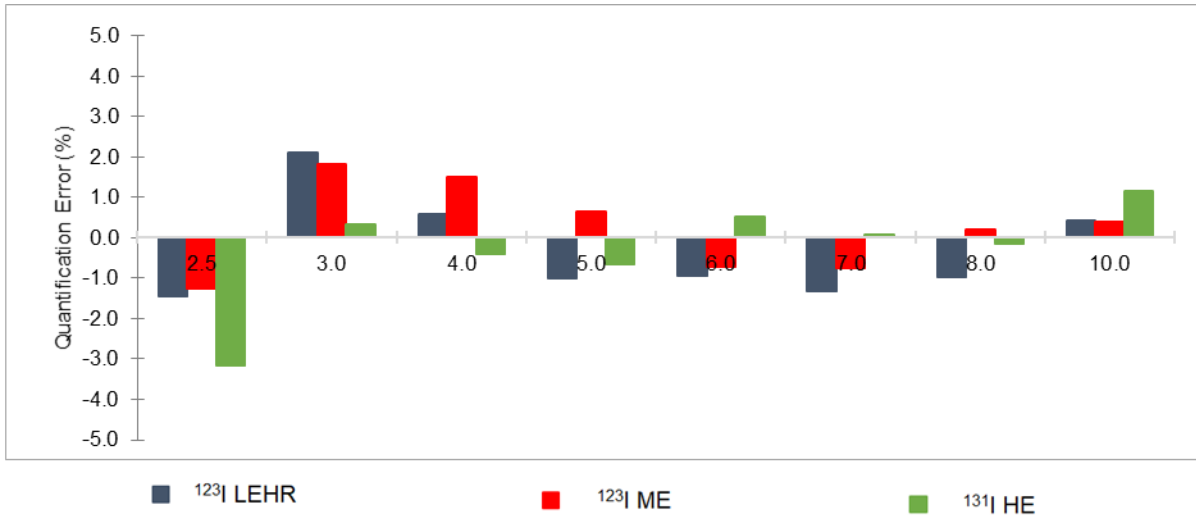


**Figure 4.6.** Quantification error (%) of spheres of differing diameter in the activity-filled cylindrical phantom, for I-123 LEHR, I-123 ME and I-131 HE.

#### 4.3.4.2 Voxel-based digital patient phantoms

Figure 4.7 shows projection images and reconstructed transaxial slices of the voxel-based digital patient phantom for all radionuclide-collimator combinations. Additionally, profiles through the largest sphere (diameter: 5.0 cm) are shown alongside their respective images.

Differences in background counts due to collimator septal scatter and penetration can be seen between I-123 LEHR and I-123 ME in Figure 4.7a and Figure 4.7c, respectively. The presence of septal scatter and penetration is further illustrated with the profile through the 5.0 cm sphere, as shown by the arrows in Figure 4.7a compared to Figure 4.7c. However, comparing the reconstructed slices and the profile through the 5.0 cm sphere, as shown in Figure 4.7b and Figure 4.7d, it can be seen that septal scatter and penetration is sufficiently compensated for the case of I-123 LEHR (ratio of peak to trough counts increased). Overall, the I-123 LEHR images appear slightly noisier compared to I-123 ME. This can be attributed to poorer counts statistics due to the reduced sensitivity of I-123 LEHR compared to I-123 ME, considering equal amounts of activity were simulated in each. The effects of septal scatter and penetration are notably lower for I-131 HE, as shown in Figure 4.7e and Figure 4.7f. Visually, the I-123 ME images are comparable to the I-131 HE images. Similar differences have been reported in literature by Nakajima et al. (54).

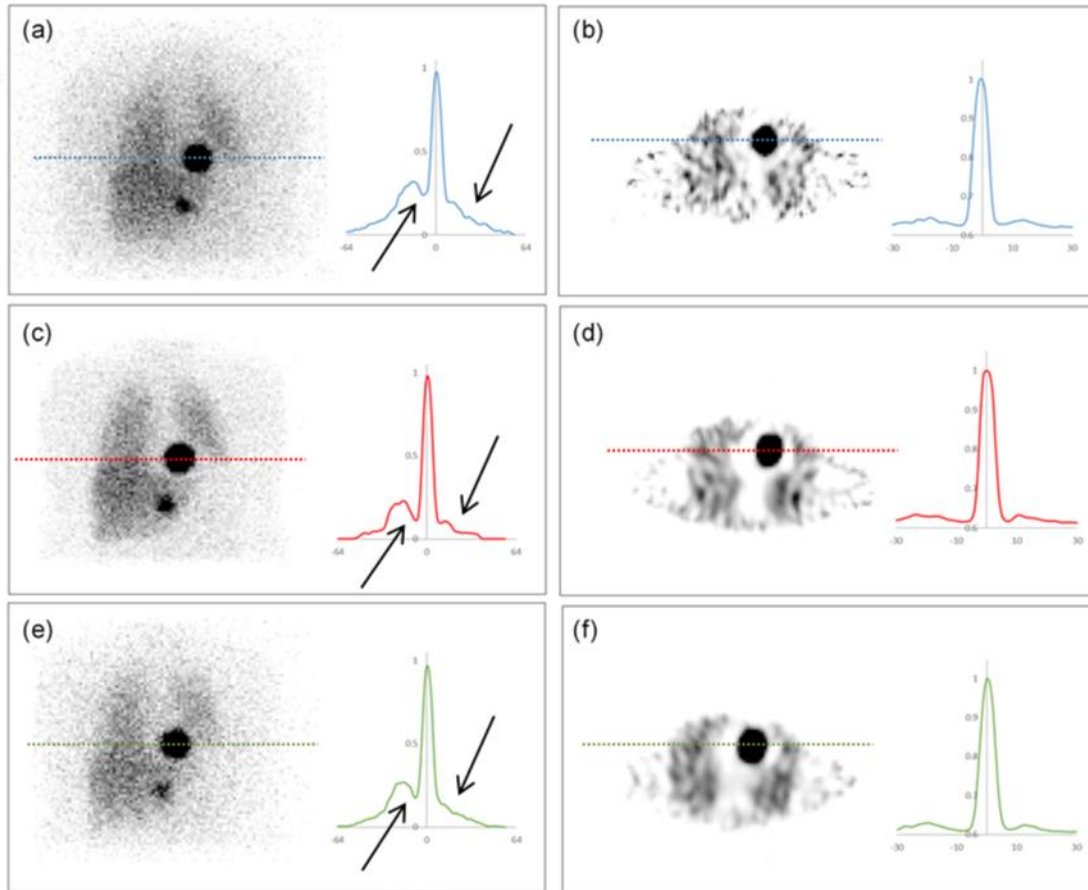


**Figure 4.7.** Uncorrected projection images (a, c, e), and reconstructed corrected transaxial slices (b, d, f) through the voxel-based digital patient phantom for (a, b) I-123 LEHR, (c, d) I-123 ME, and (e, f) I-131 HE. Profiles through the largest sphere are displayed alongside their respective images. Arrows indicate septal scatter and penetration at peak and trough and at tail region.

The activity quantification errors in the two spheres are shown in Figure 4.8 for all radionuclide-collimator combinations. The 3.0 cm and 5.0 cm spheres show an absolute quantification error of less than 5.4% for all radionuclide-collimator combinations for both scenarios 1 and 2. For the liver, absolute quantification errors of less than 5.2% are noted across all radionuclide-collimator combinations.

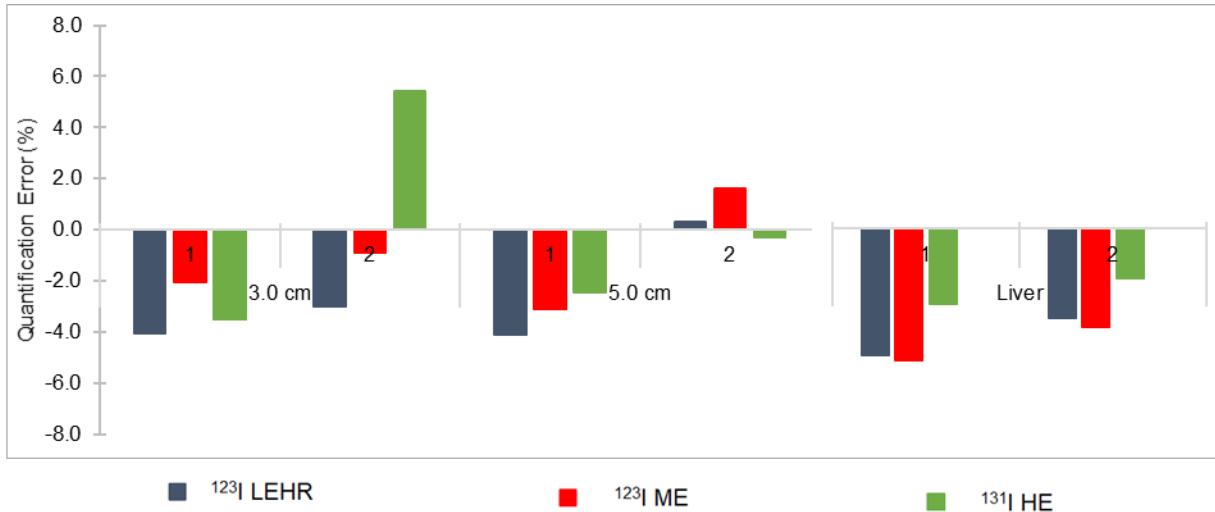


**Figure 4.8.** Activity quantification errors (%) for spheres in the voxel-based digital patient phantom (scenario 1 and 2), for I-123 LEHR, I-123 ME, and I-131 HE.

#### 4.4 Discussion

The purpose of our work was to evaluate the accuracy of activity quantification for SPECT imaging when using *I-123* with both the LEHR and ME collimators, and for *I-131* with the HE collimator.

##### Optimisation of OS-EM updates

From the results, it is evident that optimisation of the number of OS-EM updates is important for accurate SPECT activity quantification. Literature states that smaller objects require a larger number of OS-EM updates to improve reconstruction accuracy (19), which corroborates our results, as shown in Figure 4.3.

From literature, it is well known that increasing the number of OS-EM updates, increases image noise for some radionuclides, including Tc-99m (52), I-131 (43,55,56) and Lu-177 (27,57,58). The results in Figure 4.3 corroborate that stated in literature, showing that the image of the smallest sphere has the largest  $SD_{relative}$  value, and that the value decreases as the sphere size increases.

Figure 4.3 also shows that the optimal number of OS-EM updates is object size-dependent. Based on these findings, the optimal number of OS-EM updates was found to be 60 for all radionuclide-collimator combinations. Our study's findings were similar to results reported in the literature (11,19,59). The choice of optimal number of OS-EM updates was confirmed by similar convergence obtained with the voxel-based digital patient phantom (Figure 4.5).



### Calibration factors

Literature reports the use of several CFs, which include the activity-filled cylindrical phantom, point-like or spherical source in air (20,21). The simplest way of determining a CF is from a point-like source in-air. However, this method relies on SPECT data which has been reconstructed with high accuracy. To account for any uncertainties in the reconstruction process, a more reliable source geometry is one which better approximates the patients' scatter and attenuation properties (43). However, Dewaraja et al. (43), also stated that when comparing I-131 HE quantification results obtained with a spherical (volume: 200.0 ml, diameter: 7.3 cm) and a point source CF, there was no evidence that one geometry outperformed the other.

As with D'Arienzo et al. (20), the relative percentage SD values displayed in Table 4.1 show little difference between the four CF source geometries ( $CF_{\text{cylinder}}$ ,  $CF_{\text{water}}$ ,  $CF_{\text{air}}$  and  $CF_{\text{point}}$ ). However, this small error may not always be representative, as the error is highly dependent on the compensation methods implemented in the clinical reconstruction algorithm. The reconstruction algorithm used in this study includes compensation for object scatter and attenuation as well as CDR which, in turn, compensates partly for collimator septal scatter and penetration. This is not always true for software implemented on clinical workstations.

Our results showed the importance of the choice of VOI size when obtaining a CF. This is especially important when imaging radionuclide-collimator combinations resulting in high levels of septal scatter and penetration, as seen in Figure 4.4a and Figure 4.4c for I-123 LEHR and I-131 HE, respectively. Despite the reconstruction process accounting for septal scatter and penetration, counts from septal scatter and penetration are still present, as evident in the results shown in Table 4.1. The difference in CF when using VOI diameters (ii) and (iii) is 19.0% and 8.4% for I-123 LEHR and I-131 HE, respectively. However, due to the minimal amount of septal scatter and penetration present with I-123 with the ME collimator, the difference in CF values between VOI diameters (ii) and (iii) is less than 2.2%.

The results also show that a less demanding CF source geometry can be used if appropriate corrections for scatter, attenuation and CDR (including septal scatter and penetration) are applied during reconstruction. For this reason, the  $CF_{\text{point}}$  was considered optimal for all radionuclide-collimator combinations, if a VOI diameter equal to the physical size, extended with a radial distance of 3.0 cm as a margin, is used.

### Recovery coefficient curves

According to literature, the shape of the recovery curves is dependent on several factors, including the size and shape of the object, as well as the presence of activity surrounding the object. (60). In this work, only spherical sources, placed in a water-filled cylindrical phantom, were used to determine the RC curves (Figure 4.5) for the three radionuclide-collimator combinations. As a consequence, when applying these RCs as PVE corrections for structures with irregular shapes, the result may be inaccurate (31). It is important to note that the CF source geometry chosen will influence the RCs (27). In this study, the CF was obtained from the  $CF_{\text{point}}$  with a VOI diameter equal to the physical size plus a 3.0 cm margin. However, the VOI diameter used to determine the recovered activity concentration for the RCs was set equal to the sphere's physical size, since this VOI definition was used to obtain the activity quantification accuracy in the voxel-based digital phantoms. This explains why the RC curves do not reach a value of 1, for all radionuclide-collimator combinations. The underestimation of the true activity concentration was more pronounced for I-131 HE due to the collimator's limited spatial resolution (60). Similar results have been reported in literature for I-131, where different VOI geometries were used to obtain RCs and CFs (61).

### Quantification

Figure 4.6 showed absolute quantification errors not more than 3.2% for spheres in an activity-filled cylindrical phantom. The position dependence of VOIs is more pronounced for smaller objects (especially those smaller than two to three times the spatial resolution), which typically results in poorer quantification accuracies. It is important to keep in mind that due to PVEs, smaller objects are generally associated with larger quantification errors (61).

Dewaraja et al. (19) summarised results from physical phantom evaluations of SPECT quantification and highlighted that for I-131 activity quantification without compensation for PVEs, errors of 17.0% for large spheres (8.0 mL to 95.0 mL), and up to 31.0% for small spheres (4.0 mL) (55) were obtained. In another study by Koral et al. (62), I-131 quantification errors of less than 7.0% were reported when compensation for PVE was applied. These results highlight the importance of using appropriate PVE corrections to obtain accurate activity quantification. For I-123 LEHR activity quantification, errors of up to 5.0% were reported by Shcherbinin et al. (23).

In a recent study, Westerberg (61) reported I-131 activity quantification errors up to 13.0% and 8.0% for small (10.0 mL) and large (26.0 mL) spheres, respectively, as well as an activity

quantification error of 35.0% for the kidney when no compensation for PVE was applied. Brady et al. (12) reported I-123 activity quantification errors of 10.0% for spheres with volumes ranging between 5.8 mL and 29.0 mL.

Our study results showed smaller quantification errors in comparison to results in some of the literature findings, as pointed out above, which is most likely attributed to differences in the compensation and reconstruction methods used and the addition of PVE compensation which was often omitted by the referenced authors.

The overestimation noted for the 3.0 cm sphere in patient scenario 2, for I-131 HE is striking; however, results are only shown for a single patient. We therefore speculate that this may be due to statistical variations; however, it is recommended that future work include more patient phantoms.

#### **4.5 Conclusion**

Our results show when using a simple CF source geometry in clinically realistic patient geometries, it is possible to obtain activity quantification accuracies within 6.0% for all radionuclide-collimator combinations if appropriate corrections for scatter, attenuation, CDR and PVEs were incorporated into the reconstruction of the SPECT data. Our results also show that comparable I-123 activity quantification accuracies could be obtained with the LEHR and ME collimators.

The quantification procedure suggested in this study can easily be implemented in routine clinical practice. I-123 imaging should preferably be performed with a ME collimator. However, if appropriate corrections for septal scatter and penetration can be applied, then the I-123 LEHR combination can be useful for departments that do not have access to a ME collimator.

## 4.6 References

1. Frangos S, Buscombe JR. Why should we be concerned about a “g”? *Eur J Nucl Med Mol Imaging*. 2019;46:519. doi: 10.1007/s00259-018-4204-z
2. Yordanova A, Eppard E, Kürpig S, Bundschuh RA, Schönberger S, Gonzalez-Carmona M. Theranostics in nuclear medicine practice. *Onco Targets Ther*. 2017;10:4821–4828. doi:10.2147/ott.s140671
3. Ljungberg M, Gleisner K. Hybrid Imaging for Patient-Specific Dosimetry in Radionuclide Therapy. *Diagnostics*. 2015;5(3):296–317. doi: 10.3390/diagnostics5030296
4. Wieland DM, Wu J, Brown LE, Mangner TJ, Swanson DP. Radiolabeled Adrenergic Neuron-Blocking Agents : Adrenomedullary Imaging with [ I-131 ] Iodobenzylguanidine. *J Nucl Med*. 1980;21(4):349–353. PMID: 7381563.
5. Sjögreen K, Ljungberg M, Strand S, Library PM. An activity quantification method based on registration of CT and whole-body scintillation camera images, with application to I-131. *J Nucl Med*. 2002;43(7):972–982. doi:10.1.1.580.371
6. Silberstein E. Radioiodine : The Classic Theranostic Agent. *Semin Nucl Med*. 2012;42(3):164–170. doi: 10.1053/j.semnuclmed.2011.12.002
7. Jimenez C, Erwin W, Chasen B. Targeted radionuclide therapy for patients with metastatic pheochromocytoma and paraganglioma: From low-specific-activity to high-specific-activity iodine-131 metaiodobenzylguanidine. *Cancers (Basel)*. 2019;11(7). doi: 10.3390/cancers11071018
8. Theerakulpisut D, Raruenrom Y, Wongsurawat N, Somboonporn C. Value of SPECT/CT in Diagnostic I-131 MIBG Scintigraphy in Patients with Neuroblastoma. *Nucl Med Mol Imaging*. 2018;52(5):350–358. doi: 10.1007/s13139-018-0532-y
9. Bombardieri E, Giammarile F, Aktolun C, Baum RP, Bischof Delaloye A, Maffioli L. I-131/I-123-Metaiodobenzylguanidine (mIBG) scintigraphy: Procedure guidelines for tumour imaging. *Eur J Nucl Med Mol Imaging*. 2010;37(12):2436–2446. doi: 10.1007/s00259-003-1357-0
10. Giammarile F, Chiti A, Lassmann M, Brans B, Flux G. EANM procedure guidelines

- for I-131-meta-iodobenzylguanidine (I-131-mIBG) therapy. *Eur J Nucl Med Mol Imaging*. 2008;35(5):1039–1047. doi: 10.1007/s00259-008-0715-3
11. Dewaraja YK, Ljungberg M, Green AJ, Zanzonico PB, Frey EC. MIRD Pamphlet No. 24: Guidelines for Quantitative  $^{131}\text{I}$  SPECT in Dosimetry Applications. *J Nucl Med*. 2013;54(12):2182–2189. doi: 10.2967/jnumed.113.122390
  12. Brady SL, Shulkin BL. Analysis of quantitative [  $^{123}\text{I}$  ] mIBG SPECT / CT in a phantom and in patients with neuroblastoma. *EJNMMI Phys*. 2019;6(31). doi: 10.1186/s40658-019-0267-6
  13. Flotats A, Carrio I. I-131-mIBG and the phantom tollbooth. *J Nucl Cardiol*. 2017;25(3):1198–1200. doi: 10.1007/s12350-017-0843-x
  14. Inoue Y, Shirouzu I, Machida T, Yoshizawa Y, Akita F, Doi I. Physical characteristics of low and medium energy collimators for  $^{123}\text{I}$  imaging and simultaneous dual-radionuclide imaging. *Nucl Med Commun*. 2003;24:1195–1202. doi: 10.1097/00006231-200311000-00011
  15. Dobbeleir AA, Hambj e AE, Franken PR. Influence of high-energy photons on the spectrum of iodine-123 with low- and medium-energy collimators : consequences for imaging with  $^{123}\text{I}$ -labelled compounds in clinical practice. *Eur J Nucl Med*. 1999;26(6):655–658. doi: 10.1007/s002590050434
  16. Rault E, Vandenberghe S, Holen R Van, Beenhouwer J De, Staelens S, Lemahieu I. Comparison of image quality of different iodine radionuclides (I-123 , I-124 , and I-131). *Cancer Biother Radiopharm*. 2007;22(3). doi: 10.1089/cbr.2006.323
  17. Shepp LA, Vardi Y. Maximum likelihood reconstruction for emission tomography. *IEEE Trans Med Imaging*. 1982;1:113–122. doi: 10.1109/TMI.1982.4307558
  18. Lange K, Carson R. EM Reconstruction Algorithms for Emission and Transmission Tomography. *J Comput Assist Tomogr*. 1984;8(2):306–316. doi: PMID: 6608535.
  19. Dewaraja YK, Frey EC, Sgouros G, Brill AB, Roberson P, Zanzonico PB. MIRD pamphlet no. 23: Quantitative SPECT for patient-specific 3-dimensional dosimetry in internal radionuclide therapy. *J Nucl Med*. 2012;53(8):17. doi: 10.2967/jnumed.111.100123

20. D'Arienzo M, Cazzato M, Cozzella ML, Cox M, D'Andrea M, Fazio A. Gamma camera calibration and validation for quantitative SPECT imaging with  $^{177}\text{Lu}$ . *Appl Radiat Isot.* 2016;112:156–164. doi: 10.1016/j.apradiso.2016.03.007
21. Zhao W, Esquinas PL, Hou X, Uribe CF, Gonzalez M, Beaugard J. Determination of gamma camera calibration factors for quantitation of therapeutic radionuclides. *EJNMMI Phys.* 2018;5(8):16. doi: 10.1186/s40658-018-0208-9
22. Ljungberg M, Sjögreen Gleisner K. Personalized Dosimetry for Radionuclide Therapy Using Molecular Imaging Tools. *Biomedicines.* 2016;4(4):25. doi: 10.3390/biomedicines4040025
23. Shcherbinin S, Celler A, Belhocine T, Vanderwerf R, Driedger A. Accuracy of quantitative reconstructions in SPECT / CT imaging. *Phys Med Biol.* 2008;53:4595–4604. doi: 10.1088/0031-9155/53/17/009
24. Willowson K, Bailey D, Baldock C. Quantitative SPECT reconstruction using CT-derived corrections. *Phys Med Biol.* 2008;53(12):3099–3112. doi: 10.1088/0031-9155/53/12/002
25. Cherry SR, Sorenson J, Phelps ME, Methé BM. *Physics in Nuclear Medicine.* 4<sup>th</sup> ed. Philadelphia: Saunders; 2012. 1–544 p.
26. Hoffman E, Huang S, Phelps M. Quantitation in positron emission computed tomography: 1. Effect of object size. *J Comput Assist Tomogr.* 1979;3(3):299–308. doi: 10.1097/00004728-197906000-00001
27. Ramonaheng K, van Staden JA, du Raan H. The Effect of Calibration Factors and Recovery Coefficients on  $^{177}\text{Lu}$  SPECT Activity Quantification Accuracy: A Monte Carlo study. *EJNMMI Phys.* 2021;8:27. doi: 10.1186/s40658-021-00365-8
28. Ritt P, Vija H, Hornegger J, Kuwert T. Absolute quantification in SPECT. *Eur J Nucl Med Mol Imaging.* 2011;38:69–77. doi: 10.1007/s00259-011-1770-8
29. Zeintl J, Vija AH, Yahil A, Hornegger J, Kuwert T. Quantitative Accuracy of Clinical  $^{99\text{m}}\text{Tc}$  SPECT/CT Using Ordered-Subset Expectation Maximization with 3-Dimensional Resolution Recovery, Attenuation, and Scatter Correction. *J Nucl Med.* 2010;51(6):921–928. doi: 10.2967/jnumed.109.071571

30. Dewaraja YK, Ljungberg M, Koral KF. Monte Carlo evaluation of object shape effects in iodine-131 SPET tumor activity quantification. *Eur J Nucl Med*. 2001;28(7):900–906. doi: 10.1007/s002590100551
31. Tran-Gia J, Lassmann M. Optimizing image quantification for Lu-177 SPECT/CT based on a 3D printed 2-compartment kidney phantom. *J Nucl Med*. 2018;59:616–624. doi: 10.2967/jnumed.117.200170
32. Bahreyni Toossi M., Islamian P, Momennezhad M, Ljungberg M, Naseri S. SIMIND Monte Carlo simulation of a single photon emission CT. *J Med Phys*. 2010;35(1):42. doi: 10.4103/0971-6203.55967
33. Ljungberg M, Celler A, Konijnenberg MW, Eckerman KF, Dewaraja YK, Sjögreen-Gleisner K. MIRD pamphlet no. 26: Joint EANM/MIRD guidelines for quantitative <sup>177</sup>Lu SPECT applied for dosimetry of radiopharmaceutical therapy. *J Nucl Med*. 2016;57(1):151–162. doi: 10.2967/jnumed.115.159012
34. Ljungberg M, Strand SE, King MA. The SIMIND Monte Carlo program. *Monte Carlo Calc Nucl Med Appl diagnostic imaging*. 1998;145–163. <https://lup.lub.lu.se/record/3217210>
35. Zaidi H. Relevance of accurate Monte Carlo modeling in nuclear medical imaging. *Med Phys*. 1999;26(February):574–608. doi: 10.1118/1.598559
36. Fahey FH, Grogg K, El Fakhri G. Use of Monte Carlo Techniques in Nuclear Medicine. *J Am Coll Radiol*. 2018;15(3):446–448. doi: 10.1016/j.jacr.2017.09.045
37. Autret D, Bitar A, Ferrer L, Lisbona A, Bardiès M. Monte Carlo modeling of gamma cameras for I-131 imaging in targeted radiotherapy. *Cancer Biother Radiopharm*. 2005;20(1):77–84. doi: 10.1089/cbr.2005.20.77
38. Ljungberg M. Absolute Quantitation of SPECT Studies. *Semin Nucl Med*. 2018;48(4):348–358. doi: 10.1053/j.semnuclmed.2018.02.009
39. Ljungberg M, Strand SE. A Monte Carlo program for the simulation of scintillation camera characteristics. *Comput Methods Programs Biomed*. 1989;29(4):257–72. doi: 10.1016/0169-2607(89)90111-9
40. Knoll GF. *Radiation Detection and Measurement*. 3<sup>rd</sup> ed., John Wiley & Sons. Inc.

2005. 816

41. Morphis M, van Staden JA, du Raan H, Ljungberg M. Modelling of energy-dependent spectral resolution for SPECT Monte Carlo simulations using SIMIND. *Heliyon*. 2021;7:12. doi: 10.1016/j.heliyon.2021.e06097
42. Ejeh J. Accuracy of iodine-131 activity quantification and dosimetry for three-dimensional patient-specific models. 2019. [thesis] University of the Free State, South Africa
43. Dewaraja YK, Wilderman SJ, Ljungberg M, Koral KF, Zasadny K, Kaminiski MS. Accurate dosimetry in I-131 radionuclide therapy using patient-specific, 3-dimensional methods for SPECT reconstruction and absorbed dose calculation. *J Nucl Med*. 2005;46(5):840–849. PMID: 15872359
44. Morphis M, van Staden JA, du Raan H, Ljungberg M. Validation of a SIMIND Monte Carlo modelled gamma camera for Iodine-123 and Iodine-131 imaging. *Heliyon*. 2021;7:11. doi: 10.1016/j.heliyon.2021.e07196
45. Fluke Biomedical. Nuclear Associates 76-823, 76-824 & 76-825 PET/SPECT Phantom Source Tank, Phatom Inserts and Cardiac Insert User Guide. 2005;10.
46. Ramonaheng K, van Staden J, du Raan H. Validation of a Monte Carlo Modelled Gamma Camera for Lutetium-177 Imaging. *Appl Radiat Isot*. 2020;163. doi: 10.1016/j.apradiso.2020.109200
47. Sjögren K, Ljungberg M, Wingårdh K, Minarik D, Strand S-E. The LundADose method for planar image activity quantification and absorbed-dose assessment in radionuclide therapy. *Cancer Biother Radiopharm*. 2005;20(1):92–97. doi: 10.1089/cbr.2005.20.92
48. Frey EC, Tsui BMW. A new method for modeling the spatially-variant, object-dependent scatter response function in SPECT. In: 1996 IEEE Nuclear Science Symposium Conference Record. IEEE; 1996;1082–1086. doi: 10.1109/NSSMIC.1996.591559
49. Ljungberg M, Sjogren K, Liu X, Frey E, Dewaraja Y, Strand SE. A 3-Dimensional Absorbed Dose Calculation Method Based on Quantitative SPECT for Radionuclide



- Therapy : Evaluation for  $^{131}\text{I}$  Using Monte Carlo Simulation. *J Nucl Med.* 2002;43:1101–1109. PMID: 12163637
50. Loening AM, Gambhir SS. AMIDE: A Completely Free System for Medical Imaging Data Analysis. *J Nucl Med.* 2001;42(5):192. doi: 10.1.1.532.9777
  51. Brambilla M, Cannillo B, Dominietto M, Inglese E. Characterization of ordered-subsets expectation maximization with 3D post- reconstruction Gauss filtering and comparison with filtered backprojection. *Ann Nucl Med.* 2005;19(2):75–82. doi: 10.1007/BF03027384
  52. Leong LK, Kruger RL, Connor MKO. A Comparison of the Uniformity Requirements for SPECT Image Reconstruction Using FBP and OSEM Techniques. *J Nucl Med Technol.* 2001;29:79–83. PMID: 11376099
  53. Sjögren K, Ljungberg M, Strand S. Parameters Influencing Volume and Activity Quantitation in Spect. *Acta Oncol (Madr).* 1996;35(4):323–330. doi: 10.3109/02841869609101649
  54. Nakajima K, Verschure DO, Okuda K, Verberne HJ. Standardization of  $^{123}\text{I}$ - meta - iodobenzylguanidine myocardial sympathetic activity imaging : phantom calibration and clinical applications. *Clin Transl Imaging.* 2017;5(3):255–263. doi: 10.1007/s40336-017-0230-2
  55. Dewaraja YK, Koral KF, Fessler JA. Regularized reconstruction in quantitative SPECT using CT side information from hybrid imaging. *Phys Med Biol.* 2010;55:2523–2539. doi: 10.1088/0031-9155/55/9/007
  56. Koral KF, Kritzman JN, Rogers VE, Ackermann RJ, Fessler JA. Optimizing the number of equivalent iterations of 3D OSEM in SPECT reconstruction of I-131 focal activities. *Nucl Instruments Methods Phys Res.* 2007;579(A):326–329. doi: 10.1016/j.nima.2007.04.070
  57. Grassi E, Mezzenga E, Finocchiaro D. Impact of a commercial 3D OSEM reconstruction algorithm on the  $^{177}\text{Lu}$  activity quantification of SPECT / CT imaging in a Molecular Radiotherapy trial. *Radiol Diagnostic Imaging.* 2017;1(1):1–7. doi: 10.15761/RDI.1000101

58. Tran-gia J, Lassmann M. Characterization of Noise and Resolution for Quantitative  $^{177}\text{Lu}$  SPECT/CT with xSPECT Quant. *J Nucl Med*. 2019;60(1):50–59. doi: 10.2967/jnumed.118.211094
59. Niñerola-Baizán A, Gallego J, Cot A, Aguiar P, Lomeña F, Pavía J. Optimization of the reconstruction parameters in [  $^{123}\text{I}$  ] FP-CIT. *Phys Med Biol*. 2018;63:10. doi: 10.1088/1361-6560/aab799
60. Frey EC, Humm JL, Ljungberg M. Accuracy and precision of radioactivity quantification in nuclear medicine images. *Semin Nucl Med* . 2012;42(3):208–218. doi: 10.1053/j.semnuclmed.2011.11.003
61. Westerberg F, Hindorf C, Larsson E, Stenvall A. Quantification of I-131 Activity from Gamma Camera Images of Thyroid Cancer Patients. 2019. [thesis] Lund University, Lund, Sweden
62. Koral KF, Yendiki A, Lin Q, Dewaraja YK. Comparison of 3-D OSEM Versus 1-D SAGE for Focal Total-Activity Quantification in I-131 SPECT With HE Collimation. *IEEE Trans Nucl Sci*. 2005;52(1):154–158. doi: 10.1109/tns.2004.843154

# **Chapter 5: Paper IV**

## **Accuracy of patient-specific I-131 dosimetry using hybrid planar-SPECT/CT I-123 and I-131 imaging**

This paper is a publishable manuscript and is being finalised for submission for publication.

# Table of Contents

5.1	Introduction.....	5.2
5.2	Materials and methods .....	5.6
5.2.1	Monte Carlo simulations .....	5.6
5.2.2	Image processing and activity quantification .....	5.8
5.2.3	Dosimetry .....	5.10
5.3	Results.....	5.13
5.3.1	Whole-body time-activity curves .....	5.13
5.3.2	SPECT activity quantification .....	5.15
5.3.3	Dosimetry .....	5.16
5.4	Discussion .....	5.20
5.5	Conclusion .....	5.21
5.6	References.....	5.23

## 5.1 Introduction

Personalising cancer treatment in the field of oncology is rapidly evolving, highlighting the importance and advantage of radiopharmaceutical therapy (1,2). Theragnostics is a field in nuclear medicine (NM) (3), where radiopharmaceuticals and imaging techniques are uniquely combined to diagnose and treat certain types of cancers sequentially. Typically, the same radiopharmaceutical is used for both the diagnostic imaging and therapy; however, the radionuclide may differ (4,5).

Silberstein (6) considers radioiodine a classic theragnostic agent. Since iodine naturally accumulates in the thyroid, it is routinely used to diagnose thyrotoxicosis and thyroid cancer. Metaiodobenzylguanidine (mIBG) was first used to image tumours in the adrenal medulla as early as 1980. When labelled to iodine-123 (I-123) or iodine-131 (I-131), mIBG has become a standard for the detection and staging of neuroendocrine tumours (NETs) in NM imaging. I-123's principal photon energy (159.0 keV) is better suited and favoured over I-131 (364.0 keV) for imaging. I-123 has a lower radiation load, allowing for administration of higher activity for imaging purposes. As a result, I-123 is an ideal choice for accurate localisation when using SPECT/CT systems. However, I-131 is readily available; therefore, in centres where I-123 is unavailable, I-131 is often used (7,8). I-131 may also be preferred due to its longer half-life, allowing for more accurate determination of its' biological washout (9).

I-123 can be imaged with either a low energy high resolution (LEHR) or a medium energy (ME) collimator. When an improved spatial resolution is required, the LEHR collimator is recommended; however, this is only true when appropriate corrections for septal scatter and penetration are applied, since I-123 emits multiple high energy photons (e.g. 529 keV with 1.4% abundance) (10). The ME collimator reduces the influence of septal scatter and penetration from the higher-energy photons of I-123 and is thus the preferred collimator when accurate activity quantification is required. However, some NM practices may only have access to a LEHR collimator; therefore, it is worthwhile investigating the potential use of the LEHR collimator for I-123 imaging. Due to the relatively high energy of the I-131 main photopeak, together with the septal penetration and scatter from its' higher energy photons (636.9 and 722.9 keV), the use of a high energy (HE) collimator is required (10–12). In addition to the gamma photons emitted by I-131, beta particles with a maximum and mean energy of 606.0 keV and 192.0 keV are also emitted, making I-131 an ideal therapeutic agent. I-131 is

routinely used to treat thyrotoxicosis and thyroid cancer, and when labelled to mIBG, it is used in the treatment of NETs.

Typically, the efficacy of cancer treatment is directly related to the high absorbed dose to the tumours, however, the absorbed dose limits for the organs at risk and the surrounding tissue have to be taken into account (13). Thus, to ensure the safety and optimisation of radiopharmaceutical therapy, knowing the absorbed dose to tumours and organs at risk is critical, especially when evaluating its' radiobiological effect (14). The effectiveness of radiopharmaceutical therapy can therefore be improved with accurate pre-treatment patient-specific dosimetry.

The most widely used method for performing internal radiation dosimetry is the MIRD formalism, proposed by the Medical Internal Radiation Dose Committee of the Society of Nuclear Medicine (15). A practical approach for using this formalism was initially developed for diagnostic dosimetry and risk estimates, using precalculated organ-based tables describing radiation transport. This method is simple but valuable to use in routine practice. Since physical and biological radiopharmaceutical data is easily obtained, the dose to selected organs and the whole-body (WB) can be estimated using the MIRD formalism approach.

An estimated mean absorbed dose to a target volume is calculated, assuming average tissue energy deposition and uniform radiopharmaceutical distribution. For non-penetrating radiation (beta particles and electrons), the source and the target volumes are the same. For penetrating radiation (photons), multiple source volumes may contribute to the absorbed dose in a target volume, including radiation emitted from the target volume itself (16).

The mean absorbed dose to a particular target organ,  $D_{rk}$ , is calculated as follows,

$$\overline{D_{rk}} = \sum_h \widetilde{A}_h S(r_k \leftarrow r_h) \quad (5.1)$$

where  $r_h$  is the source region,  $r_k$  is the target region,  $\widetilde{A}_h$  is the time-integrated activity for each source region, and  $S(r_k \leftarrow r_h)$  is the mean dose per cumulated activity from the source region to the target region.  $S$  values are calculated using Monte Carlo (MC) simulations based on computational models. Tabulated versions are calculated from mathematical reference phantoms of an average adult, adolescent, child, or foetus. Multiple target and source volume  $S$  values for a range of radionuclides have been published in MIRD pamphlet 11 (17, 18)..

Absorbed dose calculations from reference phantoms can be useful for non-patient-specific diagnostic dosimetry and risk estimates. However, it has, in principle, a limited use in therapy, as organ shape, size, and position vary considerably from patient to patient (19). To overcome the shortcomings of the MIRD formalism, an alternative method based on MC radiation transport in a more patient-specific geometry can be adopted.

Absorbed dose calculations from real-time MC radiation transport is the most accurate method for patient-specific 3D absorbed dose calculations; however, it is not well established in the clinic, as it is relatively time-consuming (20). This approach is based on the MIRD formalism, however, the source and target volumes are defined from individual voxels, rather than from mathematical models describing whole organs.

It uses activity images together with registered attenuation maps to model radiation transport in the patient. The process involves sampling decay locations from a set of quantitative NM images, by assuming each voxel value indicates the activity at a specific volume in the patient, corresponding to the voxel location. The transportation of non-penetrating (betas and electrons) and penetrating (photons) radiation is simulated based on the density map created from patient CT images. The energy deposited at each interaction site is mapped on a separate matrix, equal in size to that of the CT image set. This matrix thus indicates the absorbed energy in the patient, on a voxel level.

The accuracy of absorbed dose calculations, based on SPECT images, depends on several factors such as the SPECT systems' spatial resolution, tumour size, organ size and the radiopharmaceuticals' biokinetics. Biokinetic information can be obtained from either planar (static or WB), SPECT/CT or a combination of planar and SPECT/CT images (20). The downfall of using planar imaging is its poor image contrast due to activity in over- and underlying tissues, and the need for precalculated S values. These limitations are overcome in tomographic SPECT imaging, allowing for improved quantification accuracy. However, a potential drawback of SPECT imaging for quantification purposes may be its limited axial range of imaging. To perform SPECT imaging over several bed positions, covering a larger anatomical region, would be impractical, as SPECT acquisitions can be time consuming. Due to the large patient load observed in most NM clinics, performing multiple SPECT/CT studies per patient could be challenging. By using a combination of WB planar and SPECT/CT imaging, one can take advantage of the effectiveness and speed of WB planar imaging with the improved quantification accuracy of SPECT/CT imaging (5). The hybrid method of imaging

may be beneficial in institutions with large patient throughput, providing quantification accuracies comparable to that for SPECT/CT, but with the speed of WB planar imaging.

The hybrid method involves acquiring multiple WB planar images over a period at specific timepoints. The geometric-mean (GM) of the anterior and posterior WB planar images are calculated, and corrections for scatter and attenuation are applied. A single SPECT/CT study is performed close in time to one of the WB planar acquisition timepoints. The construction of a time-activity curve (TAC) relies on information obtained from regions-of-interest (ROIs) delineated on the corrected planar images and will therefore represent the kinetic data of the radiopharmaceutical. A scaling factor, which is defined as the ratio between the activity determined from the single SPECT point and its corresponding WB study, is determined. The TAC is then scaled by this ratio, for specific volumes of interest (VOIs), ultimately adjusting the amplitude of the WB planar TAC (5). The assumption is that the activity obtained from SPECT/CT data is more accurate than data obtained from WB planar images.

Undoubtedly, the accuracy of the hybrid method relies on the SPECT activity quantification accuracy. SPECT quantification accuracy depends on many factors; namely, calibration of the camera, the radionuclide-collimator combination as well as the corrections applied for degrading factors which is incorporated into the reconstruction algorithm. These corrections include object scatter, non-homogenous attenuation and collimator detector response (CDR) as well as collimator-septal scatter and septal penetration (20,21).

Studies have shown that the hybrid method of imaging for dosimetry performs better than planar-based methods and can be comparable to SPECT/CT methods (22). For the hybrid method to be successful, three factors should be considered prior to performing hybrid WB planar-SPECT/CT quantification on patients: (i) there should be minimal overlap between ROIs with high activity uptake in the WB planar images, (ii) the volume, represented by the ROI, should be included in the SPECT/CT field-of-view, and (iii) the ROI uptake and boundaries should be clearly visible on the WB planar image (22). If these criteria are met, this method of quantification can be performed with great success.

It is important to note that commercially available dosimetry software, such as OLINDA, often treat tumours as isolated objects, not including cross-dose to and from other tumours and source organs. This may result in significant tumour absorbed dose underestimation. As a result, it



may be worthwhile investigating the relative contribution of photon and beta interactions on the calculated absorbed dose.

This study aimed to assess the accuracy of patient-specific absorbed dose calculations, based on hybrid WB planar-SPECT/CT imaging, for tumours and organs at risk. The study made use of I-123 and I-131 MC simulated voxel-based digital patient phantoms, from which the SPECT activity quantification accuracy was determined. Thereafter, the hybrid WB planar-SPECT/CT method was used to assess the accuracy of the liver and tumour absorbed doses (considering both photon and beta interactions, as well as beta interactions only) for I-131-mIBG radiopharmaceutical therapy.

## **5.2 Materials and methods**

### **5.2.1 Monte Carlo simulations**

The accuracy of the patient-specific dosimetry was assessed based on MC simulations of voxel-based digital patient phantoms, created from CT images of three randomly selected retrospective patient SPECT/CT data sets from the Universitas Academic Hospital NM patient database (#1-3). The process of creating these voxel-based digital phantoms is described by Morphis et al. (23,24).

Two different sized spheres mimicking spherical tumours were added to the voxel-based digital patient phantoms. As shown in Figure 5.1, two scenarios for each patient phantom were created; scenario 1 included a sphere with a diameter of 5.0 cm (65.5 ml) positioned above the liver between the lungs and a second sphere with a diameter of 3.0 cm (14.1 ml) positioned below the liver. Scenario 2 included a 3.0 cm diameter sphere positioned above the liver between the lungs and a 5.0 cm diameter sphere positioned below the liver.

The activity concentration in the liver, lungs, spheres, and remainder of the body was uniformly assigned according to the biological pharmacokinetic data in Table 5.1. The activity concentration values are based on clinical diagnostic I-123 and I-131 mIBG SPECT patient data, with an administered activity of 370.0 MBq and 185.0 MBq for I-123 and I-131, respectively.

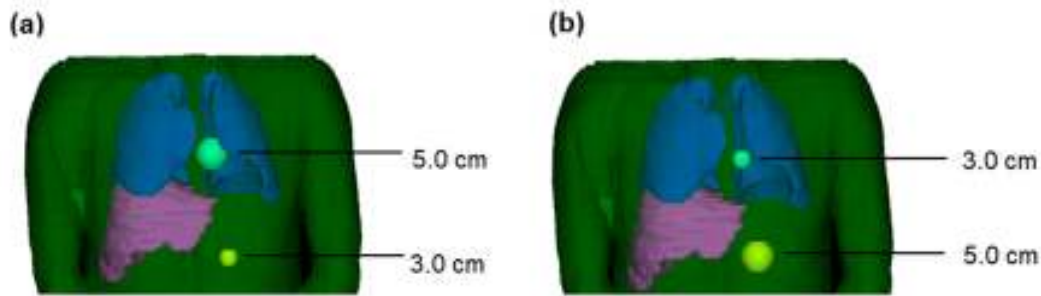


**Figure 5.1.** Schematic showing the position of the spheres for (a) scenario 1 and (b) scenario 2.

**Table 5.1**

**Biological pharmacokinetic data determined from mono-exponential fitting of quantified activity values obtained from WB images at different timepoints post-injection.**

Timepoint (hours p.i.)	Biological Pharmacokinetic Data (kBq/ml)			
	Liver	Lungs	Spheres	Remainder
1	27.9	15.5	342.3	3.4
4	26.2	14.1	325.2	3.2
6	25.1	13.3	314.2	3.1
24	17.2	7.6	231.0	2.3
36	13.3	5.2	188.2	1.8
48	10.4	3.6	153.3	1.5
72	6.2	1.7	101.7	1.0

The SIMIND MC code (25), modelling the dual-head Siemens Symbia T16 (Siemens Healthcare, Erlangen, Germany) SPECT/CT system, used at the Department of NM at Universitas Academic Hospital (Bloemfontein, South Africa), was used to simulate anterior and posterior (A/P) WB planar (from here on referred to as WB) and SPECT projection images for three radionuclide-collimator combinations (I-123 LEHR, I-123 ME and I-131 HE). Morphis et al. (23,24) described the setup and validation of the virtual gamma camera (detector and collimators) and the simulation specifications.

WB planar images were simulated at five timepoints corresponding to 1, 4, 6, 24 and 36 hours p.i. for I-123 and 6, 24, 36, 48 and 72 hours p.i. for I-131. SPECT projections were simulated at 24 hours p.i. for both I-123 and I-131. Effective half-life (biological pharmacokinetic data

shown in Table 5.1 combined with physical decay) was used to generate activity distributions at the different timepoints.

WB planar images were simulated with an image matrix and pixel size of  $256 \times 1024$  and  $2.4 \times 2.4 \text{ mm}^2$ , respectively. The count level in the WB images were scaled to match an acquisition with a scan speed of 6.0 cm/min and a scan length of 2.0 m. Sixty SPECT projections, scaled to match an acquisition time of 40 sec, with a matrix and pixel size of  $128 \times 128$  and  $4.8 \times 4.8 \text{ mm}^2$ , respectively, were simulated in step-and-shoot mode using a non-circular orbit-of-rotation. An energy window of 15.0% was centred over the 159.0 keV and 364.0 keV photopeak's of I-123 and I-131, respectively. The simulation protocols are described in more detail in recent publications by Morphis et al. (23,24). A sufficient number of histories were simulated, to ensure essentially noise-free MC data (19).

### **5.2.2 Image processing and activity quantification**

The simulated WB images were processed with LundADose; a software program developed at Lund University, Sweden (26). The software performs scatter correction on individual A/P WB planar images by applying a Wiener filter deconvolution in Fourier space. The scatter kernels used by the Wiener filter were pre-calculated by MC simulations of a point source at different depths in a water phantom. These simulations incorporated both scatter in the phantom, backscatter, as well as collimator scatter and septal penetration (20). The WB planar images were corrected for attenuation by multiplying the GM image with a patient-specific map of attenuation correction factors, created from a projection of the patient CT dataset (Figure 5.2a), scaled to match the attenuation of 159.0 keV and 364.0 keV, respectively (20). The GM scatter and attenuation corrected WB planar images were not converted to activity images, as they were only used to obtain the shape of the TAC. Despite this, both scatter and attenuation correction was performed as it results in images with improved image quality, making organ and tumour delineation more accurate (20). Since the WB images were solely utilised to determine the shape of the TAC curve, regions of interest (ROIs) smaller than physical size of the source volume, but sufficiently large to ensure good count statistics, were drawn. Smaller ROIs were selected to limit the contribution of over- and underlying activity from other source organs. TACs were generated for the liver and the two spheres, by plotting the count values obtained in each ROI as a function of time.

The SPECT projection images were reconstructed using an OS-EM iterative reconstruction package developed by Frey and Tsui (21), which is incorporated in LundADose. The iterative reconstruction algorithm performs a CT-based attenuation correction, model-based scatter correction using the Effective Scatter Source Estimation algorithm (ESSE), and a CDR correction. The CDR correction accounts for both collimator septal penetration and scatter using pre-calculated MC simulated kernels (27). No postfiltering was performed. Figure 5.2b shows an example of a transverse slice through a CT-based patient-specific attenuation map. Reconstruction was performed with a pre-determined number of OSEM updates (28), resulting in reconstructed SPECT images with a matrix dimensions of 128 and a cubic voxel size of 4.8 mm<sup>3</sup>. The reconstructed images were converted to units of activity using a pre-determined calibration factor of a point source in air, as described by Morphis et al. (28). VOIs were manually delineated to represent the physical size of the liver and the two spheres. The activity in each sphere was corrected for partial volume effect by applying recovery coefficients, obtained from pre-determined recovery curves (28), to the VOIs delineating the spheres' physical size. The recovery coefficients were selected based on spheres of equivalent volume to the delineated VOI. The activity quantification procedure was based on methods described by Morphis et al. (28). The error in the calculated activity for the liver and the two spheres was defined, according to Equation 5.2, as the percentage difference between the recovered activity concentration ( $[A]_{recovered}$ ) and the true activity concentration ( $[A]_{true}$ ), as defined in the SIMIND simulation setup,

$$Quantification\ Error\ (\%) = \frac{[A]_{recovered} - [A]_{true}}{[A]_{true}} \times 100 \quad (5.2)$$

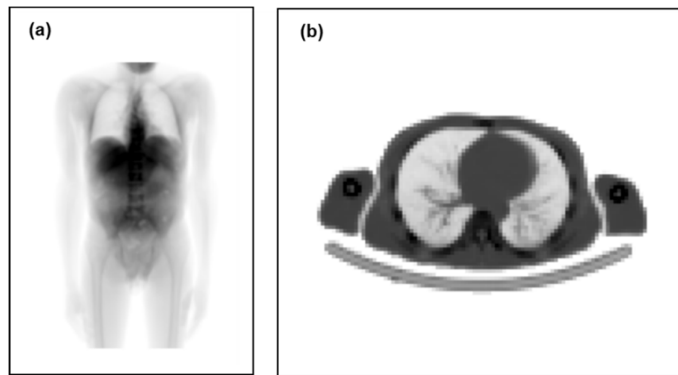


**Figure 5.2.** Example of a patient-specific (a) simulated WB planar image and (b) transverse slice through a CT-based SPECT attenuation map.

### 5.2.3 Dosimetry

Patient phantom-specific dosimetry was performed using full MC radiation transport, based on electron gamma shower (EGSnrc) software, incorporated in LundADose (26). To model the radiation transport, the EGSnrc code employs the physics of both photon and charged-particle interactions with matter. The MC simulations used CT data, incorporating patient phantom anatomical information, as well as the quantitative activity distribution, obtained from the reconstructed SPECT data. The cut-off energy of photon and electron interactions was set to 0.01 and 0.1 MeV, respectively. Two dosimetry simulations were performed, namely, (i) with both photon and beta interactions, and (ii) with beta particle interactions only. All simulations were performed with 100 million histories.

For each patient phantom scenario, two sets of images that defined the quantified SPECT activity distribution (I-123 LEHR, I-123 ME and I-131 HE), were used as input for the MC dose simulations, together with their corresponding registered density image. These were (i) the simulated quantified SPECT activity distribution (QAD) from the patient phantom, post-reconstruction, and (ii) the simulated quantified SPECT activity distribution from the patient phantom, uniformly distributed ( $QAD_u$ ) (depicted in Figure 5.3, step 4).  $QAD_u$  is the apparent image set to use; however, it is well known that when CDR correction is included in the iterative reconstruction, Gibbs artefacts may be present (29). These artefacts are characterised by an increased count level close to the edges of an object and a corresponding lower count level in the centre (20). Ultimately, this phenomenon may affect the accuracy of the calculated absorbed dose. For this reason and since the activity distribution for each VOI, used as input for the simulations, was uniformly defined,  $QAD_u$ , where the quantified activity in each activity was uniformly distributed, was created. The total quantified activity in each organ remained the same, however, spreadout uniformly in  $QAD_u$  to avoid the Gibbs artefact. The LundADose output images represented I-131 absorbed dose-rates, at 24 hours p.i., in units of mGy/hour.

A time dose-rate curve (TDC) was created for each VOI by scaling the TAC, obtained from the five WB planar timepoints, with the absorbed dose-rate calculated from the SPECT timepoint at 24-hour p.i. The time point for the liver and each sphere were fit with a mono-exponential curve-fitting model. The mean absorbed doses for each VOI, for each patient phantom scenario, were calculated by analytical integration from zero to infinity.

The accuracy of the mean absorbed dose was assessed by comparing the absorbed dose calculated from the two sets of images described above to that from the true absorbed dose estimates that were calculated directly from the predefined voxel-based digital patient phantom activity. The absorbed dose accuracy (%) was reported for the liver and both spheres according to Equation 5.3,

$$\text{Absorbed dose accuracy (\%)} = \frac{D_{\text{calculated}} - D_{\text{true}}}{D_{\text{true}}} \times 100 \quad (5.3)$$

Average absorbed dose values to the liver as well as the 3.0 cm and 5.0 cm spheres, across all three patient phantoms and for both scenarios were calculated, considering (i) beta-particle interactions only, as well as (ii) both photon and beta-particle interactions. The schematic flowchart shown in Figure 5.3 illustrates the various steps involved in the dosimetry process.

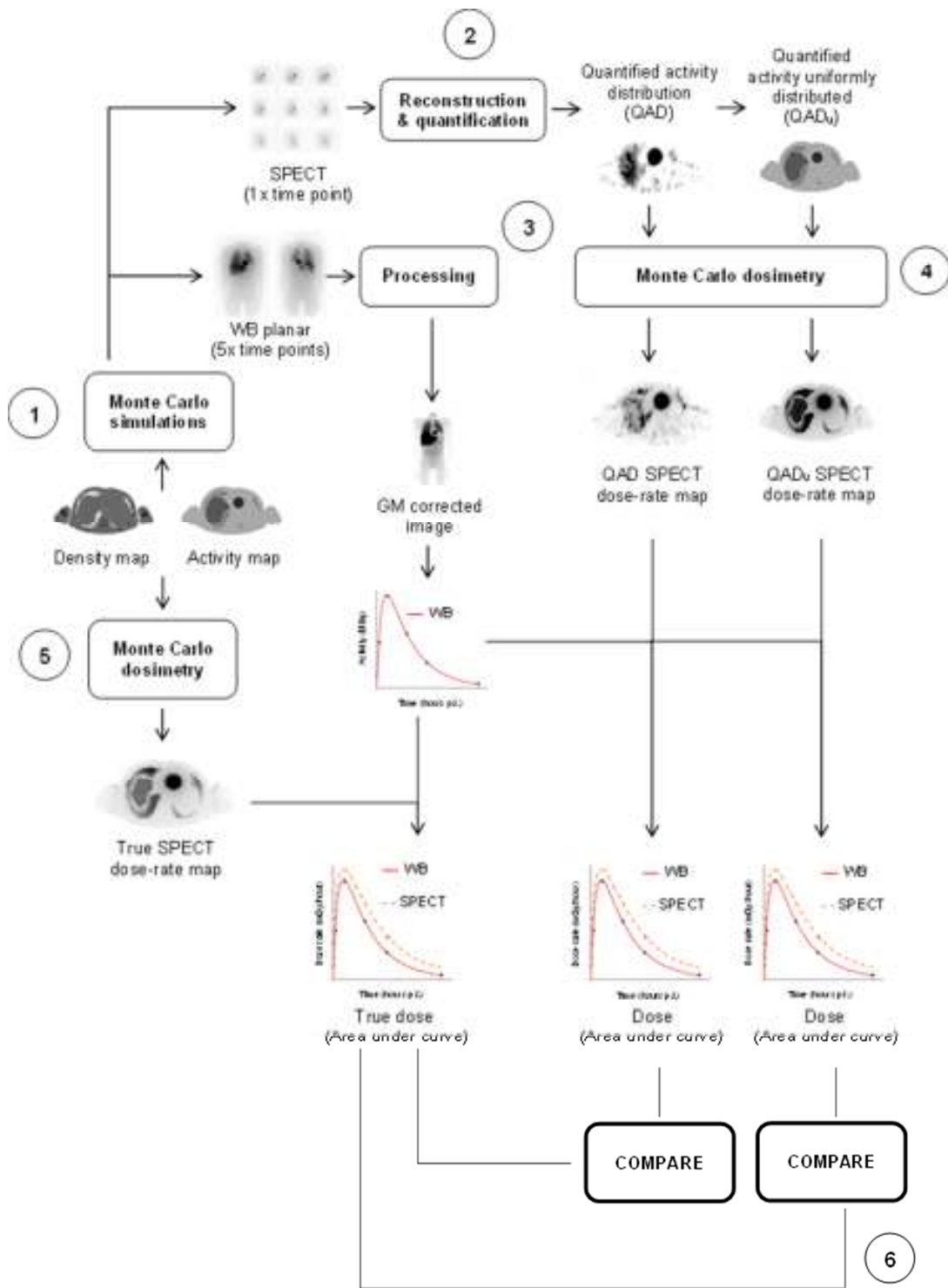


**Figure 5.3.** Schematic flowchart illustrating the various steps involved in the dosimetry process. In step [1] SPECT and WB planar images are simulated using the density and activity maps as input for the MC simulator. [2] The SPECT projection images are reconstructed and the activity in each ROI is quantified. [3] The WB planar images are

processed. In step [4] MC dosimetry is performed for both QAD and QAD<sub>u</sub>. [5] MC dosimetry is then performed on the true activity map to obtain the true dose distribution. In step [6] the calculated dose from QAD and QAD<sub>u</sub> is compared to the true dose, for the liver, 3.0 cm, and 5.0 cm sphere.

## **5.3 Results**

### **5.3.1 Whole-body time-activity curves**

Figure 5.4 shows an example of the unprocessed simulated A/P WB images, as well as the GM corrected image for the three radionuclide-collimator combinations. The ROIs used to create the TACs are also shown in Figure 5.4.

Overall, the WB planar A/P I-123 ME images show better image contrast compared to the I-123 LEHR and I-131 HE images. This can be attributed to the effects of collimator septal scatter and penetration, which is more pronounced for I-123 LEHR and I-131 HE compared to I-123 ME. Therefore, the resultant GM images are noisier after applying scatter correction. Furthermore, based on the lower administered activity and I-131 HE sensitivity, as reported by Morphis et al. (24), the I-131 HE images present with more noise. The GM corrected images show an improvement in image contrast across all three radionuclide-collimator combinations.



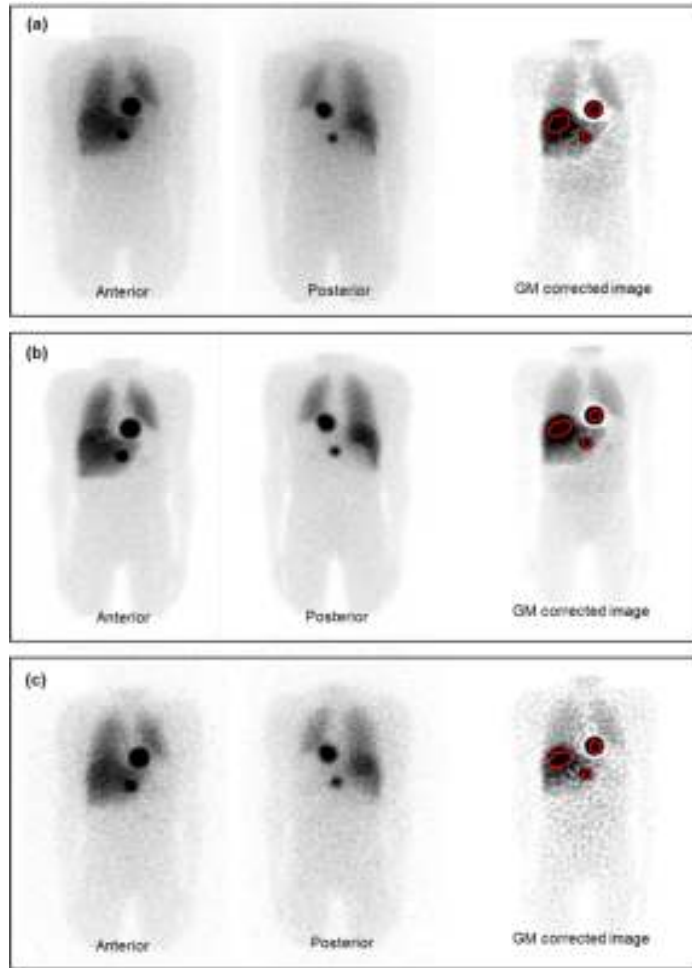


**Figure 5.4.** Example of a simulated anterior and posterior WB planar study and the corresponding GM corrected image for (a) I-123 LEHR, (b) I-123 ME, and (c) I-131 HE.

The fitted TAC for the liver, obtained from the WB planar images at different timepoints, is shown in Figure 5.5 for all three radionuclide-collimator combinations.

Overall, there is a good agreement in the shape of the liver TACs for I-123 LEHR and I-123 ME (Figure 5.5a and b). Due to its longer physical half-life and lower activity concentration, the shape of the I-131 HE TAC shows a more prolonged washout from the liver as well as reduced activity, compared to I-123.

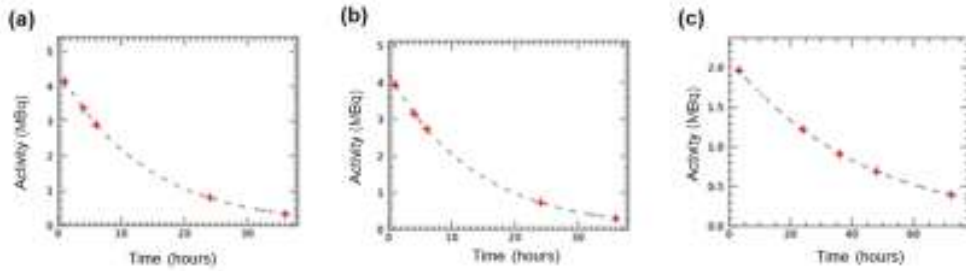


**Figure 5.5.** A plot of activity in the liver ROI as a function of time, predicting the shape of the liver TDC, for (a) I-123 LEHR, (b) I-123 ME and (c) I-131 HE.

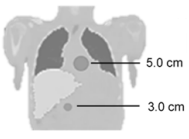
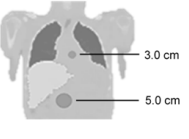
### 5.3.2 SPECT activity quantification

The results in Table 5.2 show a good agreement between the recovered and true activity concentrations for the liver and both spheres in both scenarios for all three patient phantoms. The activity quantification errors, defined by Equation 5.2, for the liver, 3.0 cm and 5.0 cm spheres, for the three radionuclide-collimator combinations, are shown in Table 5.2 below.

The largest quantification errors noted were -5.0% (#1, scenario 1), -6.2% (#2, scenario 2), and -6.9% (#2, scenario 1), for the liver, 3.0 cm and 5.0 cm sphere, respectively. The average quantification errors did not exceed -0.8%, -2.4% and -2.4% for the liver, 3.0 cm sphere and 5.0 cm sphere, respectively.

**Table 5.2**

**Activity quantification error (%) for the liver, 3.0 cm and 5.0 cm sphere, in both scenarios for patients #1-3.**

		Activity Quantification Error (%)								
		Liver			3.0 cm			5.0 cm		
		I-123	I-123	I-131	I-123	I-123	I-131	I-123	I-123	I-131
		LEHR	ME	HE	LEHR	ME	HE	LEHR	ME	HE
Scenario 1 	# 1	-5.0	1.9	-0.8	-4.1	-2.0	-3.8	-4.1	-3.1	-2.6
	# 2	2.7	-2.1	-3.1	1.5	3.4	1.2	-6.9	-6.0	-5.0
	# 3	4.5	1.9	1.8	0.1	0.0	4.8	-3.7	-1.5	-2.3
Scenario 2 	# 1	-3.5	-3.8	-2.1	-3.0	-0.9	5.4	0.3	1.6	-0.5
	# 2	-2.6	-0.3	2.1	-6.2	-5.8	-1.1	2.2	3.2	2.3
	# 3	3.2	1.1	-2.4	-2.8	-3.4	-1.1	-2.0	1.2	0.7
AVG		-0.1	-0.2	-0.8	-2.4	-1.5	0.9	-2.4	-0.8	-1.2
STDEV		4.0	2.3	2.2	2.8	3.1	3.6	3.3	3.4	2.6

### 5.3.3 Dosimetry

Transverse slices through the I-123 LEHR SPECT activity distribution and the corresponding I-131 dose-rate maps are shown in Figure 5.6, for (a) the true activity distribution, (b) QAD, and (c) QAD<sub>u</sub>. The liver and 5 cm sphere VOIs, as delineated on the CT images, are also shown.

Figure 5.6a shows the true dose-rate map, derived from the true uniform activity distribution. The image degrading effects due to the acquisition and processing of NM images are visible in the non-uniform activity distribution in Figure 5.6b. The inserted image of the sphere in Figure 5.6b shows the presence of the Gibbs artefact, post-reconstruction. The noisy activity distribution resulted in an equally noisy dose-rate map, which does not compare well to the true dose-rate map in Figure 5.6a. Using the quantified activity obtained from Figure 5.6b to create an activity map with uniformly distributed activity in each VOI (Figure 5.6c), a dose-rate map that visually compares well with the true dose-rate map is obtained.

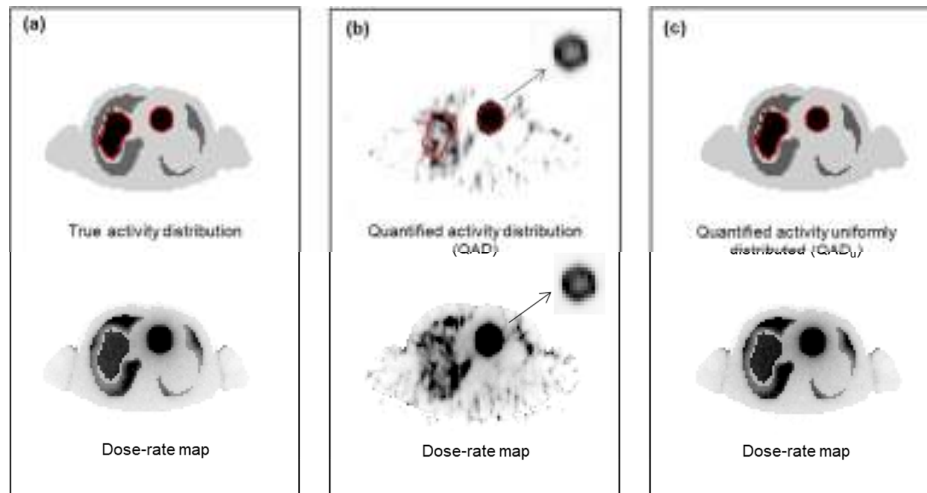


**Figure 5.6.** Slices through I-123 LEHR activity maps and corresponding I-131 dose-rate maps (photon and beta interactions), for (a) true activity distribution, (b) QAD, and (c) QAD<sub>u</sub>. In frame (b), the arrows indicate the presence of the Gibbs artefact in the sphere when viewed at an adjusted contrast level. This could be misinterpreted as necrosis.

Figure 5.7 shows the I-131 absorbed dose values, averaged over all three patient phantoms and both scenarios, with contributions from photon and beta interactions as well as beta interactions only, for the liver, 3.0 cm, and 5.0 cm spheres, calculated from the I-123 LEHR, I-123 ME and I-131 HE activity distributions.

For I-123 ME and I-131 HE, small differences can be seen when comparing the true and calculated absorbed dose values obtained from QAD and QAD<sub>u</sub>, for the liver ( $\leq 6.5\%$ ) and 3.0 cm sphere ( $\leq 4.9\%$ ). Similar differences ( $\leq 13.5\%$ ) were seen for the 5.0 cm sphere.

For I-123 LEHR, the absorbed doses obtained from QAD<sub>u</sub> closer resembled that of the true absorbed dose, with differences  $\leq 5.9\%$ . QAD overestimated the true absorbed dose, with percentage differences up to 20.3%. This overestimation can be attributed to the more pronounced effects of septal scatter and penetration for I-123 LEHR, despite partial correction thereof, contributing to the absorbed dose.

QAD tends to overestimate the true absorbed dose in scenarios where the Gibbs artefact is more prominent (e.g., 5.0 cm sphere). This can be attributed to the fact that PVE correction is applied to the activity within the VOI which delineates the objects' physical size. Therefore, for QAD, although the quantified activity within the VOI is corrected for PVE, activity that has spilled out and lies outside the VOI, still deposits energy within the VOI. The same applies to scattered

photons, or those which have penetrated the collimator septa. The effects thereof are eliminated by using QAD<sub>u</sub>, as all the recovered activity is placed within the VOI (no spill-out activity is present in the activity distribution images).

The results, shown in Figure 5.7a and Table 5.3, show that the absorbed dose to the liver is predominantly due to beta contribution, with photons contributing 34.5% and 30.2%, QAD and QAD<sub>u</sub>, respectively. In comparison, the photon contribution is far less for the 3.0 cm (10.1% and 8.3%) and 5.0 cm (13.3% and 12.6%) spheres. When considering the relatively large liver size, one can expect that more photons are absorbed within the liver volume, whereas photons originating from the spheres are more likely to escape the sphere volume before depositing dose. Furthermore, cross-dose from the liver to the spheres, and vice-versa may also play a role. Since the spheres were allocated a higher activity concentration compared to the liver, a larger contribution of photon cross-dose from the spheres to the liver can be expected, compared to that from the liver to the spheres.

The results in Figure 5.7 are summarised in Table 5.3, which shows the average absorbed dose values, across all radionuclide-collimator combinations and patient phantom scenarios, for the liver, 3.0 cm, and 5.0 cm spheres. Overall, the results show an increased absorbed dose when using QAD compared to that of QAD<sub>u</sub>, for the 3.0 cm and 5.0 cm spheres. Similar liver absorbed dose values were obtained between the two image sets. The relatively small standard deviations highlight the minor differences in dose values across all three radionuclide-collimator combinations.

**Table 5.3**

**Average absorbed dose values across all radionuclide-collimator combinations and patient phantom scenarios for the liver, 3.0 cm and 5.0 cm sphere**

	* Absorbed dose (mGy/MBq)			
	Photon and beta		Beta	
	QAD	QAD <sub>u</sub>	QAD	QAD <sub>u</sub>
Liver	2.1 ± 0.2	2.0 ± 0.1	1.4 ± 0.1	1.4 ± 0.1
3.0 cm	21.1 ± 2.3	19.0 ± 0.1	18.9 ± 2.1	17.5 ± 0.1
5.0 cm	24.2 ± 0.6	20.9 ± 0.6	21.1 ± 0.7	18.2 ± 0.5

\* Absorbed dose ± one standard deviation.

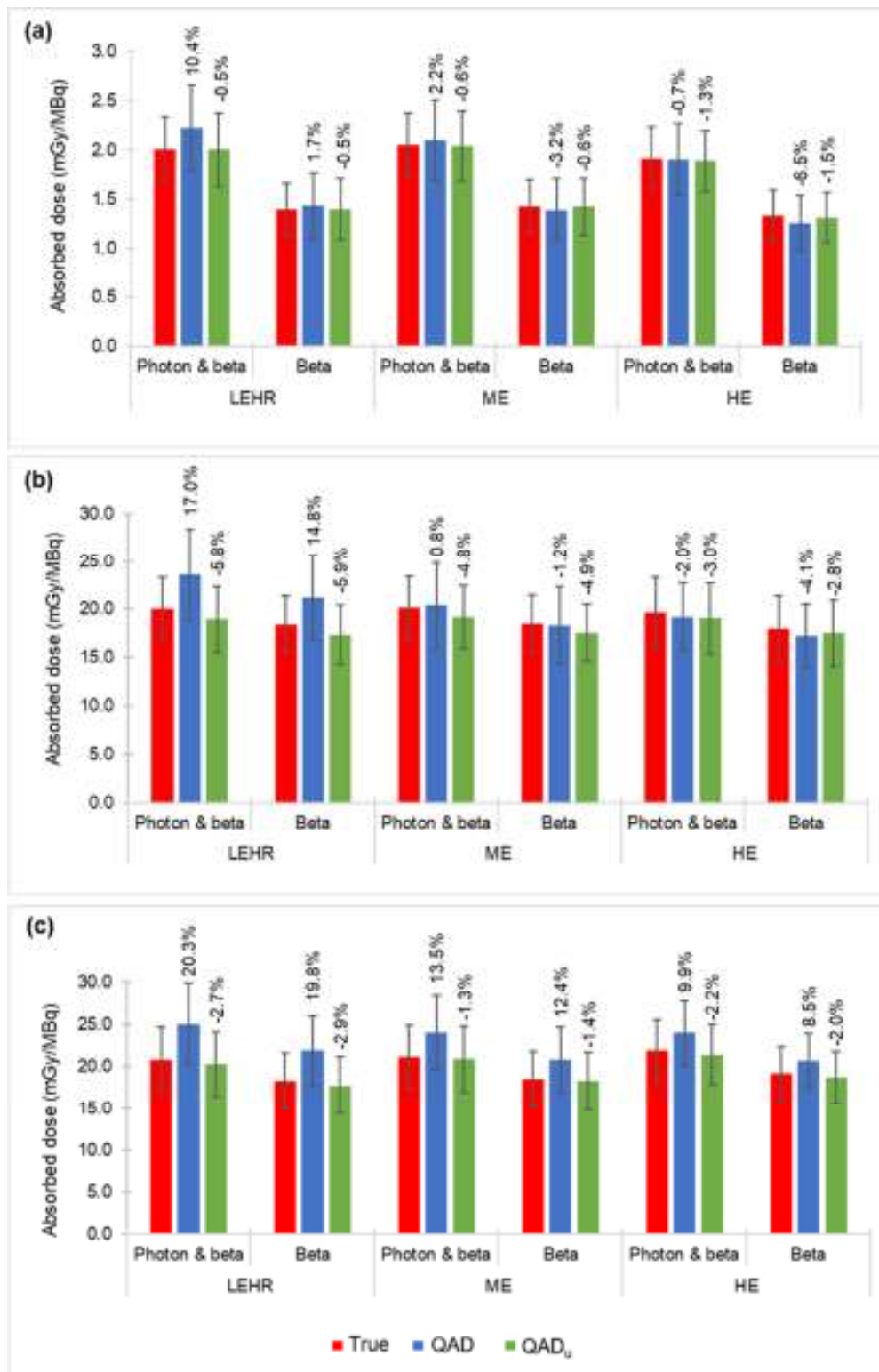


**Figure 5.7.** I-131 absorbed dose values calculated from the true activity distribution and QAD and QAD<sub>u</sub>, for the (a) liver, (b) 3.0 cm sphere, and (c) 5.0 cm sphere, averaged over the three patient phantoms and both scenarios, for all radionuclide-collimator combinations.

Absorbed dose values reported for photon and beta interactions as well as beta only interactions. The value above each bar shows the percentage difference between it and the true absorbed dose. The error bars represent a single standard deviation of the average absorbed dose values.

#### 5.4 Discussion

The assessment of radiopharmaceutical therapy planning requires precise dosimetry. Ljungberg et al. (27) used voxel-based digital phantoms, in conjunction with MC simulations, to determine possible sources of error in the quantification process, allowing for the evaluation of absorbed dose distributions. The proposed method in this study provides a similar evaluation procedure for determining the accuracy of absorbed dose in clinically realistic voxel-based digital patient phantoms.

It is important to note that activity uptake is relatively uniform for normal liver and sphere diameters up to 10.0 cm. However, larger sphere volumes may exhibit non-uniform uptake, due to possible necrotic centres. This may influence the accuracy of the treatment planning, as well as the efficacy of the treatment (9).

The results showed that QAD resulted in an overestimation of the dosimetry results, up to 20.3% (5.0 cm sphere I-123 LEHR). As mentioned, this may be attributed to the partial volume correction by a recovery coefficient, which was applied to the VOI activity, correcting the activity in the VOI for spill-out counts. The spill-out counts as well as those from septal scatter and penetration outside the VOI are not removed from the image, thus still contribute to the absorbed dose in the VOI. In a study by Dewaraja et al. (19) it was noted that when I-131 SPECT activity quantification was underestimated, the I-131 absorbed dose was also underestimated, but to a lesser extent. They stated that this could be attributed to the spill-out of counts which did not contribute to the VOI activity but did contribute to its absorbed dose.

To overcome this problem and considering the known activity distribution was uniform, the reconstructed activity distribution was replaced with a uniform distribution of the quantified activity ( $QAD_u$ ), resulting in dosimetry accuracies within 5.9%. Overall, absorbed dose values obtained with  $QAD_u$  had improved accuracy, due to the removal of spill-out activity.

A wide range of I-131-mIBG liver absorbed doses have been reported in literature, with values ranging from 0.3 to 1.1 mGy/MBq (1,30–33) and others ranging from 2.0 to 5.5 mGy/MBq

(19,27,34). The absorbed dose values (photon and beta interactions) of  $2.1 \pm 0.2$  mGy/MBq (QAD) and  $2.0 \pm 0.1$  mGy/MBq (QAD<sub>u</sub>) obtained in this study fall well within these reported values. It is important to note that the absorbed dose values for beta interactions only resulted in values up to 30.0% less than when photon and beta interactions were considered. In this case, local photon absorption is not considered and the cross-dose from spheres is significantly underestimated. Quantitative Analyses of Normal Tissue Effects in the Clinic (QUANTEC) states that for external beam radiation therapy, liver absorbed doses should not exceed 30.0 Gy, ensuring toxicity of less than 5.0% (35). However, considering I-131-mIBG therapy has a lower dose-rate, than that of external beam, the detrimental effect of radiation may be mitigated, allowing for a higher dose limit for I-131-mIBG therapy (1).

I-131-mIBG tumour absorbed doses ranging between 0.2 and 17.0 mGy/MBq have been reported in literature (19,30,31). Sphere absorbed dose values (photon and beta interactions) reported in Figure 5.7 varied between 18.9 mGy/MBq and 25.1 mGy/MBq. When only beta interactions were considered, absorbed doses were as much as 12.0% lower. This indicates that the assumption made by commercial software, such as OLINDA, which treat tumours as isolated objects, not including cross-dose to and from other tumours and organs at risk, may result in significant dose underestimation. Similar findings were reported by Grimes et al. (36).

## 5.5 Conclusion

Tumour dosimetry can be used to measure the efficacy of a treatment, whilst organ dosimetry can be used as a measure of treatment toxicity. Although the simulation studies were clinically realistic it is important to note that organ and sphere motion was not considered, which could affect the accuracy of activity quantification and absorbed dose in an actual clinical scenario.

The hybrid planar-SPECT/CT method for dosimetry has proven effective for personalised treatment planning of I-131 radiopharmaceutical therapy, with either I-123 or I-131 imaging. Highly accurate dosimetry can be obtained for the liver and spheres as small as 3.0 cm. Despite the poorer I-123 LEHR and I-131 HE image quality, acceptable quantification accuracy was obtained. I-131 absorbed dose values obtained from I-123 and I-131 images were comparable. The average liver and sphere absorbed doses for the three patient phantoms with the proposed uniformly distributed quantified activity (QAD<sub>u</sub>) were more accurate than that from the quantified reconstructed activity distribution (QAD).



The novel approach of replacing the reconstructed activity distribution with a uniform activity distribution based on the quantified activity, results in a calculated absorbed dose that more closely resembles the true absorbed dose value. As mentioned, this is an acceptable approach when applying partial volume correction using the standard recovery coefficient method. This approach may be of use in situations where there are pronounced Gibbs artefacts, due to CDR correction, as well as scenarios where radionuclide-collimator combinations result in high levels of septal scatter and penetration, which cannot completely be corrected. It may also be worth investigating how voxel-based partial volume correction will influence the quantitative and absorbed dose accuracy when using QAD.

The question arises as to whether accurate organ and tumour absorbed dose values can be obtained when a uniform activity distribution is assumed in cases with a non-uniform initial activity distribution. This will be investigated in future work, expanding on this study.

## 5.6 References

1. Chiesa C, Castellani R, Mira M, Lorenzoni A, Flux G. Dosimetry for <sup>131</sup>I mIBG Therapy: moving towards personalized medicine. *Q J Nucl Med Mol imaging*. 2013;57(2):161–70. PMID: 23822991
2. Wahl RL, Ahuja S. Current Landscape of Radiopharmaceutical Therapies : SNMMI Therapy Task Force Survey. *J Nucl Med*. 2021;62(5):11–6. PMID: 33975977
3. Frangos S, Buscombe JR. Why should we be concerned about a “g”? *Eur J Nucl Med Mol Imaging*. 2019;46:519. doi: 10.1007/s00259-018-4204-z
4. Yordanova A, Eppard E, Kürpig S, Bundschuh RA, Schönberger S, Gonzalez-Carmona M, et al. Theranostics in nuclear medicine practice. *Onco Targets Ther*. 2017;10:4821–8. doi: 10.2147/OTT.S140671
5. Ljungberg M, Gleisner K. Hybrid Imaging for Patient-Specific Dosimetry in Radionuclide Therapy. *Diagnostics*. 2015;5(3):296–317. doi: 10.3390/diagnostics5030296.
6. Silberstein E. Radioiodine : The Classic Theranostic Agent. *Semin Nucl Med*. 2012;42(3):164–70. doi: 10.1053/j.semnuclmed.2011.12.002
7. Jimenez C, Erwin W, Chasen B. Targeted radionuclide therapy for patients with metastatic pheochromocytoma and paraganglioma: From low-specific-activity to high-specific-activity iodine-131 metaiodobenzylguanidine. *Cancers (Basel)*. 2019;11(7). doi: 10.3390/cancers11071018
8. Theerakulpisut D, Raruenrom Y, Wongsurawat N, Somboonporn C. Value of SPECT/CT in Diagnostic I-131 MIBG Scintigraphy in Patients with Neuroblastoma. *Nucl Med Mol Imaging (2010)*. 2018;52(5):350–8. doi: 10.1007/s13139-018-0532-y
9. Gear J, Chiesa C, Lassmann M, Gabiña PM, Tran-gia J, Stokke C, et al. EANM Dosimetry Committee series on standard operational procedures for internal dosimetry for <sup>131</sup>I mIBG treatment of neuroendocrine tumours. *Eur J Nucl Med Mol imaging Phys*. 2020;7:15. doi: 10.1186/s40658-020-0282-7.
10. Dobbeleir AA, Hambÿe AE, Franken PR. Influence of high-energy photons on the

- spectrum of iodine-123 with low- and medium-energy collimators : consequences for imaging with <sup>123</sup>I-labelled compounds in clinical practice. *Eur J Nucl Med.* 1999;26(6):655–8. doi: 10.1007/s002590050434
11. Rault E, Vandenberghe S, Holen R Van, Beenhouwer J De, Staelens S, Lemahieu I. Comparison of image quality of different iodine isotopes ( <sup>123</sup>I , <sup>124</sup>I , and <sup>131</sup>I ). *Cancer Biother Radiopharm.* 2007;22(3). doi: 10.1089/cbr.2006.323
  12. Bailly C, Bodet-milin C, Bourgeois M, Gouard S, Ansquer C, Barbaud M, et al. Exploring Tumor Heterogeneity Using PET Imaging: The Big Picture. *Cancers (Basel).* 2019;11:17. doi: 10.3390/cancers11091282
  13. Lassmann M, Eberlein U. The Relevance of Dosimetry in Precision Medicine. *J Nucl Med.* 2018;59(10):1494–9. doi: 10.2967/jnumed.117.206649
  14. Tagesson M, Ljungberg M, Strand SE. A Monte Carlo program converting activity distributions to absorbed dose distributions in a radionuclide treatment planning system. *Acta Oncol (Madr).* 1996;35(3):367–72. doi: 10.3109/02841869609101653
  15. Loevinger R, Budinger TF. MIRD primer for absorbed dose calculations. *Soc Nuc Med;* 1991. 128 p.
  16. Lyra ME, Phinou P. Internal Dosimetry in Nuclear Medicine : A Summary of Its Development , Applications and Current Limitations. *RSO Mag.* 1999;5.
  17. MIRD. MIRD: Absorbed dose per unit cumulate activity for selected radionuclides and organs. 1975. p. 258.
  18. RADAR. The RAdiation Dose Assessment Resource. 2019. p. 0–3.
  19. Dewaraja YK, Wilderman SJ, Ljungberg M, Koral KF, Zasadny K, Kaminiski MS. Accurate dosimetry in <sup>131</sup>I radionuclide therapy using patient-specific, 3-dimensional methods for SPECT reconstruction and absorbed dose calculation. *J Nucl Med.* 2005;46(5):840–9. PMID: 15872359
  20. Ljungberg M, Sjögreen Gleisner K. Personalized Dosimetry for Radionuclide Therapy Using Molecular Imaging Tools. *Biomedicines.* 2016;4(4):25. doi: 10.3390/biomedicines4040025

21. Frey EC, Tsui BMW. A new method for modeling the spatially-variant, object-dependent scatter response function in SPECT. In: 1996 IEEE Nuclear Science Symposium Conference Record. IEEE; 1996. p. 1082–6. doi: 10.1109/nssmic.1996.591559
22. Roth D, Gustafsson J, Sundlöv A, Sjögreen Gleisner K. A method for tumor dosimetry based on hybrid planar-SPECT/CT images and semiautomatic segmentation. *Med Phys.* 2018;45(11):5004–18. doi: 10.1002/mp.13178
23. Morphis M, Staden JA Van, Raan H, Ljungberg M. Modelling of energy-dependent spectral resolution for SPECT Monte Carlo simulations using SIMIND. *Heliyon.* 2021;7:12. doi: 10.1016/j.heliyon.2021.e06097
24. Morphis M, Staden JA Van, du Raan H, Ljungberg M. Validation of a SIMIND Monte Carlo modelled gamma camera for Iodine-123 and Iodine-131 imaging. *Heliyon.* 2021;7:11. doi: 10.1016/j.heliyon.2021.e07196
25. Ljungberg M, Strand SE. A Monte Carlo program for the simulation of scintillation camera characteristics. *Comput Methods Programs Biomed.* 1989 Aug;29(4):257–72. doi: 10.1016/0169-2607(89)90111-9
26. Sjögreen K, Ljungberg M, Wingårdh K, Minarik D, Strand SE. The LundADose method for planar image activity quantification and absorbed-dose assessment in radionuclide therapy. *Cancer Biother Radiopharm.* 2005;20(1):92–7. doi: 10.1089/cbr.2005.20.92
27. Ljungberg M, Sjögreen K, Liu X, Frey E, Dewaraja Y, Strand S-E. A 3-Dimensional Absorbed Dose Calculation Method Based on Quantitative SPECT for Radionuclide Therapy: Evaluation for <sup>131</sup>I Using Monte Carlo Simulation. *J Nucl Med.* 2002;43:1101–9. PMID: 12163637
28. Morphis M, van Staden JA, du Raan H, Ljungberg M. Evaluation of Iodine-123 and Iodine-131 SPECT Activity Quantification: A Monte Carlo Study. 2021. *EJNMMI Phys.* doi: 10.1186/s40658-021-00407-1
29. Kangasmaa T, Sohlberg A, Kuikka JT. Reduction of Collimator Correction Artefacts with Bayesian Reconstruction in Spect. *Int J Mol Imaging.* 2011;2011:6. doi: 10.1155/2011/630813

30. Fielding S, Flower M, Ackery D, Kemshead J, Lashford L, Lewis I. Dosimetry of iodine 131 metaiodobenzylguanidine for treatment of resistant neuroblastoma : results of a UK study \*. *Eur J Nucl Med*. 1991;18:308–16. doi: 10.1007/bf02285457
31. Bolster A, Hilditch T, Wheldon T, Gaze, MN, Barrett A. Dosimetric considerations in 131 I-MIBG therapy for neuroblastoma in children. *Br J Radiol*. 1995;68(809):481–90. doi: 10.1259/0007-1285-68-815-1263-a
32. Bombardieri E, Giammarile F, Aktolun C, Baum RP, Bischof Delaloye A, Maffioli L, et al. 131I/123I-Metaiodobenzylguanidine (mIBG) scintigraphy: Procedure guidelines for tumour imaging. *Eur J Nucl Med Mol Imaging*. 2010;37(12):2436–46. doi: 10.1007/s00259-003-1357-0
33. Pandit-taskar N, Zanzonico P, Hilden P, Ostrovnaya I, Carrasquillo JA, Modak S. Assessment of Organ Dosimetry for Planning Repeat Treatments of high-dose I-131-MIBG therapy. *Clin Nucl Med*. 2017;00(00):1–8. doi: 10.1097/rlu.0000000000001752
34. Koral KF, Huberty JP, Frame B, Matthay KK, Maris JM, Regan D, et al. Hepatic absorbed radiation dosimetry during I-131 Metaiodobenzylguanidine ( MIBG ) therapy for refractory neuroblastoma. *Eur J Nucl Med Mol Imaging*. 2008;35:2105–12. doi: 10.1007/s00259-008-0873-3
35. Marks LB, Yorke ED, Jackson A, Ten Haken RK, Constine LS, Eisbruc, A, Bentzen SM, Nam J, Deasy JO. Use of normal tissue complication probability models in the clinic. *Int J Radiat Oncol Biol Phys*. 2010;76(3). doi: 10.1016/j.ijrobp.2009.07.1754
36. Grimes J, Celler A. Comparison of internal dose estimates obtained using organ-level , voxel S value , and Monte Carlo techniques. *Med Phys*. 2014;41(9):1–11. doi: 10.1118/1.4892606

# **Chapter 6: Summary and future work**

# Table of Contents

6.1 Summary.....	6.2
6.2 Future work.....	6.5

## 6.1 Summary

Delivering a lethal dose of radiation to tumour cells whilst maintaining safe levels to surrounding normal tissue is the goal of any radiation treatment. In South Africa, routine practice when performing radiopharmaceutical therapy in Nuclear Medicine (NM), is that fixed levels of therapeutic radionuclides are administered to all patients, with the idea that "one size fits all". Ultimately, this can lead to poor tumour control and, more concerningly, high levels of normal tissue complications. This emphasises the need for personalised radiopharmaceutical therapy planning and resulted in investigating the implementation of a dosimetry protocol for Universitas Academic Hospital (UAH) in Bloemfontein, South Africa. The study presented in this research aimed to assess the accuracy of patient-specific iodine-131 (I-131) dosimetry using hybrid whole-body (WB) planar-single-photon emission computed tomography/computed tomography (SPECT/CT) imaging. It will allow the clinician to predict the amount of activity to be administered to an individual, ensuring optimal tumour control whilst sparing surrounding normal tissues. The hybrid method of imaging is beneficial in institutions with large patient throughput, as it results in quantitative accuracies comparable to that from SPECT/CT imaging, with the speed of WB planar imaging. This study can improve I-131-metaiodobenzylguanidine (mIBG) radiopharmaceutical therapy at UAH and furthermore contribute to the application of NM Monte Carlo (MC) modelling in the field of medical physics.

To achieve the aim of this study, the work was subdivided into four chapters with distinct objectives. This chapter summarises the outcome of the four chapters and recommends some future work.

Chapter 2 (Paper I) focused on the validation of a proposed energy resolution model for the Simulation of imaging nuclear detectors (SIMIND) MC code, emulating the Siemens Symbia T16 gamma camera. This was achieved by fitting the proposed energy resolution model to measured energy resolution values as a function of photon energy. The accuracy of the fitted model was then validated by comparing measured and simulated energy spectra obtained from in-air and in-scatter measurements. Lastly, energy spectra simulated in a voxel-based digital patient-phantom were compared and evaluated. The results showed that modelling of the energy resolution across all energies is essential when simulating NM studies with high-



energy photon emitting radionuclides (e.g. I-131), as well as radionuclides with multiple photopeaks (e.g. lutetium-177, gallium-67 and I-131). Ultimately, the fitted energy resolution model proved accurate in modelling the energy resolution of the Siemens Symbia T16 gamma camera. Existing gamma camera models simulated with MC codes lack an accurate implementation of the gamma camera's energy response across all photon energies. This chapter addressed this deficiency by implementing a fitted function that models the Siemens Symbia T16 gamma camera's energy response across all energies and used it together with the SIMIND MC code to improve the gamma camera modelling. Therefore, the SIMIND MC code could be used with confidence to simulate NM images, for optimising imaging processing and activity quantification for dosimetry purposes.

It is important to first validate a MC code's capability of modelling a clinical gamma camera, prior to using it as a clinical simulator. This led to the work in chapter 3 (paper II) which aimed to validate the SIMIND modelling of the Siemens Symbia T16 gamma camera, specifically for iodine-123 (I-123) with both a low energy high resolution (LEHR) and medium energy (ME) collimator and I-131 with a high energy (HE) collimator imaging. The validation was achieved by comparing static planar, WB planar and SPECT gamma camera measurements with simulations. The results showed that when using I-123 and I-131 with the LEHR and HE collimator, respectively, appropriate collimator response corrections, including modelling of septal scatter and penetrations, were essential. The use of a ME collimator for I-123 imaging reduced the effects of septal penetration and collimator scatter from the high-energy photons, and therefore, the ME collimator was a better choice when no septal scatter and penetration corrections were available. Overall, this chapter showed the SIMIND MC code's potential usefulness, combined with the improved energy resolution model from chapter 2 (paper I), to further develop activity quantification methods for I-123 and I-131 static planar, WB planar and SPECT acquisitions with the Siemens Symbia T16 gamma camera.

The evaluation of SPECT activity quantification accuracy for I-123 (LEHR and ME collimator), and I-131 (HE collimator), using the validated SIMIND MC code (chapter 3 - paper II) with the fitted energy resolution model (chapter 2 - paper I) was presented in chapter 4 (paper III). This was accomplished by optimising the number of ordered subsets-estimation maximisation (OS-EM) updates for the SPECT iterative reconstruction algorithm

and determining an appropriate calibration factor (CF) and recovery coefficient (RC) curve for each radionuclide-collimator combination. Finally, the quantitative method was evaluated in voxel-based digital simple, and patient phantoms. The results showed that with the application of a simple CF source geometry and appropriate corrections for scatter, attenuation, collimator-detector response (CDR) and partial volume effects (PVEs), incorporated into the reconstruction of the SPECT data, quantification accuracies within 6.0% for all radionuclide-collimator combinations were obtained. The chapter showed that similar I-123 activity quantification accuracies were obtained with the LEHR and ME collimators, only if appropriate corrections for septal scatter and penetration were applied for the I-123 LEHR combination. If so, then the I-123 LEHR combination could be useful for departments without access to a ME collimator.

The accuracy of patient-specific absorbed dose calculations for tumours and organs at risk, based on hybrid WB planar-SPECT/CT imaging was presented in chapter 5 (paper IV). The study made use of quantitative data from both I-123 and I-131 MC simulated voxel-based digital patient phantoms to predict the absorbed dose for I-131-mIBG radiopharmaceutical therapy, using full MC radiation transport dosimetry techniques. MC dosimetry simulations were performed with both photon and beta interactions, as well as with beta interactions only. Two sets of images defining the quantified SPECT activity distribution for each radionuclide-collimator combination was used as input for the MC dose simulations. The two sets of input images were (i) the simulated quantified SPECT activity distribution from the patient phantom, post-reconstruction, and (ii) the simulated quantified SPECT activity distribution from the patient phantom, replacing the reconstructed activity distribution with a uniform distribution. Image set (i) activity distribution is the apparent image set to use; however, it is well known that when CDR correction is included in the iterative reconstruction, the Gibbs artefact may be present, and may affect the accuracy of the calculated absorbed dose. For this reason and based on the knowledge that the activity distribution for each region, used as input for the simulations was uniform, image set (ii) was created. Absorbed dose calculations were also performed for the true activity distribution, to which the dose values obtained from image sets (i) and (ii) were compared.

The results showed that image set (i) activity distribution resulted in an overestimation of absorbed dose values, due to the Gibbs artefact and the partial volume effect correction.

Replacing the reconstructed activity distribution with a uniform distribution (image set (ii)) overcame this problem and resulted in dosimetry accuracies within 5.9%. Furthermore, the absorbed dose values for beta interactions only resulted in an underestimation of up to 30.0% and 12.0% for the liver and tumour, respectively. This indicated that the assumption made by commercial software, such as OLINDA, which treats tumours as isolated objects (not including cross-dose to and from other tumours and organs at risk), may result in significant dose underestimation.

The MC hybrid method for dosimetry proved to be effective for personalised treatment planning of I-131 radiopharmaceutical therapy, with either I-123 or I-131 diagnostic imaging. Highly accurate dosimetry results were obtained for the liver and tumours as small as 14.0 ml (3.0 cm diameter), when considering photon and beta interactions. Despite the poorer I-123 LEHR and I-131 HE image quality, relatively good quantification accuracy was obtained. I-131 absorbed dose values obtained from I-123 and I-131 images were comparable. The novel use of a uniform activity distribution incorporated in image set (ii) resulted in more accurate average liver and tumour absorbed doses for the three patients when compared to the non-uniform reconstructed activity distribution present in image set (i).

## **6.2 Future work**

The work in chapter 2 (paper I) could be expanded by fitting the proposed energy resolution model to energy resolution values acquired on gamma cameras from different vendors, such as the GE Discovery NM/CT 670 system in use at National District Hospital, Bloemfontein, South Africa. This would allow for us to use the SIMIND MC code to simulate NM images that mimic other gamma camera systems in our department. It would also be interesting to investigate the number of measured energy resolution points required to accurately model the gamma camera's energy resolution. This could be beneficial to departments that do not have access to the large range of different radionuclides as used in chapter 2 (paper I). Expanding on the work presented in chapter 2 (paper I), it may be interesting to incorporate the gamma camera's non-linear energy response into SIMIND and assess if there is any improvement on the proposed energy resolution model. This may be of interest for yttrium-90 imaging, where the modelling of low energy photons is important.

There is much debate on how to accurately correct for PVEs. Chapter 4 (paper III) made use of the characteristic RC curve correction method, where recovery coefficients were calculated based on spheres of different sizes, with a uniform activity distribution. It will be of value to investigate the effect of object shape and activity distribution on the accuracy of I-123 and I-131 activity quantification.

Chapter 5 (paper IV) recommended the use of image set (ii) activity distribution when performing I-131 absorbed dose calculations. This method was proposed with the knowledge that the initial activity distribution was uniform. As organ and tumour activity distributions are not uniform, the study could be expanded by investigating the effect a non-uniform initial activity distribution would have on the resultant absorbed dose. The question arises whether the calculated absorbed dose when applying a uniform activity distribution in such cases, would be accurate. It may be worthwhile investigating the influence of patient, as well as tumour and organ motion on the accuracy of absorbed dose calculations. In addition, it may also be of value to compare the accuracy of absorbed dose calculations when using the hybrid method and the currently used planar MIRD method at UAH. Ultimately, the next step would be to implement and test the hybrid method in a clinical situation, with patient studies.

# Appendices

# Table of Contents

Appendix A: <i>Paper I – front page of published article</i> .....	A - 2
Appendix B: <i>Paper II – front page of published article</i> .....	A - 3
Appendix C: <i>Paper III – front page of published article</i> .....	A - 4
Appendix D: <i>Additional information and results</i> .....	A - 5
Appendix E: <i>Ethics approval letter</i> .....	A - 9
Appendix F: <i>Turnitin report</i> .....	A - 10



## Research article

## Modelling of energy-dependent spectral resolution for SPECT Monte Carlo simulations using SIMIND



Michaella Morphis<sup>a,\*</sup>, Johan A. van Staden<sup>a</sup>, Hanlie du Raan<sup>a</sup>, Michael Ljungberg<sup>b</sup>

<sup>a</sup> Department of Medical Physics, Faculty of Health Sciences, University of the Free State, Bloemfontein, South Africa

<sup>b</sup> Department of Medical Radiation Physics, Lund University, Lund, Sweden

## ARTICLE INFO

## Keywords:

Monte Carlo simulation;  
Energy resolution;  
Multiple photopeak isotopes;  
Energy spectrum

## ABSTRACT

**Purpose:** Monte Carlo (MC) modelling techniques have been used extensively in Nuclear Medicine (NM). The theoretical energy resolution relationship ( $\propto 1/\sqrt{E}$ ), does not accurately predict the gamma camera detector response across all energies. This study aimed to validate the accuracy of an energy resolution model for the SIMIND MC simulation code emulating the Siemens Symbia T16 dual-head gamma camera.

**Methods:** Measured intrinsic energy resolution data (full width half maximum (FWHM) values), for Ba-133, Lu-177, Am-241, Ga-67, Tc-99m, I-123, I-131 and F-18 sources in air, were used to create a fitted model of the energy response of the gamma camera. Both the fitted and theoretical models were used to simulate intrinsic and extrinsic energy spectra using three different scenarios (source in air; source in simple scatter phantom and a clinical voxel-based digital patient phantom).

**Results:** The results showed the theoretical model underestimated the FWHM values at energies above 160.0 keV up to 23.5 keV. In contrast, the fitted model better predicted the measured FWHM values with differences less than 3.3 keV. The I-131 in-scatter energy spectrum simulated with the fitted model better matched the measured energy spectrum. Higher energy photopeaks, (I-123: 528.9 keV and I-131: 636.9 keV) simulated with the fitted model, more accurately resembled the measured photopeaks. The voxel-based digital patient phantom energy spectra, simulated with the fitted and theoretical models, showed the potential impact of an incorrect energy resolution model when simulating isotopes with multiple photopeaks.

**Conclusion:** Modelling of energy resolution with the proposed fitted model enables the SIMIND user to accurately simulate NM images. A great improvement was seen for high-energy photon emitting isotopes (e.g. I-131), as well as isotopes with multiple photopeaks (e.g. Lu-177, I-131 and Ga-67) in comparison to the theoretical model. This will result in accurate evaluation of radioactivity quantification, which is vital for dosimetric purposes.

## 1. Introduction

Monte Carlo (MC) modelling techniques have been used extensively in the field of nuclear medicine (NM) over the past 50 years. These techniques are ideal in NM because of the stochastic nature of radiation emission, transport, and the detection process. Essential applications of MC modelling techniques in NM include collimator and detector design, image reconstruction and scatter correction techniques, as well as internal dosimetry. MC techniques are also useful in studying phenomena that may be impractical, or impossible to measure, such as collimator septal penetration and scatter. Various MC simulation codes with application to NM imaging, such as SIMIND [1], SimSET [2] and GATE [3], are available, illustrating the significance of MC simulations in NM.

The importance of patient-specific targeted radiopharmaceutical therapy for cancer therapy has increased over the past decade [4, 5, 6, 7, 8]. Thus, accurate image quantification has become increasingly important in NM. MC techniques have been used extensively to evaluate quantification procedures in NM imaging [1, 9, 10, 11]. When making use of MC simulation software, it is essential to ensure that the intrinsic characteristics of the imaging system are defined correctly. One such characteristic is the energy resolution, which is described as the system's ability to distinguish between two radiation energies with a small energy difference [12]. Factors such as variations in the number of light scintillation photons generated in the crystal, the number of photoelectrons produced in the photocathode, as well as the multiplication factor of the photomultiplier tubes, all contribute to variations in the signal amplitude

\* Corresponding author.

E-mail address: [michaellamorphis@icloud.com](mailto:michaellamorphis@icloud.com) (M. Morphis).

<https://doi.org/10.1016/j.heliyon.2021.e06097>

Received 20 November 2020; Received in revised form 22 December 2020; Accepted 21 January 2021

2405-8440/© 2021 Published by Elsevier Ltd. This is an open access article under the CC BY-NC-ND license (<http://creativecommons.org/licenses/by-nc-nd/4.0/>).



## Research article

## Validation of a SIMIND Monte Carlo modelled gamma camera for Iodine-123 and Iodine-131 imaging



Michaela Morphis<sup>a,\*</sup>, Johan A. van Staden<sup>a</sup>, Hanlie du Raan<sup>a</sup>, Michael Ljungberg<sup>b</sup>

<sup>a</sup> Department of Medical Physics, Faculty of Health Sciences, University of the Free State, Bloemfontein, South Africa

<sup>b</sup> Medical Radiation Physics, Lund University, Lund, Sweden

## ARTICLE INFO

**Keywords:**  
Validation  
Monte Carlo simulations  
SIMIND  
I-123  
I-131  
Static planar  
WB planar  
SPECT

## ABSTRACT

**Purpose:** Monte Carlo (MC) modelling techniques can assess the quantitative accuracy of both planar and SPECT Nuclear Medicine images. It is essential to validate the MC code's capabilities in modelling a specific clinical gamma camera, for radionuclides of interest, before its use as a clinical image simulator. This study aimed to determine if the SIMIND MC code accurately simulates emission images measured with a Siemens Symbia™ T16 SPECT/CT system for I-123 with a LEHR and a ME collimator and for I-131 with a HE collimator.

**Methods:** The static and WB planar validation tests included extrinsic system energy pulse height distributions (EPHDs), system sensitivity and system spatial resolution in air as well as a scatter medium. The SPECT validation test comprised the sensitivity from a simple geometry of a sphere in a cylindrical water-filled phantom.

**Results:** The system EPHDs compared well, with differences between measured and simulated primary photopeak FWHM values not exceeding 4.6 keV. Measured and simulated planar system sensitivity values displayed percentage differences less than 6.9% and 6.3% for static and WB planar images, respectively. Measured and simulated planar system spatial resolution values in air showed percentage differences not exceeding 6.4% (FWHM) and 10.0% (FWHM), and 5.1% (FWHM) and 5.4% (FWHM) for static and WB planar images, respectively. For static planar system spatial resolution measured and simulated in a scatter medium, percentage differences of FWHM and FWTM values were less than 5.8% and 12.6%, respectively. The maximum percentage difference between the measured and simulated SPECT validation results was 3.6%.

**Conclusion:** The measured and simulated validation results compared well for all isotope-collimator combinations and showed that the SIMIND MC code could be used to accurately simulate static and WB planar and SPECT projection images of the Siemens Symbia™ T16 SPECT/CT for both I-123 and I-131 with their respective collimators.

## 1. Introduction

Due to the increased interest in theranostics in Nuclear Medicine (NM), the importance of image quantification using iodine-131 (I-131) and iodine-123 (I-123) has been re-emphasised (Silberstein 2012; Sjögreen et al., 2002; Yordanova et al., 2017). I-131 is one of the earliest radionuclides used for radionuclide therapy. Since the 1940s, I-131 has been used to treat differentiated thyroid carcinoma, and is the radionuclide of choice for thyroid diseases (Thomas 2002). However, it has gained popularity in the treatment of non-Hodgkin lymphomas and neuroendocrine tumours (NETs). I-131 emits a principal gamma photon of 364.5 keV (81.2% abundance), one with 284.3 keV (6.1% abundance) and two higher energy photons of 636.9 keV (7.1% abundance) and 722.9 keV (1.8%

abundance). Despite the low abundance of these two high-energy photons, they are still of importance due to their ability to penetrate the gamma camera's collimator septa. I-131 has a physical half-life of 8.04 days and also emits beta particles with a maximum and mean energy of 606.0 keV and 192.0 keV, respectively (Kelleff et al., 2017). Iodine naturally accumulates in the thyroid; however, it can be attached to a pharmaceutical, allowing targeted imaging and therapy. I-131 labelled to a noradrenaline analogue, meta-iodobenzylguanidine (MIBG), is typically used to detect and treat NETs. It naturally accumulates in NETs as well as the lungs, liver, kidneys, spleen, bladder, bone marrow and salivary glands (Bombardieri et al., 2010; Giannarile et al., 2006).

In contrast to I-131, which emits both gamma photons and beta particles, I-123 is a pure gamma photon emitter. It emits a principal

\* Corresponding author.

E-mail address: michaelamorphis@icloud.com (M. Morphis).

<http://doi.org/10.1016/j.heliyon.2021.e07196>

Received 30 March 2021; Received in revised form 11 May 2021; Accepted 28 May 2021

2405-8440/© 2021 The Authors. Published by Elsevier Ltd. This is an open access article under the CC BY-NC-ND license (<http://creativecommons.org/licenses/by-nc-nd/4.0/>).



ORIGINAL RESEARCH

Open Access



# Evaluation of Iodine-123 and Iodine-131 SPECT activity quantification: a Monte Carlo study

Michaela Morphis<sup>1\*</sup>, Johan A. van Staden<sup>1</sup>, Hanlie du Raan<sup>1</sup> and Michael Ljungberg<sup>2</sup>

\*Correspondence: [michmor@uj.ac.za](mailto:michmor@uj.ac.za)  
<sup>1</sup>Department of Medical Physics, Faculty of Health Sciences, University of the Free State, PO Box 339, Bloemfontein 9300, South Africa  
 Full list of author information is available at the end of the article

**Abstract**

**Purpose:** The quantitative accuracy of Nuclear Medicine images, acquired for both planar and SPECT studies, is influenced by the isotope-collimator combination as well as image corrections incorporated in the iterative reconstruction process. These factors can be investigated and optimised using Monte Carlo simulations. This study aimed to evaluate SPECT quantification accuracy for <sup>123</sup>I with both the low-energy high resolution (LEHR) and medium-energy (ME) collimators and <sup>131</sup>I with the high-energy (HE) collimator.

**Methods:** Simulated SPECT projection images were reconstructed using the OS-EM iterative algorithm, which was optimised for the number of updates, with appropriate corrections for scatter, attenuation and collimator detector response (CDR), including septal scatter and penetration compensation. An appropriate calibration factor (CF) was determined from four different source geometries (activity-filled, water-filled cylindrical phantom, sphere in water-filled (cold) cylindrical phantom, sphere in air and point-like source), investigated with different volume of interest (VOI) diameters. Recovery curves were constructed from recovery coefficients to correct for partial volume effects (PVEs). The quantitative method was evaluated for spheres in voxel-based digital cylindrical and patient phantoms.

**Results:** The optimal number of OS-EM updates was 60 for all isotope-collimator combinations. The CF<sub>mean</sub> with a VOI diameter equal to the physical size plus a 3.0-cm margin was selected, for all isotope-collimator geometries. The spheres' quantification errors in the voxel-based digital cylindrical and patient phantoms were less than 3.2% and 5.4%, respectively, for all isotope-collimator combinations.

**Conclusion:** The study showed that quantification errors of less than 6.0% could be attained, for all isotope-collimator combinations, if corrections for scatter, attenuation, CDR (including septal scatter and penetration) and PVEs are performed. <sup>123</sup>I LEHR and <sup>131</sup>I ME quantification accuracies compared well when appropriate corrections for septal scatter and penetration were applied. This can be useful in departments that perform <sup>123</sup>I studies and may not have access to ME collimators.

**Keywords:** Monte Carlo simulations, SIMIND, Quantification accuracy, <sup>123</sup>I, <sup>131</sup>I, SPECT



© The Author(s). 2021 **Open Access** This article is licensed under a Creative Commons Attribution 4.0 International License, which permits use, sharing, adaptation, distribution and reproduction in any medium or format, as long as you give appropriate credit to the original author(s) and the source, provide a link to the Creative Commons licence, and indicate if changes were made. The images or other third party material in this article are included in the article's Creative Commons licence, unless indicated otherwise in a credit line to the material. If material is not included in the article's Creative Commons licence and your intended use is not permitted by statutory regulation or exceeds the permitted use, you will need to obtain permission directly from the copyright holder. To view a copy of this licence, visit <http://creativecommons.org/licenses/by/4.0/>.

## Appendix D: Additional information and results

Table D1 summarises the general SIMIND settings for the SIMIND change program.

**Table D1:** General SIMIND settings and simulation parameters

<i>Simulation flags</i>	
Write results to the screen	True
Write image matrix to file	True
Write pulse-height distribution to file	True
Include the collimator	True
Simulate a SPECT study	True
Include characteristic X-Ray emission	True
Include backscattering material	True
Use a random sampled seed Value	True
Simulate a transmission study	False
Include interactions in the cover	True
Include interactions in the phantom	True
Include simulation of energy resolution	True
Include forced Interaction at crystal entry	True
Write file header in INTERFILE V3.3 format	True
Save aligned density map	True
<i>Physical camera parameters</i>	
Crystal half-length	22.25 cm (SPECT)
	100.0 cm (WB planar)
Crystal thickness	0.95 cm
Crystal half-width	29.55 cm
Crystal material	NaI
Backscattering material thickness	7.5 cm
Backscatter material	Photomultiplier tube
<i>Scintillation camera parameters</i>	
Intrinsic spatial resolution at 140 keV	0.38 cm
Pixel size in simulated image	0.48 cm (SPECT)
	0.24 cm (WB planar)
Number of projections	60 (SPECT)
	2 (WB planar)
<i>Phantom parameters</i>	
Pixel size in density map	0.1269 cm
Distance between surface of phantom and detector	2.0 cm
<i>Image Parameters</i>	
Simulation matrix size	128 × 128 (SPECT)
	256 × 1024 (WB planar)

Density map matrix size	512 × 512		
Energy spectra channels	512		
keV per channel	1		
<i>*Collimator parameters (cm)</i>	<i>LEHR</i>	<i>ME</i>	<i>HE</i>
Hole size: X direction	0.1110	0.2940	0.4000
Hole size: Y direction	0.1282	0.3395	0.4619
Distance between holes: X direction	0.0160	0.1140	0.2000
Distance between holes: Y direction	0.0918	0.3672	0.5774
Collimator thickness	2.4050	4.0640	5.9700

\* LEHR – low energy high resolution, ME – medium energy, HE – high energy

Table D2 and Table D3 show the voxel-based digital patient-phantom activity concentration values for each volume of interest, at the different simulation timepoints for I-123 assuming an injected activity of 380.4 MBq, and I-131 assuming an injected activity of 190.2 MBq, respectively.

**Table D2:** I-123 activity concentration values for each volume of interest

Timepoint	Activity concentration (kBq/ml)			
	Liver	Lungs	Tumours	Remainder
1	27.2	15.2	333.9	3.3
4	21.9	11.8	271.1	2.7
6	18.9	10.0	235.9	2.4
24	5.0	2.2	67.5	0.7
36	2.1	0.8	29.3	0.3

**Table D3:** I-131 activity concentration values for each volume of interest

Timepoint	Activity concentration (kBq/ml)			
	Liver	Lungs	Tumours	Remainder
6	12.6	6.7	158.1	1.6
24	8.1	3.6	108.9	1.1
36	6.0	2.4	85.0	0.8
48	4.5	1.6	66.3	0.7
72	2.5	0.7	40.4	0.4

Table D4 shows example time-dose-rate curves for the liver and two tumours of patient 1 scenario a, assuming true activity distribution, for all three radionuclide-collimator combinations.

**Table D4:** Time-dose-rate curves obtained from true activity distribution of patient 1 scenario a, for the liver and both tumours.

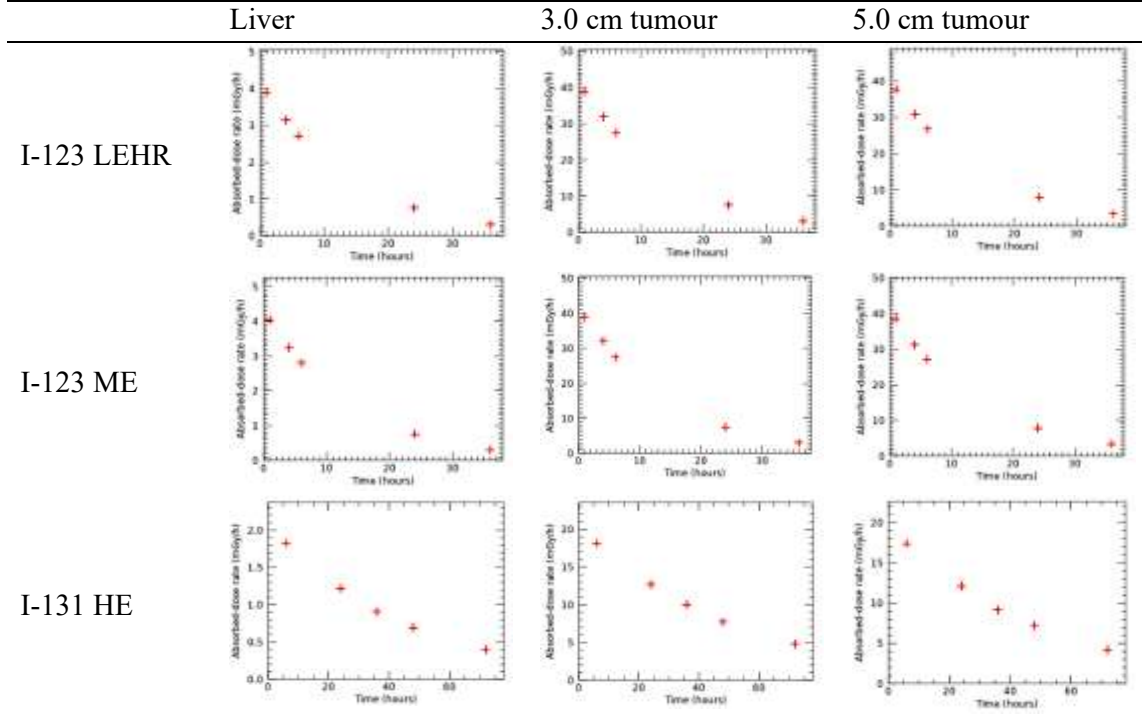




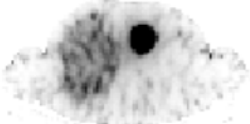















Table D5 shows example transverse slices through activity maps and corresponding dose-rate maps, for the true activity distribution, quantified activity distribution, and quantified activity uniformly distributed, of patient 1 scenario a, for the three radionuclide-collimator combinations.

**Table D5:** Transverse slices through activity maps and corresponding dose-rate maps, for the true activity distribution, quantified activity distribution, and quantified activity uniformly distributed.

		True activity distribution	Quantified activity distribution	Quantified activity uniformly distributed
I-123 LEHR	Activity map			
	Dose-rate map			
-----				
I-123 ME	Activity map			
	Dose-rate map			
-----				
I-131 HE	Activity map			
	Dose-rate map			

## Appendix E: Ethics approval letter



### Health Sciences Research Ethics Committee

28-Jan-2020

Dear Miss Michaela Morphis

Ethics Clearance: Accuracy of patient-specific dosimetry using hybrid planar-SPECT/CT imaging: A Monte Carlo study

Principal Investigator: Miss Michaela Morphis

Department: Medical Physics Department (Bloemfontein Campus)

**APPLICATION APPROVED**

Please ensure that you read the whole document

With reference to your application for ethical clearance with the Faculty of Health Sciences, I am pleased to inform you on behalf of the Health Sciences Research Ethics Committee that you have been granted ethical clearance for your project.

Your ethical clearance number, to be used in all correspondence is: **UFS-HSD2019/2135/2502**

The ethical clearance number is valid for research conducted for one year from issuance. Should you require more time to complete this research, please apply for an extension.

We request that any changes that may take place during the course of your research project be submitted to the HSREC for approval to ensure we are kept up to date with your progress and any ethical implications that may arise. This includes any serious adverse events and/or termination of the study.

A progress report should be submitted within one year of approval, and annually for long term studies. A final report should be submitted at the completion of the study.

The HSREC functions in compliance with, but not limited to, the following documents and guidelines: The SA National Health Act No. 61 of 2003; Ethics in Health Research: Principles, Structures and Processes (2015); SA GCP(2006); Declaration of Helsinki; The Belmont Report; The US Office of Human Research Protections 45 CFR 461 (for non-exempt research with human participants conducted or supported by the US Department of Health and Human Services- (HHS), 21 CFR 50, 21 CFR 56; CIOMS; ICH-GCP-E6 Sections 1-4; The International Conference on Harmonization and Technical Requirements for Registration of Pharmaceuticals for Human Use (ICH Tripartite), Guidelines of the SA Medicines Control Council as well as Laws and Regulations with regard to the Control of Medicines, Constitution of the HSREC of the Faculty of Health Sciences.

For any questions or concerns, please feel free to contact HSREC Administration: 051-4017794/5 or email [EthicsFHS@ufs.ac.za](mailto:EthicsFHS@ufs.ac.za).

Thank you for submitting this proposal for ethical clearance and we wish you every success with your research.

Yours Sincerely

Dr. SM Le Grange

Chair : Health Sciences Research Ethics Committee

Health Sciences Research Ethics Committee

Office of the Dean: Health Sciences

T: +27 (0)51 401 7795/7794 | E: [ethicsfhs@ufs.ac.za](mailto:ethicsfhs@ufs.ac.za)

IRB 00011992; REC 230406-011; IORG 0010096; FWA 00027947

Block D, Dean's Division, Room D104 | P.O. Box/Posbus 339 (Internal Post Box G40) | Bloemfontein 9300 | South Africa



## Appendix F: Turnitin report

---

ORIGINALITY REPORT

---

<b>8</b> %	<b>8</b> %	<b>1</b> %	<b>1</b> %
SIMILARITY INDEX	INTERNET SOURCES	PUBLICATIONS	STUDENT PAPERS

---

PRIMARY SOURCES

---

<b>1</b>	<a href="http://link.springer.com">link.springer.com</a> Internet Source	<b>1</b> %
<b>2</b>	<a href="http://www.mdpi.com">www.mdpi.com</a> Internet Source	<b>1</b> %
<b>3</b>	<a href="http://open.library.ubc.ca">open.library.ubc.ca</a> Internet Source	<b>1</b> %
<b>4</b>	<a href="http://ejnmiphys.springeropen.com">ejnmiphys.springeropen.com</a> Internet Source	<b>&lt;1</b> %
<b>5</b>	<a href="http://lup.lub.lu.se">lup.lub.lu.se</a> Internet Source	<b>&lt;1</b> %
<b>6</b>	<a href="http://www.frontiersin.org">www.frontiersin.org</a> Internet Source	<b>&lt;1</b> %
<b>7</b>	<a href="http://kanazawa-u.repo.nii.ac.jp">kanazawa-u.repo.nii.ac.jp</a> Internet Source	<b>&lt;1</b> %
<b>8</b>	<a href="http://www.science.gov">www.science.gov</a> Internet Source	<b>&lt;1</b> %
<b>9</b>	<a href="http://epubs.surrey.ac.uk">epubs.surrey.ac.uk</a> Internet Source	<b>&lt;1</b> %

---

10	<a href="http://jnm.snmjournals.org">jnm.snmjournals.org</a> Internet Source	<1 %
11	<a href="http://www.eanm.org">www.eanm.org</a> Internet Source	<1 %
12	<a href="http://iopscience.iop.org">iopscience.iop.org</a> Internet Source	<1 %
13	<a href="http://silo.tips">silo.tips</a> Internet Source	<1 %
14	<a href="http://trepo.tuni.fi">trepo.tuni.fi</a> Internet Source	<1 %
15	<a href="http://thesesups.ups-tlse.fr">thesesups.ups-tlse.fr</a> Internet Source	<1 %
16	<a href="http://journals.plos.org">journals.plos.org</a> Internet Source	<1 %
17	<a href="http://ejnmmires.springeropen.com">ejnmmires.springeropen.com</a> Internet Source	<1 %
18	<a href="http://abmpk.files.wordpress.com">abmpk.files.wordpress.com</a> Internet Source	<1 %
19	<a href="http://biblio.ugent.be">biblio.ugent.be</a> Internet Source	<1 %
20	Submitted to University of Notre Dame Student Paper	<1 %
21	<a href="http://orca-mwe.cf.ac.uk">orca-mwe.cf.ac.uk</a> Internet Source	<1 %



22	<a href="http://ndl.ethernet.edu.et">ndl.ethernet.edu.et</a> Internet Source	<1 %
23	<a href="http://radiologykey.com">radiologykey.com</a> Internet Source	<1 %
24	<a href="http://www.ncbi.nlm.nih.gov">www.ncbi.nlm.nih.gov</a> Internet Source	<1 %
25	<a href="http://livrepository.liverpool.ac.uk">livrepository.liverpool.ac.uk</a> Internet Source	<1 %
26	<a href="http://Munin.uit.no">Munin.uit.no</a> Internet Source	<1 %
27	<a href="http://aapm.onlinelibrary.wiley.com">aapm.onlinelibrary.wiley.com</a> Internet Source	<1 %
28	<a href="http://digitalcommons.library.tmc.edu">digitalcommons.library.tmc.edu</a> Internet Source	<1 %
29	<a href="http://www.yumpu.com">www.yumpu.com</a> Internet Source	<1 %
30	<a href="http://cms.galenos.com.tr">cms.galenos.com.tr</a> Internet Source	<1 %
31	<a href="http://slidelegend.com">slidelegend.com</a> Internet Source	<1 %
32	Submitted to North West University Student Paper	<1 %
33	<a href="http://oatext.com">oatext.com</a> Internet Source	<1 %

34	<a href="http://ro.uow.edu.au">ro.uow.edu.au</a> Internet Source	<1 %
35	<a href="http://www.his.se">www.his.se</a> Internet Source	<1 %
36	<a href="http://www.rug.nl">www.rug.nl</a> Internet Source	<1 %
37	Bingxin Gu, Mingyuan Meng, Lei Bi, Jinman Kim, David Dagan Feng, Shaoli Song. "Prediction of 5-year Progression-Free Survival in Advanced Nasopharyngeal Carcinoma with Pretreatment PET/CT using Multi-Modality Deep Learning-based Radiomics", Research Square Platform LLC, 2021 Publication	<1 %
38	<a href="http://epdf.pub">epdf.pub</a> Internet Source	<1 %
39	<a href="http://issuu.com">issuu.com</a> Internet Source	<1 %
40	Submitted to The University of Manchester Student Paper	<1 %
41	<a href="http://acsjournals.onlinelibrary.wiley.com">acsjournals.onlinelibrary.wiley.com</a> Internet Source	<1 %
42	<a href="http://citeseerx.ist.psu.edu">citeseerx.ist.psu.edu</a> Internet Source	<1 %

43	<a href="https://tel.archives-ouvertes.fr">tel.archives-ouvertes.fr</a> Internet Source	<1 %
44	<a href="https://hal.archives-ouvertes.fr">hal.archives-ouvertes.fr</a> Internet Source	<1 %
45	<a href="https://mafiadoc.com">mafiadoc.com</a> Internet Source	<1 %
46	<a href="https://portal.research.lu.se">portal.research.lu.se</a> Internet Source	<1 %
47	Submitted to Imperial College of Science, Technology and Medicine Student Paper	<1 %
48	Lore Santoro, Laurine Pitalot, Dorian Trauchessec, Erick Mora-Ramirez et al. "Clinical Implementation of PLANET®Dose for Dosimetric Assessment after 177Lu- DOTATATE: Comparison with Dosimetry Toolkit® and OLINDA/EXM® V1.0", Research Square, 2020 Publication	<1 %
49	Submitted to University of Surrey Student Paper	<1 %
50	<a href="https://aip.scitation.org">aip.scitation.org</a> Internet Source	<1 %
51	<a href="https://discovery.ucl.ac.uk">discovery.ucl.ac.uk</a> Internet Source	<1 %

52	<a href="http://edoc.ub.uni-muenchen.de">edoc.ub.uni-muenchen.de</a> Internet Source	<1 %
53	<a href="http://oak.go.kr">oak.go.kr</a> Internet Source	<1 %
54	<a href="http://www.habeat.eu">www.habeat.eu</a> Internet Source	<1 %
55	<a href="http://www.zora.uzh.ch">www.zora.uzh.ch</a> Internet Source	<1 %
56	<a href="http://brage.bibsys.no">brage.bibsys.no</a> Internet Source	<1 %
57	<a href="http://wachusett.umassmed.edu">wachusett.umassmed.edu</a> Internet Source	<1 %
58	<a href="http://docplayer.net">docplayer.net</a> Internet Source	<1 %
59	<a href="http://ejnmmipharmchem.springeropen.com">ejnmmipharmchem.springeropen.com</a> Internet Source	<1 %
60	<a href="http://www.omicsonline.org">www.omicsonline.org</a> Internet Source	<1 %
61	Submitted to Associatie K.U.Leuven Student Paper	<1 %
62	Clarita Saldarriaga Vargas, Lara Struelens, Matthias D'Huyvetter, Vicky Caveliers, Peter Covens. "Assessment of Mouse-Specific Pharmacokinetics in Kidneys Based on 131I	<1 %

---

Activity Measurements Using Micro-SPECT",  
Research Square Platform LLC, 2021

Publication

---

63	Julian MM Rogasch, Stephanie Bluemel, Oliver S. Grosser, Josefine Albers et al. "Feasibility of iodine-123-mIBG SPECT/CT quantification in neuroblastoma using CZT and NaI detectors", Research Square, 2020 Publication	<1 %
64	Submitted to Mahidol University Student Paper	<1 %
65	Submitted to Royal Melbourne Institute of Technology Student Paper	<1 %
66	Submitted to University of Edinburgh Student Paper	<1 %
67	Submitted to University of South Australia Student Paper	<1 %
68	core.ac.uk Internet Source	<1 %
69	www.dosisoft.com Internet Source	<1 %
70	www.scribd.com Internet Source	<1 %
71	archive-ouverte.unige.ch Internet Source	<1 %

---

72	de.scribd.com Internet Source	<1 %
73	eprints.mums.ac.ir Internet Source	<1 %
74	publicacoes.cardiol.br Internet Source	<1 %
75	repub.eur.nl Internet Source	<1 %
76	www.medimaging.gr Internet Source	<1 %
77	University of Tennessee, Knoxville Publication	<1 %
78	idoc.pub Internet Source	<1 %

Exclude quotes    On  
Exclude bibliography    On

Exclude matches    < 10 words